

DTIC FILE COPY

(2)

NPS 61-89-009

NAVAL POSTGRADUATE SCHOOL

Monterey, California

AD-A218 019

DTIC
ELECTE
FEB 14 1990
S D



THESIS

CORRELATION OF ATMOSPHERIC OPTICAL TUR-
BULENCE AND METEOROLOGICAL MEASURE-
MENTS

by

Gail M. Tirrell Vaucher

June 1989

Thesis Advisor

Donald L. Walters

Approved for public release; distribution is unlimited.

Prepared for:

Air Force Weapons Laboratory
(AFWL/ARCS, Mr. Paul Kervin)
Kirtland AFB, NM 87117-6008

90 02 13 016

NAVAL POSTGRADUATE SCHOOL
Monterey, California 93943

Rear Admiral R. C. Austin
Superintendent


H. Shull
Provost


This thesis prepared in conjunction with research sponsored in part by the Strategic Defense Initiative Organization through the US Air Force Weapons Laboratory under NPS 61-89-009.

Reproduction of all or part of this report is authorized.

Approved by:

Released by:


KARLHEINZ E. WOELER
Chairman of Physics


GORDON E. SCHACHER
Dean of Science and Engineering

Unclassified

security classification of this page

REPORT DOCUMENTATION PAGE

1a Report Security Classification Unclassified		1b Restrictive Markings	
2a Security Classification Authority		3 Distribution Availability of Report Approved for public release; distribution is unlimited.	
2b Declassification Downgrading Schedule		5 Monitoring Organization Report Number(s)	
4 Performing Organization Report Number(s) NPS-61-89-009		7a Name of Monitoring Organization Strategic Defense Initiative Organization (SDIO/DE)	
6a Name of Performing Organization Naval Postgraduate School	6b Office Symbol (if applicable) 63	7b Address (city, state, and ZIP code) 1717 H Street Washington, D.C. 20301	
6c Address (city, state, and ZIP code) Monterey, CA 93943-5000		9 Procurement Instrument Identification Number AFWL 88-MP-130	
8a Name of Funding Sponsoring Organization Air Force Weapons Laboratory (Mr. Paul Kervin)	8b Office Symbol (if applicable) AFWL-ARCS	10 Source of Funding Numbers	
8c Address (city, state, and ZIP code) Kirtland Air Force Base, NM 87117-6008		Program Element No Project No Task No Work Unit Accession No	
11 Title (include security classification) CORRELATION OF ATMOSPHERIC OPTICAL TURBULENCE AND METEOROLOGICAL MEASUREMENTS (Unclassified)			
12 Personal Author(s) Guil M. Tirrell Vaucher in conjunction with Donald L. Walters			
13a Type of Report Master's Thesis	13b Time Covered From To	14 Date of Report (year, month, day) June 1989	15 Page Count 157
16 Supplementary Notation The views expressed in this thesis are those of the author and do not reflect the official policy or position of the Department of Defense or the U.S. Government.			
17 Cosati Codes		18 Subject Terms (continue on reverse if necessary and identify by block number)	
Field	Group	atmospheric optical turbulence, transverse coherence length, isoplanometer, C_T^2 , Relay Mirror Experiment (RME)	
19 Abstract (continue on reverse if necessary and identify by block number) $(r_{sub} 0)$ $(\theta_{sub} 0)$ The correlation of meteorological events such as the jet stream, gravity waves and boundary layer circulation with the optical turbulence parameters, the transverse coherence length (r_0) and the isoplanatic angle (θ_0) is essential for interpreting and forecasting imaging and laser systems performance. In support of the United State Air Force Relay Mirror Experiment, the Naval Postgraduate School performed a series of six site characterization measurements near Kihei, Maui, during August 1987 to July 1988. Spatial and temporal summaries of atmospheric events corresponding to the optical remote sensor data are presented using meteorological data from the National Weather Service Radiosonde Observation stations, synoptic charts, GOES-WEST infrared satellite images, and four Kihei, Maui rawinsonde datasets. To quantify the correlation between optical turbulence measurements and meteorological phenomena, four methods of calculating (C) from rawinsonde data were investigated. Results show that existing rawinsonde systems are inadequate for direct (C) calculation. However, moderate improvements in the vertical resolution, the temperature resolution and probe response time, will allow direct calculations of optical turbulence parameters from rawinsonde data. $\theta_{sub} 0$ (RH) $C_{square} (T)$			
20 Distribution Availability of Abstract <input checked="" type="checkbox"/> unclassified unlimited <input type="checkbox"/> same as report <input type="checkbox"/> DTIC users		21 Abstract Security Classification Unclassified	
22a Name of Responsible Individual Donald L. Walters		22b Telephone (include Area code) (408) 646-2267	22c Office Symbol 61We

DD FORM 1473.84 MAR

83 APR edition may be used until exhausted
All other editions are obsolete

security classification of this page

Unclassified

Approved for public release; distribution is unlimited.

Correlation of Atmospheric Optical Turbulence and Meteorological Measurements

by

Gail M. Tirrell Vaucher
Physical Scientist, Department of Navy
B.S., Lebanon Valley College, 1981

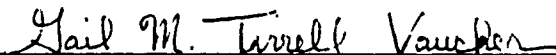
Submitted in partial fulfillment of the
requirements for the degree of

MASTER OF SCIENCE IN METEOROLOGY

from the

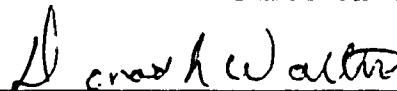
NAVAL POSTGRADUATE SCHOOL
June 1989

Author:

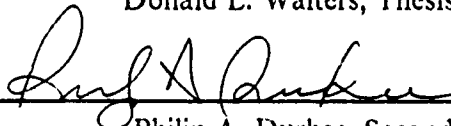


Gail M. Tirrell Vaucher

Approved by:



Donald L. Walters, Thesis Advisor



Philip A. Durkee, Second Reader



Robert J. Renard, Chairman,
Department of Meteorology



Gordon E. Schacher,
Dean of Science and Engineering

ABSTRACT

The correlation of meteorological events such as the jet stream, gravity waves and boundary layer circulation with the optical turbulence parameters, the transverse coherence length r_0 and the isoplanatic angle θ_0 is essential for interpreting and forecasting imaging and laser systems performance. In support of the United State Air Force Relay Mirror Experiment, the Naval Postgraduate School performed a series of six site characterization measurements near Kihei, Maui during August 1987 to July 1988. Spatial and temporal summaries of atmospheric events corresponding to the optical remote sensor data are presented using meteorological data from the National Weather Service Rawinsonde Observation Stations, synoptic charts, GOES-WEST infrared satellite images and four Kihei, Maui rawinsonde datasets. To quantify the correlation between optical turbulence measurements and meteorological phenomena, four methods of calculating C_ζ from rawinsonde data were investigated. Results show that existing rawinsonde systems are inadequate for direct C_ζ calculation. However, moderate improvements in the vertical resolution, the temperature resolution and probe response time will allow direct calculations of optical turbulence parameters from rawinsonde data.



Accession For	
NTIS CRA&I	<input checked="" type="checkbox"/>
DTIC TAB	<input type="checkbox"/>
Unannounced	<input type="checkbox"/>
Justification	
By	
Distribution /	
Availability Codes	
Dist	Avail and/or Special
A-1	

TABLE OF CONTENTS

I. INTRODUCTION	1
II. BACKGROUND	3
A. HISTORICAL REVIEW OF CORRELATION RESEARCH	3
B. THE RELAY MIRROR EXPERIMENT	4
C. HAWAIIAN CLIMATOLOGY	5
1. Climatic Regions of Hawaii	5
2. Circulation	5
3. Temperature, Humidity, Cloud Cover	7
4. Storms	7
III. ATMOSPHERIC OPTICS THEORY	9
A. ATMOSPHERIC INFLUENCE ON LIGHT PROPAGATION	9
B. OPTICAL VARIABLES	11
1. Transverse Coherence Length	11
2. Isoplanatic Angle	12
IV. EXPERIMENT DATA	15
A. RME KIHEI DATA COLLECTION	15
B. KIHEI RME EQUIPMENT	16
1. Optical Equipment	16
2. Meteorological Equipment	16
C. KIHEI SONDE DATA PREPARATION FOR ANALYSIS	17
V. ANALYSIS RESULTS	18
A. STANDARDIZING THE TEMPERATURE PROFILE	18
B. CALCULATING C_2 : FOUR CASE STUDIES	19
1. Case I: Simple Potential Temperature Differences	19
a. Results	19
2. Case II: Using a Running Mean	19
a. 111 Running Mean	20

b. 13531 Running Mean	20
c. r_0 Results	20
d. θ_0 Results	20
3. Case III: Using the Bulk Gradient C_7 Equation	23
a. Results	24
4. Case IV: Using Richardson Number	24
a. Results: Unstable Ri Case ($Ri < 0.25$)	24
b. Results: Conditionally Unstable Ri Case ($Ri < 2.0$)	25
C. CORRELATION OF SENSOR AND CALCULATED PARAMETERS ..	25
D. ERROR ANALYSIS	26
1. Temperature Probe Time Constant Correction	26
a. Application of the Filter	31
2. Sensor/Atmosphere Interaction Noise	32
a. Standard Error Formula	32
b. Vertical C_7 Quantization Noise Simulation	33
3. Implementing Noise and Filter Corrections	33
E. DETERMINING AN ADEQUATE TEMPERATURE RESOLUTION ..	34
F. RUNNING MEAN FITTING ERROR	35
VI. DISCUSSION AND CONCLUSIONS	37
A. CORRELATED OPTICAL DATA AND METEOROLOGICAL EVENTS	37
B. OPTICAL VARIABLES CALCULATED FROM RAWINSONDE DATA	38
VII. RECOMMENDATIONS FOR FUTURE RESEARCH	41
A. LINKING OPTICAL DATA AND METEOROLOGICAL EVENTS	41
B. CALCULATING C_7 FROM RAWINSONDE DATA	42
APPENDIX A. CALCULATED/MEASURED OPTICAL PARAMETERS	43
A. R_0 RESULTS	45
B. Θ_0 RESULTS	49
APPENDIX B. MAUI, HAWAII - AUGUST 1987	53
A. METEOROLOGICAL DATA	53
APPENDIX C. MAUI, HAWAII - DECEMBER 1987	66

A. METEOROLOGICAL DATA	66
APPENDIX D. MAUI, HAWAII - APRIL 1988	78
A. METEOROLOGICAL DATA	78
B. APRIL 1988, EXPERIMENT REPORT	103
1. 0600-1730 UTC 27 April 1988	103
2. 0600-1730 UTC 28 April 1988	104
3. 0600-1730 UTC 29 April 1988	106
4. 0500-1730 UTC 30 April 1988	107
5. 0600-1730 UTC 01 May 1988	108
APPENDIX E. MAUI, HAWAII - JULY 1988	110
A. METEOROLOGICAL DATA	110
LIST OF REFERENCES	141
INITIAL DISTRIBUTION LIST	143

LIST OF TABLES

Table 1. MAIN OPTICAL AND METEOROLOGICAL RME SENSORS	15
Table 2. SINGLE PROBE RESULTS - 0605 UTC 28 APRIL 1988	23
Table 3. MEASURED AND CALCULATED PARAMETERS CORRELATED	26
Table 4. CORRECTING FOR TEMPERATURE PROBE TIME CONSTANT .	31
Table 5. CORRECTING FOR TEMPERATURE PROBE TIME CONSTANT .	31
Table 6. APRIL 1988 KIHAI, MAUI RAWINSONDE LAUNCHES	43
Table 7. JULY 1988 KIHAI, MAUI RAWINSONDE LAUNCHES	43
Table 8. AUGUST 1987 KIHAI, MAUI RAWINSONDE LAUNCHES	53
Table 9. DECEMBER 1987 KIHAI, MAUI RAWINSONDE LAUNCHES	66
Table 10. APRIL 1988 KIHAI, MAUI RAWINSONDE LAUNCHES	78
Table 11. JULY 1988 KIHAI, MAUI RAWINSONDE LAUNCHES	110

LIST OF FIGURES

Fig. 1. Relay Mirror Experiment System Schematic	6
Fig. 2. Diagram of Isoplanatic Angle, θ_0	14
Fig. 3. Profile of Potential Temperature Differences	21
Fig. 4. Potential Temperature Differences Detrended by the 111 Running Mean ..	22
Fig. 5. Initial 2 km of Detrended Potential Temperature Differences	27
Fig. 6. Initial 2 km of Detrended Temperature Differences	28
Fig. 7. Kolmogorov Model vs. Actual Structure Function Curve.	30
Fig. 8. 111 Running Mean Across an Inversion	36
Fig. 9. Measured and Calculated r_0 (All Values Included)	46
Fig. 10. Measured and Calculated r_0 ($Ri < 0.25$)	47
Fig. 11. Measured and Calculated r_0 ($Ri < 2.0$)	48
Fig. 12. Measured and Calculated θ_0 (All Values Included)	50
Fig. 13. Measured and Calculated θ_0 ($Ri < 0.25$)	51
Fig. 14. Measured and Calculated θ_0 ($Ri < 2.0$)	52
Fig. 15. Kihei, Maui Rawinsonde Data: 0658 UTC 18 August 1987	54
Fig. 16. Kihei, Maui Rawinsonde Data: 1440 UTC 18 August 1987	55
Fig. 17. Kihei, Maui Rawinsonde Data: 0722 UTC 19 August 1987	56
Fig. 18. Kihei, Maui Rawinsonde Data: 1103 UTC 19 August 1987	57
Fig. 19. Kihei, Maui Rawinsonde Data: 1512 UTC 19 August 1987	58
Fig. 20. Kihei, Maui Rawinsonde Data: 0607 UTC 20 August 1987	59
Fig. 21. Kihei, Maui Rawinsonde Data: 1011 UTC 20 August 1987	60
Fig. 22. Kihei, Maui Rawinsonde Data: 0650 UTC 21 August 1987	61
Fig. 23. Kihei, Maui Rawinsonde Data: 1106 UTC 21 August 1987	62
Fig. 24. Kihei, Maui Rawinsonde Data: 1559 UTC 21 August 1987	63
Fig. 25. Kihei, Maui Rawinsonde Data: 0541 UTC 22 August 1987	64
Fig. 26. Kihei, Maui Rawinsonde Data: 1053 UTC 22 August 1987	65
Fig. 27. Kihei, Maui Rawinsonde Data: 0950 UTC 5 December 1987	67
Fig. 28. Kihei, Maui Rawinsonde Data: 1552 UTC 5 December 1987	68
Fig. 29. Kihei, Maui Rawinsonde Data: 0639 UTC 6 December 1987	69
Fig. 30. Kihei, Maui Rawinsonde Data: 1131 UTC 6 December 1987	70
Fig. 31. Kihei, Maui Rawinsonde Data: 0517 UTC 7 December 1987	71

Fig. 32. Kihei, Maui Rawinsonde Data: 1624 UTC 7 December 1987	72
Fig. 33. Kihei, Maui Rawinsonde Data: 0537 UTC 8 December 1987	73
Fig. 34. Kihei, Maui Rawinsonde Data: 1031 UTC 8 December 1987	74
Fig. 35. Kihei, Maui Rawinsonde Data: 1557 UTC 8 December 1987	75
Fig. 36. Kihei, Maui Rawinsonde Data: 0345 UTC 9 December 1987	76
Fig. 37. Kihei, Maui Rawinsonde Data: 0958 UTC 9 December 1987	77
Fig. 38. Kihei, Maui Rawinsonde Data: 0610 UTC 27 April 1988	79
Fig. 39. Kihei, Maui Rawinsonde Data: 0610 UTC 27 April 1988	80
Fig. 40. Kihei, Maui Rawinsonde Data: 0610 UTC 27 April 1988	81
Fig. 41. Kihei, Maui Rawinsonde Data: 1548 UTC 27 April 1988	82
Fig. 42. Kihei, Maui Rawinsonde Data: 1548 UTC 27 April 1988	83
Fig. 43. Kihei, Maui Rawinsonde Data: 1548 UTC 27 April 1988	84
Fig. 44. Kihei, Maui Rawinsonde Data: 0605 UTC 28 April 1988	85
Fig. 45. Kihei, Maui Rawinsonde Data: 0605 UTC 28 April 1988	86
Fig. 46. Kihei, Maui Rawinsonde Data: 0605 UTC 28 April 1988	87
Fig. 47. Kihei, Maui Rawinsonde Data: 1549 UTC 28 April 1988	88
Fig. 48. Kihei, Maui Rawinsonde Data: 1549 UTC 28 April 1988	89
Fig. 49. Kihei, Maui Rawinsonde Data: 1549 UTC 28 April 1988	90
Fig. 50. Kihei, Maui Rawinsonde Data: 0605 UTC 29 April 1988	91
Fig. 51. Kihei, Maui Rawinsonde Data: 0605 UTC 29 April 1988	92
Fig. 52. Kihei, Maui Rawinsonde Data: 0605 UTC 29 April 1988	93
Fig. 53. Kihei, Maui Rawinsonde Data: 1558 UTC 29 April 1988	94
Fig. 54. Kihei, Maui Rawinsonde Data: 1558 UTC 29 April 1988	95
Fig. 55. Kihei, Maui Rawinsonde Data: 1558 UTC 29 April 1988	96
Fig. 56. Kihei, Maui Rawinsonde Data: 0544 UTC 30 April 1988	97
Fig. 57. Kihei, Maui Rawinsonde Data: 0544 UTC 30 April 1988	98
Fig. 58. Kihei, Maui Rawinsonde Data: 0544 UTC 30 April 1988	99
Fig. 59. Kihei, Maui Rawinsonde Data: 1434 UTC 30 April 1988	100
Fig. 60. Kihei, Maui Rawinsonde Data: 1434 UTC 30 April 1988	101
Fig. 61. Kihei, Maui Rawinsonde Data: 1434 UTC 30 April 1988	102
Fig. 62. Kihei, Maui Rawinsonde Data: 0703 UTC 7 July 1988	111
Fig. 63. Kihei, Maui Rawinsonde Data: 0703 UTC 7 July 1988	112
Fig. 64. Kihei, Maui Rawinsonde Data: 0703 UTC 7 July 1988	113
Fig. 65. Kihei, Maui Rawinsonde Data: 1537 UTC 7 July 1988	114
Fig. 66. Kihei, Maui Rawinsonde Data: 1537 UTC 7 July 1988	115

Fig. 67. Kihei, Maui Rawinsonde Data: 1537 UTC 7 July 1988	116
Fig. 68. Kihei, Maui Rawinsonde Data: 0536 UTC 8 July 1988	117
Fig. 69. Kihei, Maui Rawinsonde Data: 0536 UTC 8 July 1988	118
Fig. 70. Kihei, Maui Rawinsonde Data: 0536 UTC 8 July 1988	119
Fig. 71. Kihei, Maui Rawinsonde Data: 1612 UTC 8 July 1988	120
Fig. 72. Kihei, Maui Rawinsonde Data: 1612 UTC 8 July 1988	121
Fig. 73. Kihei, Maui Rawinsonde Data: 1612 UTC 8 July 1988	122
Fig. 74. Kihei, Maui Rawinsonde Data: 0605 UTC 9 July 1988	123
Fig. 75. Kihei, Maui Rawinsonde Data: 0605 UTC 9 July 1988	124
Fig. 76. Kihei, Maui Rawinsonde Data: 0605 UTC 9 July 1988	125
Fig. 77. Kihei, Maui Rawinsonde Data: 1527 UTC 9 July 1988	126
Fig. 78. Kihei, Maui Rawinsonde Data: 1527 UTC 9 July 1988	127
Fig. 79. Kihei, Maui Rawinsonde Data: 1527 UTC 9 July 1988	128
Fig. 80. Kihei, Maui Rawinsonde Data: 0556 UTC 10 July 1988	129
Fig. 81. Kihei, Maui Rawinsonde Data: 0556 UTC 10 July 1988	130
Fig. 82. Kihei, Maui Rawinsonde Data: 0556 UTC 10 July 1988	131
Fig. 83. Kihei, Maui Rawinsonde Data: 1532 UTC 10 July 1988	132
Fig. 84. Kihei, Maui Rawinsonde Data: 1532 UTC 10 July 1988	133
Fig. 85. Kihei, Maui Rawinsonde Data: 1532 UTC 10 July 1988	134
Fig. 86. Kihei, Maui Rawinsonde Data: 0550 UTC 11 July 1988	135
Fig. 87. Kihei, Maui Rawinsonde Data: 0550 UTC 11 July 1988	136
Fig. 88. Kihei, Maui Rawinsonde Data: 0550 UTC 11 July 1988	137
Fig. 89. Kihei, Maui Rawinsonde Data: 0926 UTC 11 July 1988	138
Fig. 90. Kihei, Maui Rawinsonde Data: 0926 UTC 11 July 1988	139
Fig. 91. Kihei, Maui Rawinsonde Data: 0926 UTC 11 July 1988	140

ACKNOWLEDGEMENTS

I would like to express my sincere gratitude to Dr. D.L. Walters for his patient advice and instruction in atmospheric optics. A special note of thanks to my parents whose consistent love and encouragement continue to provide a wonderful environment in which to grow. To June A. Favorite and Elizabeth A. Ugorcak, their friendship and assistance with the non-trivial task of transferring large datasets from hardcopy to ASCII files was greatly appreciated. To my husband, Christopher A. Vaucher, for his patient love and support throughout the thesis development - merci. A special thanks for his assistance in generating the "final" form plots for figures 2-8, as well as Appendices B and C. And finally, to my saviour and Lord Jesus Christ: His unchanging love and forgiveness documented in the Bible has helped to maintain perspective while dealing with the many hurdles encountered throughout the master's program. It is my hope that at least some of the many blessings I've received while pursuing the thesis have also been enlightening and encouraging to those with whom I have run this race.

I. INTRODUCTION

Atmospheric turbulence produces optical phase and amplitude fluctuations that seriously degrade laser beam propagation and the performance of imaging systems. In order to perform systems analyses of optical propagation, the spatial and temporal distribution of atmospheric optical turbulence must be understood. Over the past two and a half years optical turbulence measurements in the form of isoplanatic angles, θ_0 , and transverse coherence lengths, r_0 , have been made at a variety of sites in the continental United States, as well as Maui, Hawaii and Vieques, Puerto Rico. Though a dominant application of these measurements involve laser technology and astronomy, the interpretation of the results are very valuable to the meteorologist. The optical data represents an instantaneous summary of the optical turbulence along a vertical path. Imbedded within this vertical cross-section is information describing various synoptic and mesoscale phenomena such as the jet stream, gravity waves, low level jets and boundary layer circulation. By correlating meteorological measurements and optical turbulence parameters, the practical cause and effect relationships can be assimilated into prognostic tools.

The United States Air Force Relay Mirror Experiment (RME) requires a critical evaluation of atmospheric turbulence over the Maui, Hawaii experiment site. RME is designed to "assess how accurately an orbiting mirror can place (a) reflected (laser) beam on a ground target with low beam wander" (Nelson, 1988). Observed beam jitter and wander are a product of both the laser system and the atmospheric turbulence. Accurate measurements of the atmospheric contributions are vital for evaluating the optical system's performance.

Between August 1987 and July 1988, the Naval Postgraduate School (NPS) performed six measurement sessions of approximately one week duration each in order to quantify the RME target board site's optical turbulence characteristics. NPS optical instruments were used to acquire atmospheric coherence length, r_0 , and isoplanatic angle, θ_0 , measurements near sea level at Kihei, Maui. In addition to meteorological data from the National Weather Service Rawinsonde Observation Stations, synoptic charts and the GOES-WEST Infrared Satellite Images, four of the six Kihei data sets had on-site rawinsonde measurements.

This thesis attempts to correlate the RME meteorological measurements with the optical data. Initially, the National Weather Service measurements, charts and satellite images were used to compare meso- and synoptic scale events with the optical results. This method provided qualitative results.

The major thrust of this thesis, however, materialized with the availability of high resolution rawinsonde soundings. These profiles finally provided the resolution necessary for attempting the direct computation of optical parameters from the rawinsonde data. The August and December 1987 sessions used the VIZ WO-8000RP+ rawinsonde system. With a vertical resolution of approximately 35 m, measurements were recorded up to 12 km. The April and July 1988 sessions made use of the Vaisala DigiCORA MW 11 system. This system profiled meteorological data up to approximately 24 km with a sampling rate of 2 seconds (surface to 2 km) and 10 seconds (above 2 km). The 8 m and 40 m vertical resolutions of the DigiCORA system were considered reasonable for computing the optical turbulence directly from the rawinsonde data.

The optical variables measured, r_0 and θ_0 , depend on an integral of the index of refraction structure parameter, C_n^2 , along the vertical path. The parameter C_n^2 is proportional to the temperature structure parameter C_T^2 which can be computed from the rawinsonde data. Four methods for computing the temperature structure parameter C_T^2 from the rawinsonde data were investigated:

1. the Simple Potential Temperature Differences (SPTD) Equation,
2. the Potential Temperature Differences with a Running Mean,
3. the Bulk Gradient Equation (BG) and
4. conditional data sampling based on the Richardson Number.

Each C_T^2 method was tested by calculating r_0 and θ_0 from the C_T^2 profile. These results were ultimately compared to the optical measurements simultaneously acquired over the same site.

II. BACKGROUND

A. HISTORICAL REVIEW OF CORRELATION RESEARCH

International scientific interest in the meteorological influence on "seeing", a rating system based on the angular size of a star image, flourished in the mid to late 50's. Following a brief decline, interest was reestablished in 1962. The new upper atmospheric and outer space environmental data introduced by artificial satellites and space probes provided a catalyst for the development of atmospheric physics. One of the dominant questions addressed by the melange of scientific backgrounds required in the atmospheric physics field involved how meteorological conditions affect "seeing" (Kuchеров, 1966a).

In October 1962, the issue of observatory site selection and related astroclimatic topics were discussed at the International Astronomical Union Symposium held in Rome. Geophysicists, meteorologists and astronomers worked in cooperation to study the interrelationships between atmospheric conditions and astronomical "seeing". Participants resolved that placing telescopes at certain heights above the ground would improve image quality (Kuchеров, 1966a). The following summarizes some of the pertinent articles presented at the Third All-Union Conference held four months earlier in Kiev.

Kuchеров (1966b) observed "shimmer angle" and meteorological conditions at one seashore and two inland sites over a period of approximately two years (1960-1962). The results of that study confirmed the relationship between synoptic fronts (mostly cold fronts) and astronomical "seeing". It should be noted that 25% of the cases display no relationship.

Bol'shakova and Darchiya (1966) investigated the causes of "seeing" condition changes. While they acknowledge the synoptic fronts as an influence on "seeing", they suggest that "seeing" is affected by frontal passages only when air masses with optical characteristics differing from the original advect over the site. Using statistics, they support their claim. To a first approximation, 50% of the cases show the synoptic front causing a deterioration in "seeing", or alternatively, absence of a synoptic front ensures high "seeing" conditions. The rest of the cases display the reverse situation. In their opinion, the analysis must be repeated taking into account the type of front, the incli-

nation of the frontal plane, the direction of the front's motion, and ideally, other detailed meteorological information defined in various atmospheric layers.

Zinchenko (1966) comes to the following conclusions:

1. The lower-atmospheric turbulence is of decisive significance in all that concerns "seeing":
 - a. "optical inhomogeneities are most effective in the ground layer, where the air density is highest;"
 - b. "turbulence intensity is greatest in this layer"; and
 - c. "eddies of minimum size occur in the ground layer".
2. Contradictory results exist with the applicability of Richardson number(Ri) as a criterion of high atmospheric turbulence.

The main reason supporting the latter point is that turbulence intensity is not a single-valued function of Ri , though a dependency on Ri exists. Zinchenko explains, when $Ri < 1$, one can qualitatively accept that turbulence set in; and, the amount of accumulated eddy energy in steady-state conditions increases with the decrease in Ri . (Note: Current understanding requires $Ri < 0.25$ for the above to be true.) Though lack of data prohibited an exact definition of the layer directly responsible for the blurring of the stellar diffraction disks, Zinchenko found that turbulence does show a tendency to be restricted to the 0.5-2.0 km layer.

B. THE RELAY MIRROR EXPERIMENT

The Relay Mirror Experiment (RME) is a United States Air Force Experiment monitored by the Kirtland Air Force Weapons Laboratory, Albuquerque, New Mexico. RME is designed to "assess the ability to place a laser beam on a ground target with low beam wander" (Nelson, 1988). As described by Nelson, RME involves the propagation of three ground to space (uplink) laser beams as well as the reflection from space to ground (downlink) of one of these beams (see Figure 1). Two of the uplink lasers, one from AMOS (Air Force Maui Observatory Station), a site located at the Haleakala crater rim, and the other from Kihei, a site located at the volcano's base, serve to align a relay mirror located on a payload orbiting over the Maui, Hawaii stations. With the mirror aligned, a $1.06 \mu m$ laser travels from AMOS to payload and is relayed down to a hexagonal target board at Kihei. The telescopes and optical detectors on the target board record the centroid motion and beam size of the reflected $1.06 \mu m$ laser beam. Atmospheric turbulence has an important effect on both uplink and downlink beams

(Nelson, 1988). Understanding and characterizing the atmospheric turbulence over the Hawaiian experiment site is crucial for assessing the success of the RME project.

C. HAWAIIAN CLIMATOLOGY

The following is a brief summary of Hawaiian climatology with a focus on the main experiment site in Kihei, Maui.

The tropical island of Maui is located at 156° 15' longitude and 20° 45' latitude (Blumenstock and Price, 1967). The island is the second most southern island in the Hawaiian chain and has an extreme length of 77 km, maximum width perpendicular to extreme length of 42 km and a maximum elevation of 3.1 km. Nicknamed "The Valley Isle", this 1886 square km island is comprised of an isthmus linking two volcanos. The older volcano, Pui Kukui, is in the northwest sector reaching a peak of 1.8 km. To the southeast is the dormant volcano, Haleakala. Though Haleakala defines the island's highest point, it's crater is one of the largest on earth: 12 km long, 4 km wide and about 900 m deep (Creal et al., 1987). Topographically induced high winds crossing the summit are common.

1. Climatic Regions of Hawaii

The tropical climate on Maui varies greatly with location. The dominate sub-climates include the following:

1. Rainy MOUNTAIN slopes on the north, northeast WINDWARD SIDE (above 600 m);
2. Moderately rainy and mild WINDWARD LOWLANDS (below 600 m) to the north, northeast;
3. Dry LEEWARD LOWLANDS to the south, southeast;
4. Sometimes rainy, sometimes dry INTERIOR LOWLANDS between the two volcanic peaks;
5. Dry, cold HIGH MOUNTAINS above 600-900 m (Blumenstock and Price, 1967).

Rainfall measurements reveal the sharp weather contrasts over this island. On the leeward coastal areas such as Kihei, and mountain summits, average annual rainfall is 0.5 m. The lower windward slopes of a high mountain and at/near the summit of lower mountains (western Maui) have an average annual rainfall of 7.6 m (Blumenstock and Price, 1967).

2. Circulation

The dominant atmospheric circulation for the Hawaiian islands is the north-northeasterly trade winds. The prevalence of this flow reflects the seasonal north-south

EXPERIMENT SYSTEM SCHEMATIC

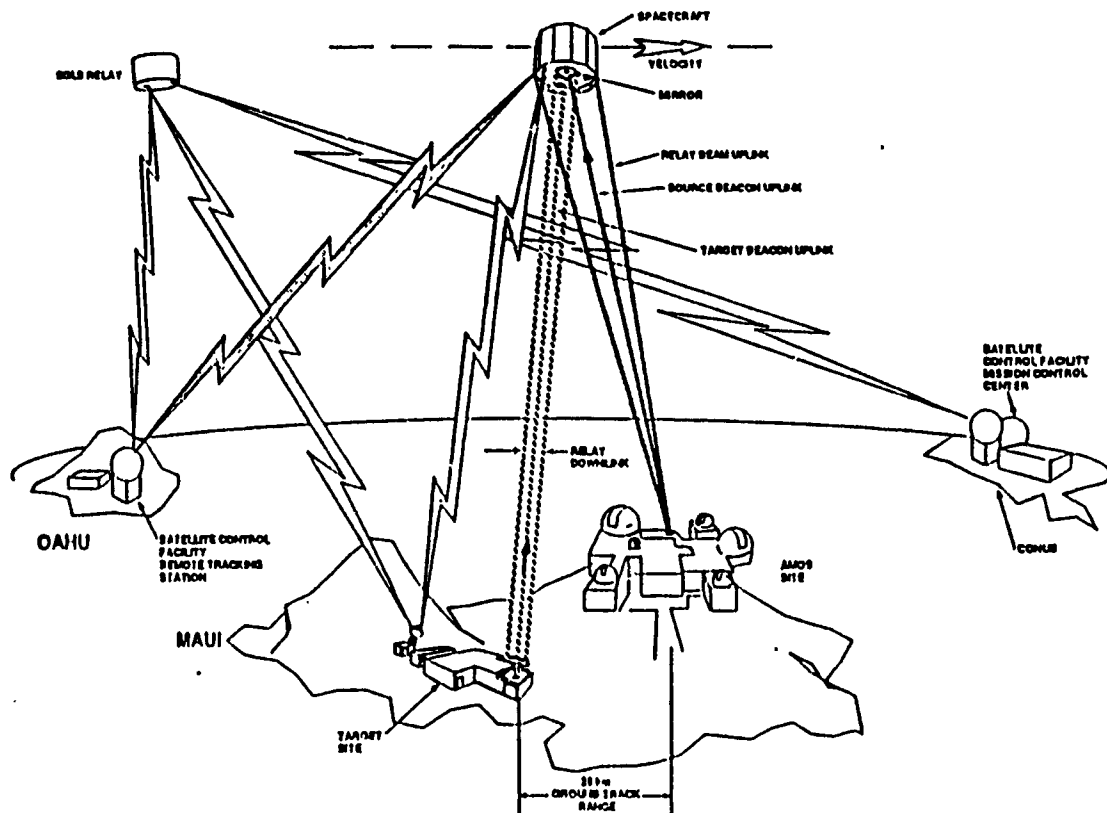


Fig. 1. Relay Mirror Experiment System Schematic

movement of the North Pacific High. From May to September (summer), the North Pacific High is to the north. During this season, the southern sectors of the counter-clockwise flow around the High is such that trades prevail 80-95% of the time. From October to April (winter) the North Pacific High drops south such that the heart of the trades pass well to the south of the islands. The frequency of trades during this season drops to 50-80% (Blumenstock and Price, 1967).

Land and sea breeze circulation occurs on a much smaller scale. Kihei is unique in that land and sea breezes are present even during moderate to strong trades (Blumenstock and Price, 1967). The sometimes brisk sea breezes occur from forenoon to early evening. During the night, a very gentle land breeze flows until shortly after sunrise. The Kihei region also receives a nighttime Katabatic (downslope) flow complementing the land breeze already in progress (personal observation).

3. Temperature, Humidity, Cloud Cover

Hawaii's mean annual temperature range generally fluctuates less than 6 degrees Celsius (Blumenstock and Price, 1967). Daily summer temperatures at 2.5 km are between 4C (nighttime) and 10C (daytime). The winter range at this height is 0-10C. In the lowlands, daytime temperature is between 21-27C, while nighttime is in the 16-21C range. The warmest months in the dry areas such as Kihei are August and September (Blumenstock and Price, 1967).

Generally humid conditions exist with high clouds except in the driest coastal regions and at high elevations. In the absence of synoptic scale events, Kihei begins a day with locally clear skies. A backdrop of clouds clinging to the north and west slopes of Haleakala is common. Throughout the day Kihei experiences a growing and decaying of cloud cover. From sunset to approximately 2000 hours local time, the partly cloudy sky cover over the site dissipates. Because of the dramatic climate changes over such a small island, clouds are generally visible at all hours from the Kihei experiment site in some section of the sky (Blumenstock and Price, 1967).

4. Storms

Generally, Hawaiian weather falls into trade wind and non-trade wind conditions. During trade wind conditions one can expect trade wind showers on the E and NE (windward) coasts; possible light trade wind showers over the S and SW (leeward) areas; and, sea breezes ascending mountain slopes potentially producing light to occasionally heavy showers in the late afternoon and evening. Non-trade wind conditions are associated with light and variable winds; moist air slowly advecting onto the islands from the southeast, south or southwest; intense local storms; and, the possibility of

major and minor storm systems passing through the islands (Blumenstock and Price, 1967).

Major storms for Hawaii fall into one of four classes of disturbances:

1. Cold Front Storms - winter storm systems associated with cold fronts that approach from the northwest end of Hawaii, and move eastward barely reaching Oahu.
2. Kona Storms - winter storm systems similar to cold front storms; winds are generally from "kona" or leeward directions relative to the trades; well-developed kona storms are more widespread and more prolonged than the usual cold front storms.
3. Tropical Storms - similar to hurricanes but with winds below 120 km/hr.
4. Hurricane - the least prevalent storm system; in 63 years only four hurricanes have crossed over the islands. Unlike the Cold Front and Kona Storms, the Tropical Storm and Hurricane can occur at any time. They are most likely to occur, however, between the months of July to December (Blumenstock and Price, 1967).

These events will be discussed in greater detail as they pertain to a specific case study.

III. ATMOSPHERIC OPTICS THEORY

A. ATMOSPHERIC INFLUENCE ON LIGHT PROPAGATION

Light propagates through a medium in the form of a wavefront, "a surface over which an optical disturbance has a constant phase" (Hecht and Zajac, 1974). Fermat's Principle explains that the route light travels will be the smallest Optical Path Length (OPL). This is expressed mathematically as (Hecht and Zajac, 1974)

$$OPL = \int_S^P n(s) ds, \quad (1)$$

where n is the index of refraction (the "speed of an electromagnetic wave in vacuum to that in matter"), and s is the path length. The phase of a propagating wave will be $k = 2\pi/\lambda$ times OPL (Eq. (1)). Optical turbulence arises when the accumulated phase along adjacent paths is different. Phase distortion in the atmosphere occurs when a wavefront encounters random irregularities in the atmosphere's index of refraction. Such irregularities are due to the turbulent mixing processes of the atmosphere. Thus, when a wavefront from a laser propagates vertically through the atmosphere, accumulated, random phase differences will degrade the laser beam and image system performance. Typical atmospheric distortions result in: laser beam centroid wander, scintillation, image breakup and blurring.

The study of these atmospheric random turbulence processes requires the utilization of statistical quantities, means, variances and high moments. Frequently, variances and the higher order moments are not single-valued, unique or even bounded. Also, the atmosphere is neither homogeneous nor isotropic. Kolmogorov and Tatarski introduced the concept of structure functions and local homogeneity to resolve these problems (Tatarski, 1961).

Kolmogorov and Tatarski define the structure function, $D_R(\bar{r})$, for an arbitrary spatially distributed random variable $R(r)$ as

$$D_R(\bar{r}) = \langle [R(\bar{r}_1) - R(\bar{r}_2)]^2 \rangle, \quad (2)$$

where $\bar{r} = \bar{r}_1 - \bar{r}_2$, and the angled brackets indicate an ensemble average of the enclosed quantity. Assuming the random process generating R is homogeneous and isotropic,

then only the magnitude of r is important, $r = |\vec{r}_1 - \vec{r}_2|$. Local homogeneity assumes that the mean $\langle R(r_1) \rangle = \langle R(r_2) \rangle$ (Clifford, 1978). Restricting the separation r to the inertial subrange of turbulence, Kolmogorov (1961) develops a universal form of the single structure function

$$D_R(r) = C_R^2 r^{2/3}, \quad (3)$$

where C_R^2 is a structure parameter, a measure of "the total amount of energy in the turbulence" (Clifford, 1978); r is the distance between the two sampled points; and, r must be between the turbulence innerscale, l_0 , and the turbulence outerscale, L_0 . Eddy sizes below the innerscale correspond to the eddy's energy dissipation through viscous effects. The outerscale corresponds to "the largest scale size for which the eddies may be considered to be isotropic" (Clifford, 1978).

For optical propagation through turbulence, the characterizing quantity is the index of refraction structure parameter (Walters and Kunkel, 1981)

$$C_n^2 = \frac{\langle (n_1 - n_2)^2 \rangle}{r^{2/3}}, \quad (4)$$

where $n_1 = n(r_1)$ and $n_2 = n(r_2)$ are the atmospheric index of refraction at points r_1 and r_2 , respectively. Though C_n^2 is difficult to measure directly, profiles calculated from rawinsonde sensor measurements show that C_n^2 generally decreases with altitude (Nelson, 1988). A more practical approach for measuring atmospheric turbulence is to measure the temperature structure parameter C_T^2 ,

$$C_T^2 = \frac{\langle (T_1 - T_2)^2 \rangle}{r^{2/3}}. \quad (5)$$

Since the atmospheric index of refraction

$$n - 1 = (79 \times 10^{-6}) \frac{P}{T} \quad (6)$$

depends on pressure P and temperature T (Tatarski, 1961), C_n^2 is related to C_T^2 by substituting Eq. (6) in Eq. (4) to get

$$C_n^2 = (79 \times 10^{-6} \frac{P}{T^2})^2 C_T^2, \quad (7)$$

assuming turbulence is isobaric. Specific methods for calculating C_ζ will be discussed in Chapter 5.

B. OPTICAL VARIABLES

As described earlier, the laser beam is affected by atmospheric turbulence as a result of index of refraction fluctuations along the turbulent propagation path. Two parameters that characterize the optical turbulence generated by the atmosphere are: the transverse coherence length, r_0 , and the isoplanatic angle, θ_0 .

1. Transverse Coherence Length

The transverse coherence length, r_0 , is a measure of the lateral autocorrelation length of the electric field propagating through the turbulent atmosphere. Because of the Fourier transform properties of an imaging system, r_0 is also a measure of the spatial frequency response of the atmosphere, the atmospheric modulation transfer function (MTF). Viewed as a component of a linear system, the atmosphere acts like a low pass filter suppressing the high spatial frequencies, or details of an image.

The perturbation theory developed by Tatarski and extended by Fried (1966) and Lutomirski and Yura (1971) shows that the long term, modulation transfer function of the atmosphere is expressed in terms of the wave structure function D by

$$MTF(v) = \exp\left(\frac{-D(\lambda f v)}{2}\right), \quad (8)$$

where v is the spatial frequency in cycles/m, λ is the wavelength of light and f is the focal length of the optical system. For a plane wave, D has the form

$$D(\rho) = 2.91 k^2 \rho^{5/3} \int_0^L C_n^2(z) dz, \quad (9)$$

where k is $2\pi/\lambda$, the wavenumber; $\rho = |\vec{r}_1 - \vec{r}_2| = \lambda f v$, a distance measured at the entrance pupil of the optical system, L is the optical path length and C_n^2 is the index of refraction structure parameter.

The general format of $MTF(v)$ is $\exp(-a\rho^{5/3})$ where a is a turbulence and wavelength scaling parameter. $MTF(v)$ is frequently written as:

$$MTF(v) = \exp\left[-3.44\left(\frac{\lambda f v}{r_0}\right)^{5/3}\right] = \exp\left[-3.44\left(\frac{\rho}{r_0}\right)^{5/3}\right], \quad (10)$$

representing Fried's (1966) version of the long term atmospheric modulation transfer function. Equivalently, Lutomirski and Yura's (1971) mutual coherence function (MCF) is

$$MCF(\rho) = \exp \left[- \left(\frac{\rho}{\rho_0} \right)^{5/3} \right], \quad (11)$$

where ρ_0 is an autocorrelation length of the electric field.

The parameters r_0 and ρ_0 are different measures of the electromagnetic (EM) wave's coherence as restricted by the atmospheric turbulence. They are related by

$$r_0 = 3.44^{3/5} \rho_0 = 2.1 \rho_0. \quad (12)$$

Using Eq. (8) and (9), the coherence length for a plane wave, r_0 becomes

$$r_0 = 2.1 [1.46 k^2 \int_0^L C_n^2(z) dz]^{-3/5}. \quad (13)$$

The parameter r_0 represents the distance traverse to the direction of propagation where, on average, the correlation of the electric field is $e^{-3.44}$ (Fried, 1966).

To interpret r_0 consider the following:

1. For an optical aperture d smaller than the coherence length, the electric field across the aperture is coherent. The angular resolution will be proportional to λ/d .
2. For an optical aperture larger than the coherence length, the correlation across the aperture is limited to regions of r_0 or ρ_0 (depending on how the correlation is defined). The EM intensities across the aperture will add (energy is conserved). The optical system's average angular resolution will be proportional to λ/r_0 (Walters, Favier and Hines, 1979).
3. Visually, for apertures smaller than r_0 , atmospheric turbulence results in image centroid motion, a process called, "tilt". In telescopes larger than r_0 , the image is broken up into multiple speckels, each associated with a r_0 sized region. The angle λ/r_0 determines the overall envelope of the complex image.
4. With respect to measuring the atmospheric optical turbulence, large r_0 values, such as 200-400 mm, indicate a small amount of optical turbulence is present along the integrated path. Conversely, small r_0 magnitudes, such as 20-40 mm, imply a large amount of optical turbulence exists along the integrated path.

2. Isoplanatic Angle

The isoplanatic angle, θ_0 , is an angular measurement of spatial coherence between two intersecting rays (Walters, 1985). Given two light sources a small angle θ

apart, the random atmospheric phase fluctuations along the two paths are different. Figure 2 displays rays r_{21} and r_{31} interacting with three different turbulence patches. At the atmosphere top the two paths undergo unique path distortions. At the surface (near point 1), the turbulent interaction is common to both rays. θ_0 is the angle between rays r_{21} and r_{31} such that the accumulated phase fluctuations are correlated to within e^{-1} of a perfect correlation.

Fried (1982) develops a mathematical representation for θ_0 for apertures $d \gg r_0$:

$$\theta_0 = [2.91 k^2 \int_0^\infty C_n^2(z) z^{5/3} dz]^{-3/5}, \quad (14)$$

where k is $2\pi/\lambda$, wavenumber of light; C_n^2 is the refractive index structure parameter; and, z is the altitude from the ground.

Typical C_n^2 profiles display a rapid decrease with altitude. The $z^{5/3}$ term is significant in that it emphasizes the optical turbulence at higher altitudes. The net product of these two terms (the integrand) results in a profile of relatively constant values from a few kilometers to 10 – 15 kilometers (Walters, 1985).

The practical interpretation of θ_0 is similar to r_0 . When θ_0 magnitudes are small ($1-2 \mu$ rad), the optical turbulence along the integrated path and especially around the tropopause level is large. Conversely, when θ_0 values are large ($14-20 \mu$ rad), optical turbulence is small.

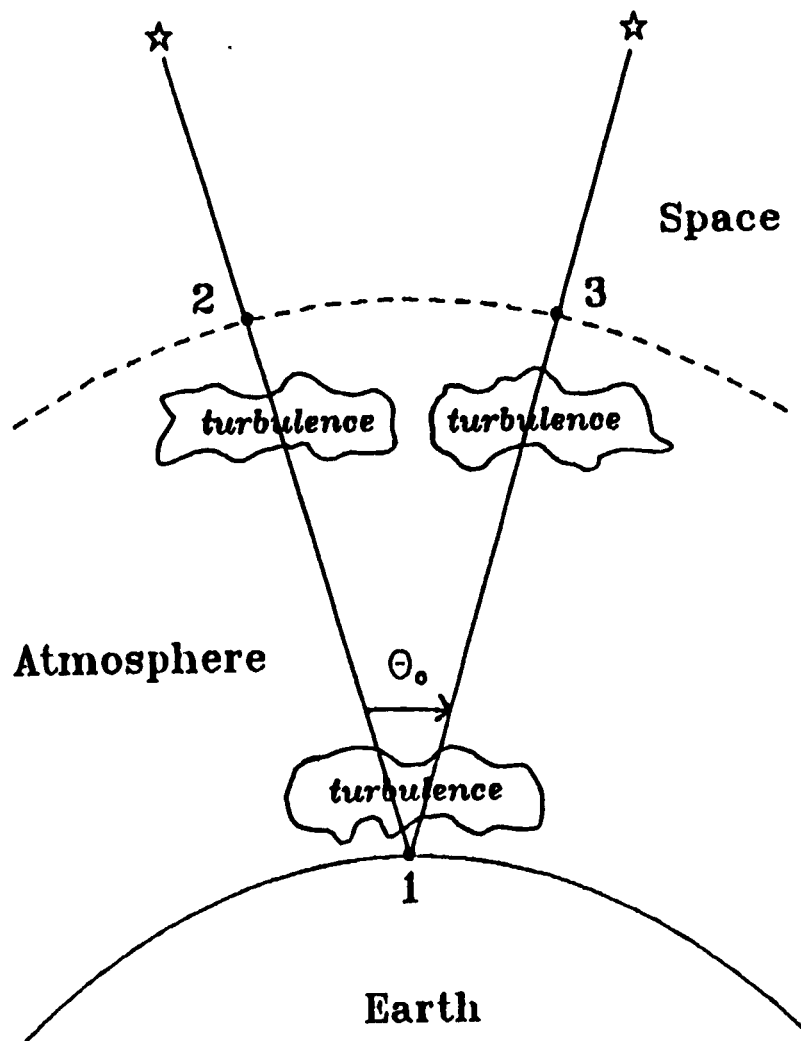


Fig. 2. Diagram of Isoplanatic Angle, θ_0 .

IV. EXPERIMENT/DATA

A. RME KIHAI DATA COLLECTION

The initial sampling of isoplanatic angles, θ_0 , took place on the summit of Mt. Haleakala in Maui, Hawaii. These measurements commenced on 17 September 1985 and concluded on 1 February 1986. Simultaneous meteorological surface measurements at the site provided some understanding of localized atmospheric events. A year and a half later, both θ_0 and r_0 were measured at the base of Haleakala (at approximately sea level), in Kihei. Six sampling sessions of four and five nights took place between August 1987 and July 1988. Two Hawaii Rawinsonde Observation stations, Hilo and Lihue, provided raw data listings for each of the 1987-1988 cases. Additional on-site rawinsonde launches supplemented the optical data for four out of the six sessions (Table 1). The meteorological data for the August and December 1987 experiments used the VIZ WO-8000RP+ rawinsonde system with 10-second vertical resolution. The April and July 1988 experiments employed the Vaisala DigiCORA MV/ 11 system with 2- and 10-second vertical resolution. All four cases used the OMEGA Navigational Network for wind measurements. Intermittent GOES-WEST Infrared Satellite Images complimented the rawinsonde data for all the cases. The primary focus of this study will be on the April and July 1988 experiments, due to the higher vertical resolution provided by the DigiCORA dataset.

Table 1. MAIN OPTICAL AND METEOROLOGICAL RME SENSORS

EXPERIMENT DATES	OPTICAL DATA		RAWINSONDE SITES		
	θ_0 (μ rad)	r_0 (mm)	Hilo, Hawaii	Lihue, Kauai	Kihei, Maui
17 Sep 85-1 Feb 86	X				
18-22 Aug 87	X	X	X	X	X
24-27 Oct 87	X	X	X	X	
5-9 Dec 87	X	X	X	X	X
27 Feb- 1 Mar 88	X	X	X	X	
27 Apr- 1 May 88	X	X	X	X	X
7-11 July 88	X	X	X	X	X

B. KIHEI RME EQUIPMENT

1. Optical Equipment

Optical measurements were taken by an isoplanometer and transverse coherence length sensor designed/built by Dr. D.L. Walters, NPS. For specific details on each instrument the reader should pursue Stevens (1985) for the isoplanometer and Walters, Favier, and Hines (1979) for the transverse coherence length sensor. Isoplanatic angles were measured by an isoplanometer mounted on a portable 200 mm Celestron telescope. The software was run on an HP 217 computer. Isoplanometer data were automatically sampled once every second and displayed real-time on a time verses isoplanatic angle plot. Before storing the data, the samples were converted into 10 second averages. The complete isoplanatic angle system is capable of operating independent of human interaction for 1-3 hours provided polar alignment is perfect and the chosen star's zenith angle does not exceed 40 degrees.

The transverse coherence length sensor was mounted onto a portable 355 mm Celestron telescope. Software used for real-time processing required an operator to evaluate the image and stellar positioning before each sample. This added interface with a trained researcher served to suppress instrumental artifacts. The average sampling rate was between 1-2 minutes/sample. Processed data were stored on an HP 300 series computer.

2. Meteorological Equipment

Meteorological measurements specific to this thesis were a product of the Vaisala DigiCORA MW 11. This solid state, digital design rawinsonde package integrates the receiver, data processors and operator display into one unit. High speed precision sensors permit rapid sampling (at approximately 2 second intervals) resulting in high density data acquisition. The 95 mm by 145 mm (approximate size) RS 80 Rawinsonde (Navaid Radiosonde) package was launched on an unravelling tether attached to a 200 gm balloon filled with helium. Pressure values were measured by a BAROCAP pressure sensor, a steel capacitive aneroid with a resolution of 0.1 hPa and an accuracy of 0.5 hPa. Temperature sampling was taken by a THERMOCAP sensor, a small capacitive bead in a glass casing. Resolution of the THERMOCAP was 0.1C; accuracy was 0.2C. The HUMICAP, a thin film humidity sensor, measured humidity with a resolution of 1% relative humidity (RH) and an accuracy of 2% RH. According to the Vaisala Ref. A0435, this sensor produced a reliable response even in low temperatures and after exposure to condensation. The measuring range published was 0-100% RH (Vaisala, 1986a).

The commutation between the sensors and the transducer electronics was accomplished by a digital electronic switch. A water activated battery provided the RS 80 "sonde" with a light weight power supply capable of keeping the package activated for the entire surface to 30 km (balloon permitting) launch sequence (Vaisala, 1986b).

The telemetry frequency was between 400-406 MHz. Wind data for this experiment were calculated from the OMEGA Navigational System. The RS 80 received signals from the OMEGA Navaid Network (11-14 kHz), superimposed this information onto the thermodynamic data and relayed the sampling to the DigiCORA MW 11 (Vaisala, 1986b).

C. KIHEI SONDE DATA PREPARATION FOR ANALYSIS

The initial form of the DigiCORA MW 11 rawinsonde output used in this research began as a hardcopy listing of time in minutes and seconds, height in meters, pressure in millibars, temperature in Celsius, relative humidity in percent, dewpoint temperature in Celsius, mixing ratio in grams per kilogram, wind speed in knots and wind direction in degrees. Using a Dest PCSCAN scanner, the powerful IBM mainframe XEDIT, a software package capable of transferring IBM files to a IBM PC-AT, and the instant graphics display of QUATTRO, the initial hardcopy was duplicated as an ASCII file.

Thermodynamic sampling rate for the first two kilometers was every two seconds. Beyond this threshold, sampling continued once every 10 seconds. Due to the limitations in the Omega Navigational system, winds were measured every 10 seconds throughout the launch. A linear interpolation between the 10-second wind measurements was applied to the initial two kilometers remedying the inconsistent sampling rate.

Variables calculated from the raw data include potential temperature, potential temperature gradient, shear, Richardson number, C_T^2 , C_n^2 , r_0 and θ_0 .

V. ANALYSIS/RESULTS

To strengthen the link between the measured optical parameters and the meteorological data collected, a number of methods for calculating r_0 and θ_0 values were pursued. As explained earlier, both r_0 and θ_0 are a function of C_n^2 , which, in turn, is a function of C_T^2 (see Chapter 3). In this chapter, four methods for calculating C_T^2 from rawinsonde data will be investigated. However, the first step is to define an appropriate conservative temperature quantity to be used in the C_T^2 calculation.

A. STANDARDIZING THE TEMPERATURE PROFILE

An air parcel vertically displaced in the atmosphere experiences a temperature change as the parcel's pressure equalizes with the ambient environment (Clifford, 1978). Permitting the air to be moist but unsaturated, and assuming the atmosphere is in hydrostatic equilibrium, the rate at which the lifted parcel's temperature will decrease is the dry-adiabatic lapse rate. This is approximately 9.767°C/km. If the parcel is saturated, the release of latent heat produces a lapse rate that is less than the dry-adiabatic lapse rate (Huschke, 1970). For this study, it is important to work with conservative variables, a variable that is independent of position in space. As described above, temperature does not fit this description. The conservative quantity (independent of position) best suited is potential temperature (Clifford, 1978). By definition, potential temperature is "the temperature which the parcel of air would have if it were expanded or compressed adiabatically from its existing pressure and temperature to a standard pressure p_0 (generally taken as 1000mb)" (Wallace and Hobbs, 1977). In short, the temperatures sampled vertically are standardized to one pressure level. Mathematically, the potential temperature expression is

$$\Theta = T \left(\frac{P_0}{P} \right)^{\frac{R}{C_p}}, \quad (15)$$

where Θ is potential temperature in kelvin, T is temperature in kelvin, P_0 is a standard pressure such as 1000mb, P is pressure in millibars, R is the gas constant for dry air and C_p is the specific heat of dry air at constant pressure (1.005 J/g K) (Huschke, 1970). Note: Following the usual convention, C_T^2 shall hereafter be written in place of C_θ^2 (Clifford, 1978).

B. CALCULATING C_T^2 : FOUR CASE STUDIES

1. Case I: Simple Potential Temperature Differences

Case I takes the given mathematical definition,

$$C_T^2 = \frac{\langle [(\Theta_2 - \bar{\Theta}_2) - (\Theta_1 - \bar{\Theta}_1)]^2 \rangle}{r^{2/3}} \quad (16)$$

and assumes $\bar{\Theta}_2 = \bar{\Theta}_1$. Physically, this presumes homogeneity between neighboring samples. In other words, the samples are taken within the inner and outerscale of the turbulent layer (Tatarski, 1961). Note: the angled brackets indicate an ensemble average of the enclosed quantity. Associated with the above and all the cases hereafter is the assumption that the sampled layer is isotropic (Tatarski, 1961).

Unlike most C_T^2 calculations, the dataset employed by this research consists of vertical temperature samples. For the above assumption to be true, the rate of sampling must be sufficiently high with respect to the potential temperature gradients. If the sampling rate is too slow, trends in potential temperature will show up in the differences, $(\Theta_2 - \Theta_1)$. Figure 3 displays such trends first between 2 and 5 km then again above 12 km. Note: The large increase in potential temperature differences in the stratosphere was found in all the profiles examined.

a. Results

Using the entire potential temperature profile for the C_T^2 calculations, the eight April 1988-Kihei rawinsonde flights and the ten July 1988-Kihei launches all under estimate the direct r_0 and θ_0 measurements by a factor of ten. (See Appendix A) This is expected considering the trends in the potential temperature differences. As demonstrated in Figure 3, these trends generate differences approaching 2 K near the boundary layer top. In the stratosphere (above 15 km), potential temperature differences are even larger. For this particular profile, the stratospheric potential temperature differences reach as much as 4 K. When these large differences are blindly used to calculate C_T^2 , the result is a deceptively large over estimation of C_T^2 . The over estimated C_T^2 subsequently leads to an under estimation of r_0 and θ_0 .

2. Case II: Using a Running Mean

Case II investigates the effects of detrending the potential temperature profile prior to calculating C_T^2 . The two representative high pass filters selected for this case include the equally weighted 111 Running Mean (R.M)

$$X_i = \frac{1X_{i-1} + 1X_i + 1X_{i+1}}{3} \quad (17)$$

and the weighted 13531 Running Mean

$$X_i = \frac{1X_{i-2} + 3X_{i-1} + 5X_i + 3X_{i+1} + 1X_{i+2}}{13} \quad (18)$$

Figure 4 displays the potential temperature difference profile after the 111 RM has been subtracted from the original potential temperature profile. There is still an increase in potential temperature differences around the boundary layer, however, the peak values of approximately 0.3 K is balanced with an adjacent value of about -0.3 K. Even the stratosphere appears nearly symmetrical between ± 0.7 K.

a. 111 Running Mean

The implementation of the equally weighted (111) RM handles the DigiCORA's two- to ten-second sampling rate transition by using values equally spaced in time when available. When data are unavailable, preference is given to the "central" point. Profile endpoints are ignored. For two-second data the filter takes into account layers between 15-30 meters thick. Ten-second data involves layers of 90-120 meters.

b. 13531 Running Mean

The 13531 running mean filter accommodates the two- to ten-second sampling rate change with preference given first to data equally spaced in time, and second, to the central point. Endpoints are noted, but generally ignored.

c. r_0 Results

Both RM methods produce r_0 values within the same order magnitude as the optical sensor values. With few exceptions, the relatively large and small magnitude variations present in the optical sensor data are traced by both RM results. The 13531 RM generate values approximately 16% larger than the 111 RM. The error between the 111 RM and sensor results ranges from 13% to 55%. The 13531 RM under estimates the sensor values by 4% to 48%. When the C_7 profile detrended by the 111 RM is truncated just below the stratosphere's large C_7 increase, r_0 increases by only 11%. Table 2 displays a sample of these results.

d. θ_0 Results

While large scale magnitude changes recorded by the sensor are virtually ignored, the calculated θ_0 values are within the same order of magnitude as the sensor. The range of sensor measurements is from 3 to 7.5 μ rad. Values calculated from the

0605 UTC 28 April 88

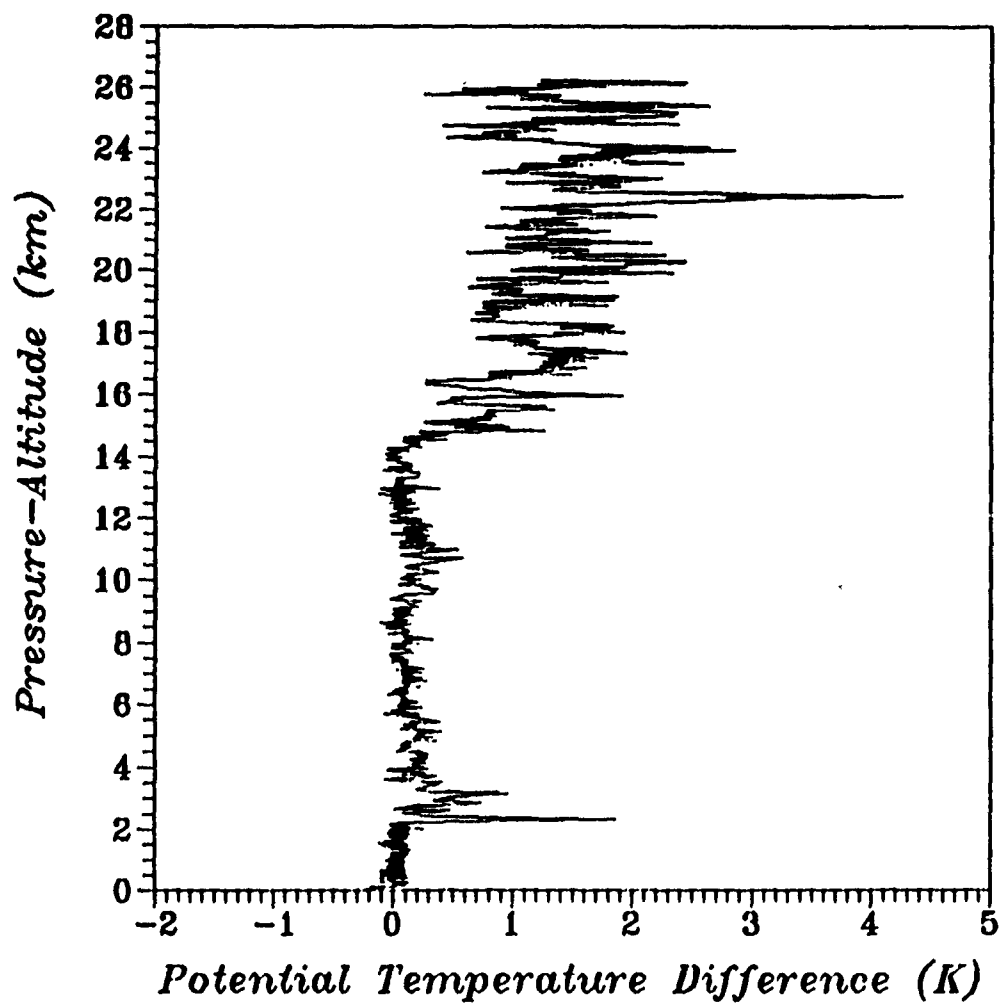


Fig. 3. Profile of Potential Temperature Differences

0605 UTC 28 April 88

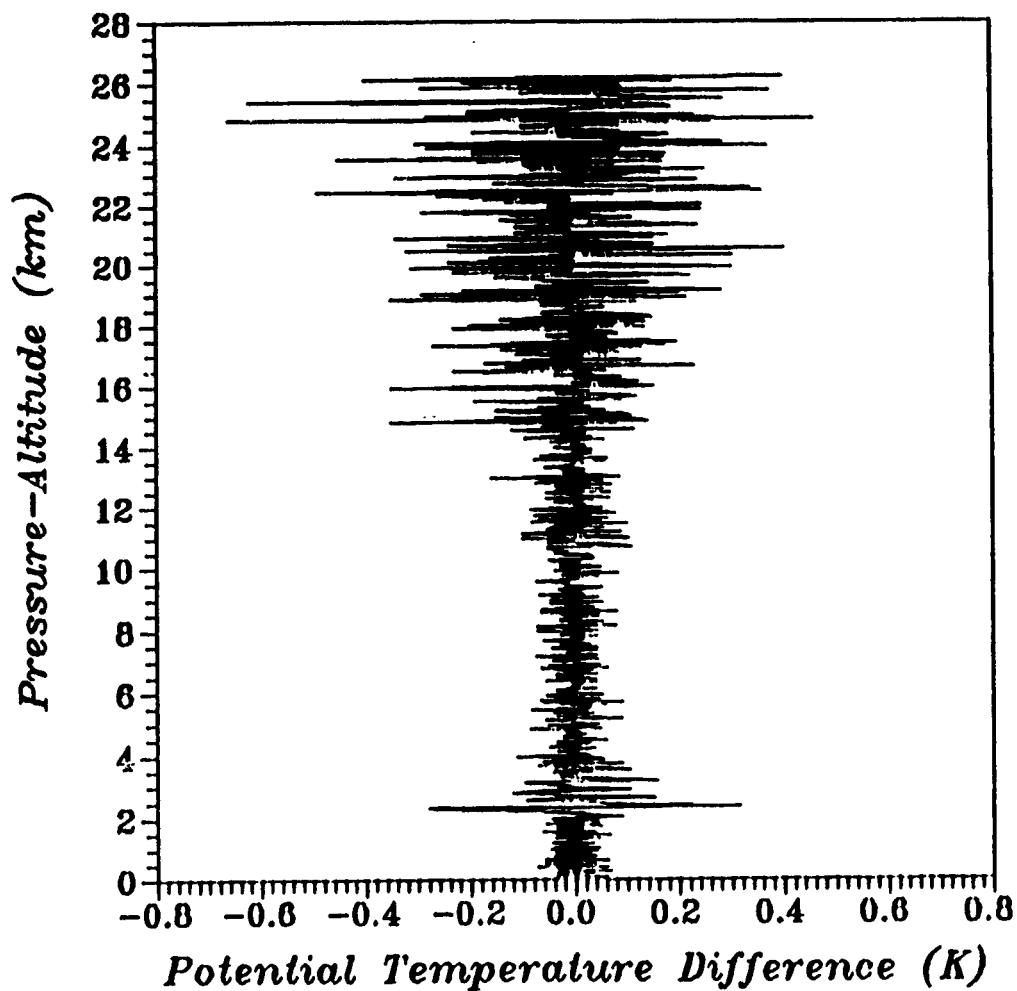


Fig. 4. Potential Temperature Differences Detrended by the 111 Running Mean

111 RM cover a range of 0.7-1.3 μ rad. (The 8.5 μ rad of flight 5, July 88 is ignored.) θ_0 calculated with the 13531 RM ranges from 0.8-1.5 μ rad. Truncating the detrended C_T^2 profile just below the stratosphere's large C_T^2 increase, increases θ_0 by 78%. A sample of these results is in Table 2.

Table 2. SINGLE PROBE RESULTS - 0605 UTC 28 APRIL 1988

C_T^2 CALCULATION METHOD	r_0 (mm)	θ_0 (μ rad)
SPTD (all values)	8	0.2
BG (all values)	7	0.2
111 RM (all values)	36	1.3
111 RM (troposphere only)	40	2.3
13531 RM (all values)	38	1.5
SENSOR VALUES	43	3

3. Case III: Using the Bulk Gradient C_T^2 Equation

The third approach incorporates an expression developed by Tatarski (1961) that relates C_T^2 to bulk parameters of the atmosphere. This expression which will hereafter be referenced as the "Bulk Gradient C_T^2 " equation (BG) is,

$$C_T^2 = a \alpha L_0^{4/3} (d\Theta/dz)^2, \quad (19)$$

where a is a constant; α is the ratio of eddy thermal diffusivity to eddy viscosity; L_0 is the outerscale length; and, $(d\Theta/dz)^2$ is the potential temperature gradient. Because L_0 is not universally well-defined and $d\Theta/dz$ is also vague with respect to the resolution needed to properly define the derivative, the values calculated from BG are suspect. The main strength of the expression is that it accentuates the strong dependence C_T^2 has on the square of the temperature gradient. This term also provides the "atmospheric density inhomogeneity susceptible to being mixed by the wind turbulence" (Walters and Kunkel, 1981). Assumptions made when applying this equation include the following:

1. The atmosphere is mechanically turbulent. Note the lack of a shear term.
2. The outerscale, L_0 , is half the distance between samples.
3. Constant, a , is 2.8.
4. Ratio, α , is 1.

a. Results

The BG r_0 and θ_0 results are one-tenth the sensor measurements. Both optical parameters calculated in this case closely trace those values generated by the Simple Potential Temperature Differences (SPTD) Case. r_0 magnitudes vary over a range of 6-8 mm. θ_0 values cover a range of 2-3 mm. These values are within 7% of the SPTD case. Considering the dominant term of the BG equation is the potential temperature gradient, it is not surprising to discover the final results are so closely associated to Case I. An explanation for why r_0 and θ_0 values are off by a factor of 10 begins with a re-evaluation of the assumptions. The constant, a , has a suggested range between 2.8 to 3.2. Shifting this to the higher constant will not accommodate the discrepancy. Changing the outerscale length to the full thickness of the layer serves only to decrease r_0 and θ_0 . Justifying an outerscale smaller than half the thickness of the layer sampled taps into the fundamental problem with the C_T calculations. That is, vertical resolution. The sampled values are too far apart to provide the temperature gradient information needed to drive this C_T equation properly. Decreasing the outerscale length without simultaneously decreasing the thickness of the sampled layer is illogical. As in Case I, the BG results indicate a need for either detrending the data prior to calculating C_T or using a rawinsonde dataset capable of producing more detailed temperature gradient information.

4. Case IV: Using Richardson Number

C_T is a constant representing the total amount of energy in a turbulent layer (Clifford, 1978). The vertical temperature samples measured by the rawinsonde are not always taken from turbulent layers. To computationally isolate only those atmospheric layers which are turbulent, the Richardson number, Ri , was used. Richardson number is "the ratio of work done against gravitational stability to energy transferred from mean to turbulent motion" (Huschke, 1970). When $Ri < 0.25$, the layer is unstable and C_T is calculated using the SPTD, Running Mean and BG approaches, respectively. When $Ri \geq 2$, the layer is stable and no C_T calculation is made. "Critical" conditions exist when $0.25 \leq Ri < 2.0$. As the final case reviewed, C_T is calculated when $Ri < 2.0$.

a. Results: Unstable Ri Case ($Ri < 0.25$)

Letting a turbulent layer be defined as one having a $Ri < 0.25$, each of the above three methods for calculating C_T was conditionally computed. With remarkable consistency, all three methods over estimate r_0 . r_0 values farthest from the sensor's value generally are produced by the SPTD case. Except for one extreme case where r_0 is calculated as greater than 360 mm from the sensor value, the SPTD r_0 values are generally 2 to 3 times too large. The BG method leads to values that are approximately 7% closer

than SPTD to the sensor value. The RM method(s) r_0 values over estimate the sensor by 18 to 71 mm for the 13531 RM and 8 to 58 mm for the 111 RM.

θ_0 calculations generate less consistent results. The sequence of greater to smaller magnitudes seen in the r_0 results does not hold for θ_0 . About 40% of all the θ_0 data calculated for Case IV ($Ri < 0.25$) over estimate the sensor's measurement; 50% under estimate θ_0 ; and, 10% straddle the sensor value (see Appendix A).

b. Results: Conditionally Unstable Ri Case ($Ri < 2.0$)

With the inclusion of more atmospheric layers in the r_0 integral, one would expect the resulting magnitude to be smaller. For the most part this is true. The SPTD and the BG cases respond in the same manner. Their r_0 values under estimate the sensor by 17-80% for the SPTD case and 22-65% for the BG case. The 111 and 13531 RM calculations still over estimate r_0 with the 13531 RM slightly higher than the 111 RM (See Appendix A). The magnitude of the results as compared to the sensor's value is generally within 78% for 13531 RM and 59% for the 111 RM.

θ_0 results display a pattern consistent with the "All Values" results. The largest to smallest θ_0 magnitudes calculated are: (Sensor Value), 13531 RM, 111 RM, SPTD and BG. All values are less than $3 \mu \text{ rad}$! As before the large magnitude variations observed in the sensor data are virtually ignored in the calculated data.

C. CORRELATION OF SENSOR AND CALCULATED PARAMETERS

Correlating the measured and calculated optical parameters for each case discussed in section-B generates r-squared values between 0.0009 and 0.5. Table 3 lists r-squared values for each case. Note: r-squared is 1 for a perfect correlation.

The lack of good correlation demands a review of the sensor's ability to sample values for C_T^2 calculations. After detrending the potential temperature profile with a 111 RM, potential temperature differences for the two-second data are plotted. (See Figure 5) Initially, this profile appears to contain valid turbulence information. Repeating this procedure with the temperature (K) profile (Figure 6), however, unveils a major problem. The systematic $\pm 0.03 \text{ K}$ oscillation dominating the profile implies that the temperature differences below 2 km are predominantly quantization noise from the 0.1°C temperature resolution. Comparing Figure 5 and Figure 6 shows that the potential temperature calculation introduces additional errors that obscure the quantizing error. Rather than pursue a detailed correlation analysis, attention is diverted to 1) identifying and quantizing the major sources of error, and 2) providing recommendations for a temperature sensor/system more suited for calculating C_T^2 .

0605 UTC 28 April 88

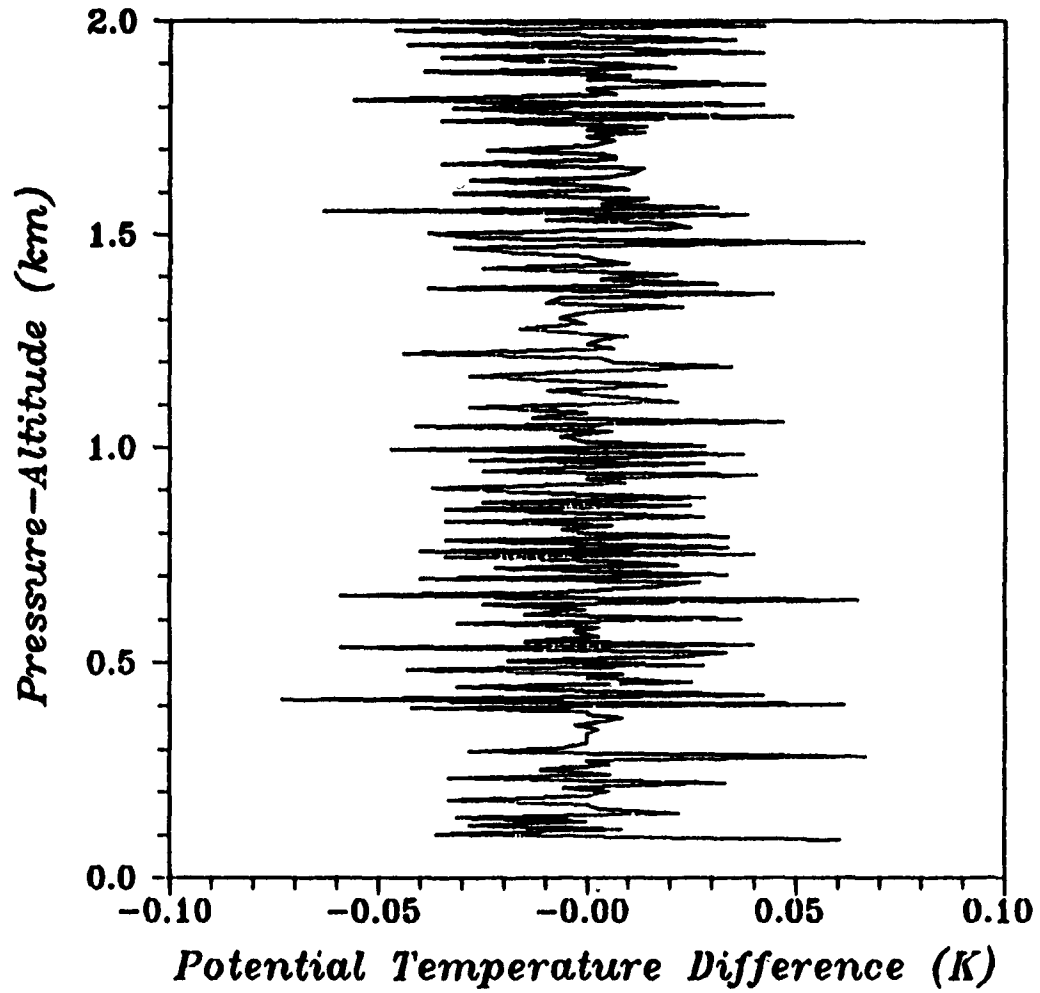


Fig. 5. Initial 2 km of Detrended Potential Temperature Differences

0605 UTC 28 April 88

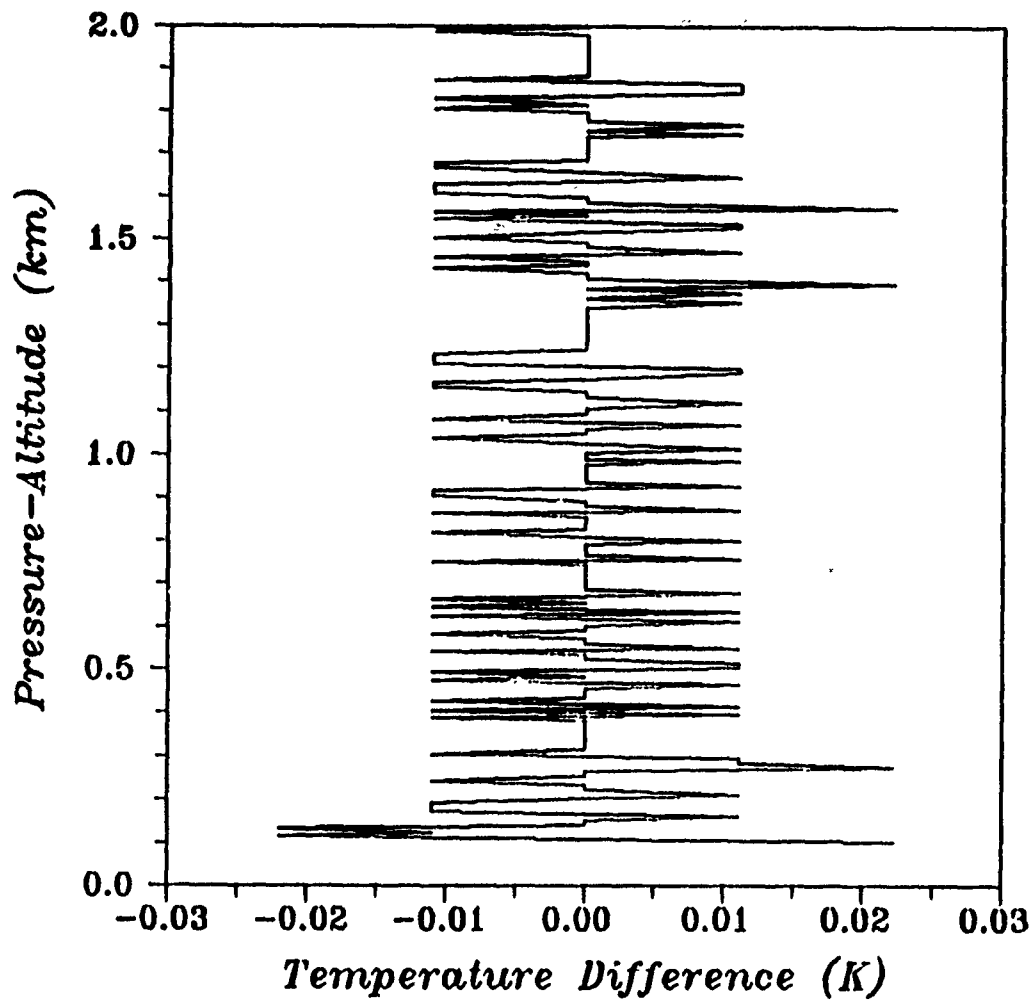


Fig. 6. Initial 2 km of Detrended Temperature Differences

Table 3. MEASURED AND CALCULATED PARAMETERS CORRELATED

R-SQUARED VALUES	r_0 (mm)			θ_0 (μ rad)		
C_7^2 CALCULATION METHOD	ALL Values	Ri < 0.25	Ri < 2.0	ALL Values	Ri < 0.25	Ri < 2.0
SPTD	0.009	0.3	0.5	0.05	0.3	0.02
BG	0.009	0.3	0.4	0.05	0.3	0.02
111 RM	0.005	0.0009	0.06	0.01	0.2	0.1
13531 RM	0.002	0.001	0.07	0.07	0.2	0.2

D. ERROR ANALYSIS

1. Temperature Probe Time Constant Correction

In both the April 88 and July 88 soundings, the temperature was measured with a capacitive bead. For sensor specifications see Chapter 4. To calculate the sensor response time τ , the following equation was used:

$$1/\tau = A + B\sqrt{v}, \quad (20)$$

where v is velocity, A is the constant for the calm atmosphere ($v = 0$) and B is a constant at velocity, v . For this particular probe, the sensor time constant at a velocity of 6 m/s is 2.5 s. With an ascent rate of 4 m/s, τ increases to approximately 3 s. In order to calculate the error induced by the temperature sensor time constant, the structure function of the probe system with limiting scale lengths must be compared to the structure function over all scale lengths.

Mathematically, the structure function over all scale lengths is (Tatarski, 1961):

$$D(r, 0, \infty) = 4 \int_0^\infty \sin^2(kr/2) k^{-5/3} dk, \quad (21)$$

where k is $2\pi/\lambda$, λ the turbulent wavelength and r the probe separation distance.

The structure function filtered by a one pole, low pass filter is (Hunten, 1964):

$$D(r,a,b) = 4 \int_a^b \frac{\sin^2(kr/2)k^{-5/3}}{1 + (\omega\tau)^2} dk, \quad (22)$$

where

a is $2\pi/L_0$, the limiting lower frequency (outerscale, L_0),

b is $2\pi/l_0$, the limiting upper frequency (inner scale, l_0),

ω is kV where V is the wind velocity (rawinsonde's ascent rate) and

τ is the time constant of the temperature probe (the upper frequency cutoff).

The $\omega\tau$ term in the denominator attenuates the high spatial frequencies. Since the $k^{-5/3}$ term increases at low wavenumber, Eq. (22) is much more sensitive to the selection of an outerscale than the innerscale. Test calculations of the $D(8m,a,b)$ integral confirm that an innerscale of 0.1 m versus 0.001 m produce virtually identical results. When varying the outerscale from 10 m to 1000 m (all other parameters of $D(8m,a,b)$ remaining unchanged), the 1000 m structure function is 200 times larger than for the 10 m.

With an inner scale of 0.1 m, an outerscale of 1000 m and a 3-second temperature probe time constant, the DigiCORA's 2-second data is 15% of the actual C_τ^2 present. The structure parameter C_τ^2 , calculated from the 10-second data is 54% of the actual C_τ^2 value. While the 10-second data appears to produce results more than three times closer to the desired values, this is somewhat deceptive. The larger time interval between samples (ascent rate is constant) results in a greater probe separation distance. Consequently, higher spatial frequencies or rapid changes in the potential temperature will be missed. This aliasing of temperature measurements is one of the major difficulties with calculating structure function parameters from rawinsonde data.

Another problem with calculating a structure function D from 10 second ($r=40$ m) data involves a limitation of the Kolmogorov $r^{2/3}$ slope model. D is a function of the probe separation distance, r , and the outerscale. For r values comparable to the outerscale, the actual $D(r)$ deviates from Kolmogorov's model. When r is larger than the outerscale, the measured (actual) structure function will be smaller than the D calculated from Kolmogorov's model. (See Figure 7) The significance of this problem is that the calculated D under estimates the actual turbulence present when r is greater than the outerscale. Thus, accepting the calculated C_τ^2 as 54% of the actual C_τ^2 present is done cautiously.

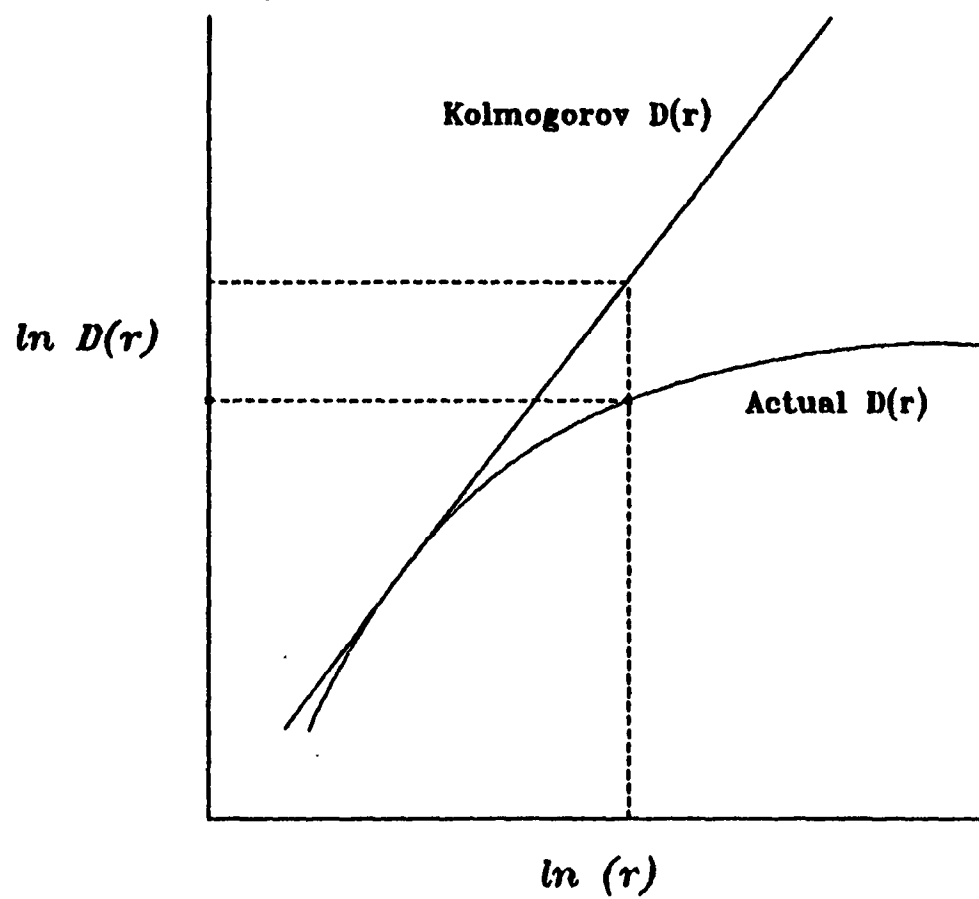


Fig. 7. Kolmogorov Model vs. Actual Structure Function Curve.

a. Application of the Filter

Correcting the basic C_T equations for the temperature probe time constant produces an even greater over estimation of atmospheric turbulence. The magnitudes of the filtered r_0 and θ_0 (all values) decrease 35-50% from the unfiltered values. Table 4 and Table 5 display the results taken from two rawinsonde datasets: 0605 UTC 28 April 1988 and 1434 UTC 30 April 1988. Imposing this correction onto the calculation of the optical parameters where $Ri < 0.25$ and $Ri < 2.0$ produce the same 35-50% decrease as the "All Values" cases. Unless otherwise noted, further reference of correction implementation will be done on the 0605 UTC 28 April 1988 Kihei, Maui rawinsonde dataset.

Table 4. CORRECTING FOR TEMPERATURE PROBE TIME CONSTANT

0605 UTC 28 April 1988	r_0 (mm)		θ_0 (μ rad)	
C_T Calculation Method	Uncor- rected	Corrected	Uncor- rected	Corrected
SPTD-All Values	8	5	0.2	0.1
BG-All Values	7	5	0.2	0.1
111 RM-All Values	36	20	1.3	0.9
13531 RM-All Values	38	22	1.5	1.0
SENSOR VALUES	48	48	3	3

Table 5. CORRECTING FOR TEMPERATURE PROBE TIME CONSTANT

1434 UTC 30 April 1988	r_0 (mm)		θ_0 (μ rad)	
C_T Calculation Method	Uncor- rected	Corrected	Uncor- rected	Corrected
SPTD-All Values	8	4	0.2	0.1
BG-All Values	8	4	0.2	0.1
111 RM-All Values	33	16	1.2	0.8
13531 RM-All Values	37	19	1.3	0.9
OPTICAL SENSOR VALUES	54	54	7	7

2. Sensor/Atmosphere Interaction Noise

Since the optical parameters calculated by the rawinsonde are smaller than the optical sensor values and compensation for the probe response-time accentuates this problem, some other large error source must be present. Noise introduced by the sensor-atmosphere interaction is such a source. Two methods attempt to quantize this phenomena.

a. Standard Error Formula

The first approach tackles the problem by focusing on the limitations of the rawinsonde system. In other words, knowing the resolution of each variable measured, how well can the given instruments measure atmospheric turbulence? This method uses the standard error formula which for a function $E(x,y,z)$ is (Bevington, 1969):

$$\sigma_E^2 = \left(\frac{\partial E}{\partial x}\right)^2(\sigma_x)^2 + \left(\frac{\partial E}{\partial y}\right)^2(\sigma_y)^2 + \left(\frac{\partial E}{\partial z}\right)^2(\sigma_z)^2. \quad (23)$$

Applying the standard error formula to the SPTD calculation of C_T^2 produces

$$\sigma_{C_T^2}^2 = 4 \left[\frac{(T_2 - T_1)}{(z_2 - z_1)^{2/3}} \right]^2 [\sigma_{T_2}^2 + \sigma_{T_1}^2] + \frac{4}{9} \left[\frac{(T_2 - T_1)^2}{(z_2 - z_1)^{5/3}} \right]^2 [\sigma_{z_2}^2 + \sigma_{z_1}^2]. \quad (24)$$

Note: T_2 and T_1 are assumed to generate independent random errors.

With C_T^2 defined as

$$C_n^2 = (79 \times 10^{-6} \frac{P}{T^2})^2 C_T^2. \quad (25)$$

the system induced error for C_n^2 is

$$\sigma_{C_n^2}^2 = \left[\frac{(79 \times 10^{-6})^4 P^2}{T^8} \right] \left[(P \sigma_{C_T^2})^2 + \left(\frac{4 P C_T^2 \sigma_T}{T} \right)^2 + (2 C_T^2 \sigma_P)^2 \right]. \quad (26)$$

Implementing the error correction reveals three layers where $(C_T^2 - \sigma_{C_T^2}) \leq 0$. These results imply that the measurement uncertainties are comparable to the measurements. The sensitive regions include 0 to 2 km, 4.5 to 9.5 km and 12 to 14 km. However, the area of major concern is near the surface where the majority of turbulence is measured. Eliminating the 0-2 km layer would result in a gross under estimation of turbulence which ultimately generates large r_0 and θ_0 . Since by definition C_T^2 can not be less than zero, all negative error corrections are assumed to be zero.

The results from the C_n^2 error calculation show values less than or equal to 0 near the surface (0 - 2 km). Between 3.5 - 9.5 km, as well as, 10 - 14 km, the $C_n^2 \leq 0$ condition is intermittent. Unlike the C_T^2 calculation, C_n^2 has a pressure term that effectively minimizes the influence of any values above the tropopause. Thus, the main concern is with turbulence measurements near the surface.

The average C_T^2 structure parameter, including sensor error (0605 UTC 28 April 1988), is $(1.1 \pm 1.8) \times 10^{-3} K^2 m^{-2/3}$ for the 0 - 2 km two-second data; the average $C_n^2 \pm$ sensor error over this same region is $(8 \pm 13) \times 10^{-16} m^{-2/3}$. The 10-second data (2 km and above) produces an average $C_T^2 \pm$ sensor error of $(7.4 \pm 0.8) \times 10^{-2} K^2 m^{-2/3}$; the average C_n^2 , including sensor error for the 10-second data, is $(2.0 \pm 0.4) \times 10^{-15} m^{-2/3}$. Clearly, the 0-2 km data are buried in uncertainties.

b. Vertical C_T^2 Quantization Noise Simulation

The second technique used for quantizing the roundoff error in the SPTD (Simple Potential Temperature Differences) calculation of C_T^2 simulates the atmosphere's temperature profile with a straight line slope of -0.007 K/m. This technique (Walters, 1989) includes a correlation between adjacent temperature samples that is ignored in the standard error approach. The 0.1 K temperature resolution produces a quantization noise of $1.4 \times 10^{-3} K^2 m^{-2/3}$ for the two-second data and $6.8 \times 10^{-3} K^2 m^{-2/3}$ for the ten-second data. The two-second noise is 22% less than the Standard Error Function's result. The ten-second value is the same. Running the simulation on a detrended potential temperature profile, the calculated noise for C_T^2 is a factor of 10 smaller than the SPTD calculation. Specifically, the two- and ten-second quantization noises are $6.2 \times 10^{-4} K^2 m^{-2/3}$ and $1.4 \times 10^{-4} K^2 m^{-2/3}$, respectively.

3. Implementing Noise and Filter Corrections

The measured C_T^2 is

$$C_{T_{measured}}^2 = (Filter \times C_{T_{actual}}^2) + Noise, \quad (27)$$

where the Filter is the temperature probe time constant correction, and Noise is the vertical C_T^2 quantization noise from the simulation.

Applying the noise correction to the 111 RM C_T^2 calculation for the 0605 UTC 28 April 1988 rawinsonde flight, the original 36 mm r_0 calculated by this method increases to 46 mm (all values included). The sensor value is 48 mm. Replacing all negative C_T^2 with zero reduces this measurement to 41 mm. Imposing the temperature probe

time constant correction reduces this value again to 36 mm (all values included) and ultimately r_0 is 25 mm including only positive C_T^2 values.

θ_0 displays a much smaller range of results due to the equation's sensitivity for values at the tropopause coupled with a lack of large variation created by the noise and filter at that level. Specifically, θ_0 starts as 1.3 μ rad (only the 111 R.M applied). Including all values and subtracting out the quantization noise increases θ_0 to 1.4 μ rad. Removing all negative C_T^2 does not change the calculated measurement. Dividing the noise-free C_T^2 by the filter leads to a value of 1.0 μ rad (all values). And finally, using only positive C_T^2 , the θ_0 result remains 1.0 μ rad. The sensor's measurement is 3 μ rad.

E. DETERMINING AN ADEQUATE TEMPERATURE RESOLUTION

The $(0.1 \pm 0.05)K$ temperature probe resolution dominates the error term in Eq. (24). An important consideration is to determine the temperature resolution required for calculating C_T^2 from rawinsonde data. First, let $\sigma_{C_T^2} = 1 \times 10^{-4} Km^{-2/3}$. A C_T^2 noise level of $1 \times 10^{-4} Km^{-2/3}$ is adequate for most measurements. Assuming the temperature difference is 0.0098 K over a 1 meter height difference (dry-adiabatic lapse rate), and that $\sigma_{z_2} = \sigma_{z_1} = 0$, one can solve for σ_T^2 . Note: $\sigma_{T_2}^2 = \sigma_{T_1}^2$. The result is $\sigma_T^2 = 1.30 \times 10^{-5} K^2 m^{-2/3}$. The roundoff error (noise) temperature variance expression (Bose, 1985)

$$\sigma_T^2 = \frac{1}{12} 10^{-2d}, \quad (28)$$

where d is the number of base ten significant digits to the right of the decimal point remaining after roundoff, permits the calculation of significant digits required for a given variance. Solving for d , the resolution necessary for a $\sigma_{C_T^2} = 1 \times 10^{-4} Km^{-2/3}$ is approximately two decimal points remaining after roundoff, 0.01K resolution. Repeating the above procedure with a $\Delta T/\Delta z$ of $-0.007K/1m$ (a lapse rate observed in the Kihei dataset), the results are also approximately two.

The initial use of the standard error formula defined σ_T as 0.05 K, as implied by the sensor specifications. The roundoff error temperature variance expression calculates σ_T as 0.03 K. When 0.03 K is used in the C_T^2 standard error formula, the product is approximately one-third the magnitude of the standard error formula using 0.05 K. This decrease in the C_T^2 noise term increases C_T^2 . A larger C_T^2 leads to a larger C_n^2 and, subsequently a smaller r_0 and θ_0 . Since the calculated optical parameters are already under estimating the sensor values, this adjustment only confirms that the current temperature sensor/system is at best marginally acceptable for calculating C_T^2 .

F. RUNNING MEAN FITTING ERROR

A fitting error around sharp gradients, such as across inversions, arises when implementing the running mean into the C_T^2 calculation. The running mean is unable to follow the trends. Figure 8 displays the large difference that occurs between the running mean and a given profile. Though variances are used in the C_T^2 calculation, the variances are artificially enlarged by the poor fit across the inversion. The SPTD experiences a form of this fitting problem that results in aliasing. (See Section D1 of this chapter).

0605 UTC 28 April 88

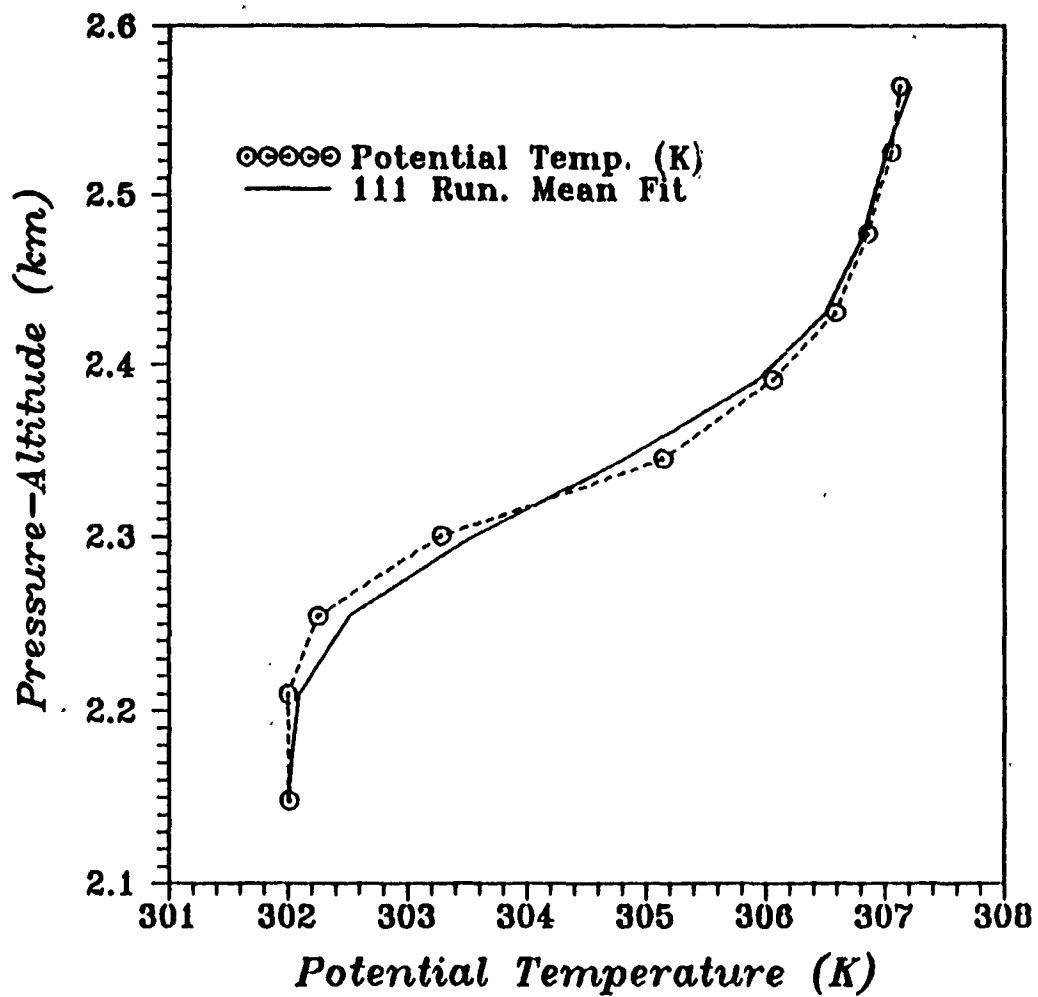


Fig. 8. 111 Running Mean Across an Inversion

VI. DISCUSSION AND CONCLUSIONS

A. CORRELATED OPTICAL DATA AND METEOROLOGICAL EVENTS

Optical and meteorological data for the Relay Mirror Experiment (RME) were collected between 1985-1988 in Kihei, Maui, Hawaii. Reviewing the composite Kihei optical dataset reveals the Maui site as "mediocre" to "poor". While upward and downward trends occur, the predominant transverse coherence length values generally stay within the 50 to 70 mm range.

The lack of extremely good values (e.g., 200-400 mm) is tied to the turbulent, 3-5° C boundary layer inversion 2-3 km above the Kihei site. Except in the winter, north-northeasterly trades usually cap the boundary layer. The interface between the 4 to 7 m/s trades and the boundary layer provides the mechanical turbulence detrimental to optimum "seeing" conditions for light propagation. The concept of the boundary layer introducing optical turbulence is supported by Gossard (1985). Using fast-response turbulence sensors traversing a 300m tower, he shows a turbulent layer of approximately $0.01 K^2 m^{-2/3}$ to exist just below the inversion. This implies that the greatest mixing of air masses with different temperatures (turbulence) is at the base of the boundary layer inversion.

Kihei has a land/sea breeze even during the "trade wind" season (see Chapter 2, Section C). This daily shift of circulation generating a warm, convective air mass over Kihei in the daytime followed by a cool, relatively dry environment at night renders the mediocre r_0 measurements. Katabatic flow off of the 3.1 km high Mt. Haleakala is another turbulence producing mechanism observed at the Kihei site.

Profiling the atmosphere over Kihei during summer conditions, one expects a land/sea breeze circulation, a boundary layer inversion, trade winds, a second moist layer aloft and a moderate jet stream. The shear surrounding any jet is a source of turbulence exhibited in the r_0 magnitudes. Shear provides the mechanical mixing necessary for optical turbulence, however, without the compliment of a strong temperature gradient, the effect on the optical regime is weakened. This is best exemplified by reviewing the summer trade season optical measurements collected when an upper-level jet is traversing the site (weak temperature gradient). The θ_0 measurements, which are sensitive to turbulence in the 300 to 200 mb jet stream level, are rarely below 3 μ rad. Note: 3 μ rad is considered poor optical conditions. The exception to the rule for Maui occurs when

a synoptic-scale event crosses overhead, tightening the temperature gradient associated with the jet (see Appendix D). A stronger example is examining the influence of a polar jet. The tighter temperature gradient and subsequently stronger winds associated with the polar jet are able to drive θ_0 measurements down to 1 to 2 μ rads, a very turbulent environment optically. An example of this was in the 10 December 1985 Haleakala data, where θ_0 was measured as 1.6 μ rad.

One of the most optically active Hawaiian cases occurs in April 1988, a winter case. The Kihei site experiences the passage of a low or "eddy". A detailed discussion of the optical and meteorological conditions throughout that experiment is found in Appendix D.

B. OPTICAL VARIABLES CALCULATED FROM RAWINSONDE DATA

During four of six RME experiments at Kihei, Maui on-site rawinsonde launches were released. Two sessions employed the use of a Vaisala DigiCORA MW 11 Rawinsonde System. The eight April 1988 launches and ten flights recorded in July 1988 began with a two-second sampling rate up to 2 km, followed by a ten-second sampling rate for the remainder of the flight. All 18 vertical profile sets were utilized for testing four distinct C_7 calculation methods. The final rating of each method was done by using the C_7 profile to calculate the two optical parameters, r_0 and θ_0 . These calculated values were compared to the optical measurements acquired simultaneously with the rawinsonde launch.

The first two methods, the Simple Potential Temperature Differences (SPTD) and the Bulk Gradient (BG), produced similar results. Both over estimated the turbulence leading to an under estimation of r_0 and θ_0 by a factor of 10.

Using the entire profile, the 111 and 13531 running mean techniques produced r_0 and θ_0 values of the same order magnitude as the sensor values. The r_0 data even showed a general ability to match the relatively large and small magnitude variations observed in the sensor data. θ_0 calculated from the running mean methods were generally insensitive to the magnitude changes measured by the isoplanometer. However, the calculated values were within the same order of magnitude as the sensor. Overall, the 13531 running mean provided turbulence parameters at least 16% closer to the sensor values than the 111 running mean.

Using the Richardson number to isolate the turbulent layer from the non-turbulent brought mixed results. Conditioning the C_7 profile by calculating turbulence for layers with $Ri < 0.25$ generated r_0 two to three times larger than the sensor. The BG Case

provided values approximately 7% closer to the sensor. The running mean approaches were within 8-71 mm of the sensor. θ_0 calculations for SPTD, BG and running mean generated results such that about 40% over estimated the sensor's θ_0 ; 50% under estimated; and, 10% straddled the sensor value.

The conditionally unstable results ($Ri < 2$) for the SPTD Case under estimated the r_0 sensor by 17-80%.

Poor correlation between the calculated and measured optical parameters revealed the existence of serious problems. Limitations in the current sensor/system prevented successful C_T calculations. The limitations were broken down into three areas:

1. Excessive Temperature Probe Response Time,
2. Limited Vertical Resolution (aliasing) and
3. Limited Temperature Resolution (Roundoff Error).

The limited temporal resolution of the DigiCORA MW 11 rawinsonde profiles was confirmed by calculating the temperature probe time constant correction. For the 2-second data, only 15% of the actual C_T was measured. While the 10-second filter displayed 54% of the actual C_T , this was deceptive. The distance between 10-second samples produced aliasing effects when the mean potential temperature gradient was large. This inability to resolve high frequencies artificially enlarged the already over estimated turbulence present. In addition, this large 40-45 m separation approached the Kolmogorov outerscale.

The 2-second data was not as susceptible to aliasing. Instead, the 0.1 K temperature resolution (roundoff error) introduced quantization noise. Using two distinct procedures, the standard error formula and a vertical C_T quantization noise simulation model, noise corrections of $6.2 \times 10^{-4} K^2 m^{-2/3}$ (2-second data) and $1.4 \times 10^{-4} K^2 m^{-2/3}$ (10-second data) were calculated. Application of this correction confirmed that the C_T values in the initial 2 km of data were mostly quantization noise. Because most optical turbulence is expected near the surface, this realization was not encouraging.

Another major problem with calculating C_T from rawinsonde data was insufficient vertical resolution that produced a fitting problem with the running mean case. Just as the inability to resolve higher frequencies (aliasing) produced an over estimation of C_T for the SPTD Case, this effect became even more apparent when the running mean methods encountered a 3-5 ° C inversion with a 10-second sampling rate. This enhanced the existing over estimation of turbulence. In contrast, turbulence calculated across the

sharp temperature shift (inversion) captured within the 2-second data (1537 UTC 7 July 1988) did not appear to suffer from this difficulty.

VII. RECOMMENDATIONS FOR FUTURE RESEARCH

A. LINKING OPTICAL DATA AND METEOROLOGICAL EVENTS

Quantizing the optical turbulence based on weather conditions is a non-trivial project. As simultaneous optical and meteorological observations accumulate, the possibility of plotting "weather" charts of $iso - r_0$ and $iso - \theta_0$ lines nears reality. Such a task, however, requires at least two phases of investigation. The first deals with synoptic-scale events. Major atmospheric phenomena affecting optical propagation include: the passage of cold and warm fronts, the polar and subtropical jets, high and low pressure systems, and so on. A dedicated climatological study (spanning many years) of optical parameters during each of these events, with measurements taken at one location, would provide a statistical sample from which ranges of values could be determined. Being realistic, a more cost effective and time efficient approach for acquiring a (marginally) valid statistical sample is to design a set of experiments with multiple (minimum 3, preferable 5) r_0 and θ_0 sensors. The geometric shape formed by 4 of the sensor site locations would be a square. The sides of this square would be along the prevailing winds and measure a kilometer or more in length. The fifth sensor would be in the center of this box. Time based cross-sections would be derived from three of the sensors. Because the central site is common to both possible cross-sections, this sensor would be the most critical.

The meteorological sensors needed for simultaneous measurements would depend on the particular event being studied. For example, the passage of a cold front would require surface meteorological stations, rawinsondes and satellite resources. The effect of a polar jet would require rawinsondes, aircraft and satellite data. The main objective is to pinpoint optical measurements (processed in real time) with the movement of the weather phenomena. Armed with at least three "clean" case studies of a specific weather event, r_0 and θ_0 ranges for various sectors of the specified event would be possible.

The second area of investigation involves the meso- and microscale weather activities. Though weather phenomena on these scales are often site specific, one major source of optical distortions common to all sites is the boundary layer. The influence of the boundary layer has been estimated as 30-50%. A simultaneous data collection at the surface and above the boundary layer inversion would better quantize the importance of this atmospheric structure. Because Mt. Haleakala is over 3 km high, such a

project could theoretically be done in Maui. However, Haleakala's Crater experiences a local jet. Therefore, the measurements above the boundary layer inversion would have to be sampled sufficiently far from this accelerated flow. Another possible location is along the central California coast where r_0 values have often been recorded to be more than 200 mm. A dedicated study contrasting the good "seeing" conditions above and below the boundary layer interface may provide a better resolution for this question.

Another meteorological phenomena at the mesoscale is gravity waves. With the current method of data acquisition for the isoplanometer, tracing the influence of gravity waves in real-time is possible. This ability coupled with the mobility of the isoplanometer could be of value to gravity wave studies.

B. CALCULATING C_T FROM RAWINSONDE DATA

Another approach to resolving the correlation of optical turbulence and meteorological conditions is to calculate key optical parameters (such as r_0 and θ_0) directly from rawinsonde data. Currently, one of the main obstacles is the need for a low cost temperature probe and operating system capable of acquiring large high resolution data bases. An adequate single probe rawinsonde temperature sensor would require a 0.01-0.02 K resolution, 100 msec response time and a 1 m vertical resolution. These specifications are not unreasonable with current technology. Some method of detrending the potential temperature profile with a running mean still will be necessary until 0.1-0.2 m vertical resolution is possible.

An interesting experiment would be to launch a rawinsonde with both the above recommended single temperature probe and the more expensive two temperature probe sensor. The latter has been discussed in Olmstead (1988). A comparison of the two C_T profiles generated from these methods would help to calibrate the less expensive single probe method.

As personal computers become faster and high data-acquisition rate rawinsonde packages become routine, the theoretical concept of evaluating and predicting the optical turbulence over any site in real time will evolve and become a reality.

APPENDIX A. CALCULATED/MEASURED OPTICAL PARAMETERS

The optical variables r_0 (transverse coherence length) and θ_0 (isoplanatic angle) depend on an integral of C_n^2 along the vertical path. The refractive structure parameter C_n^2 is proportional to the temperature structure parameter C_T^2 which can be computed from the rawinsonde data. Four methods for computing the temperature structure parameter C_T^2 from the rawinsonde data include:

1. the Simple Potential Temperature Differences (SPTD) Equation,
2. detrending the potential temperature differences with a 111 Running Mean (111 RM) or a 13531 Running Mean (13531 RM),
3. the Bulk Gradient Equation (BG) and
4. conditional data sampling based on the Richardson Number ($Ri < 0.25$ and $Ri < 2.0$).

Each C_T^2 method was tested by calculating r_0 and θ_0 from the C_T^2 profile. These results were ultimately compared to the optical measurements simultaneously acquired over the same site.

Table 6 and Table 7 correlates the flight numbers referenced in the Appendix A plots with their rawinsonde launch time (UTC).

Table 6. APRIL 1988 KIHAI, MAUI RAWINSONDE LAUNCHES

FLIGHT NO.	TIME (UTC)	DATE (DAY MON YR)
1	0610	27 April 1988
2	1548	27 April 1988
3	0605	28 April 1988
4	1549	28 April 1988
5	0605	29 April 1988
6	1558	29 April 1988
7	0544	30 April 1988
8	1434	30 April 1988

Table 7. JULY 1988 KIHAI, MAUI RAWINSONDE LAUNCHES

FLIGHT NO.	TIME (UTC)	DATE (DAY MON YR)
1	0703	7 July 1988
2	1537	7 July 1988
3	0536	8 July 1988
4	1612	8 July 1988
5	0605	9 July 1988
6	1527	9 July 1988
7	0556	10 July 1988
8	1532	10 July 1988
9	0550	11 July 1988
10	0926	11 July 1988

A. R_0 RESULTS

Figure 9 through Figure 11 display the r_0 values calculated from the eight April 1988 and ten July 1988 Maui rawinsonde datasets. An estimate of the r_0 simultaneously measured over the same Kihei, Maui site is also included.

For the measured r_0 time series corresponding to these profiles, see Nelson (1988).

Transverse Coherence Length

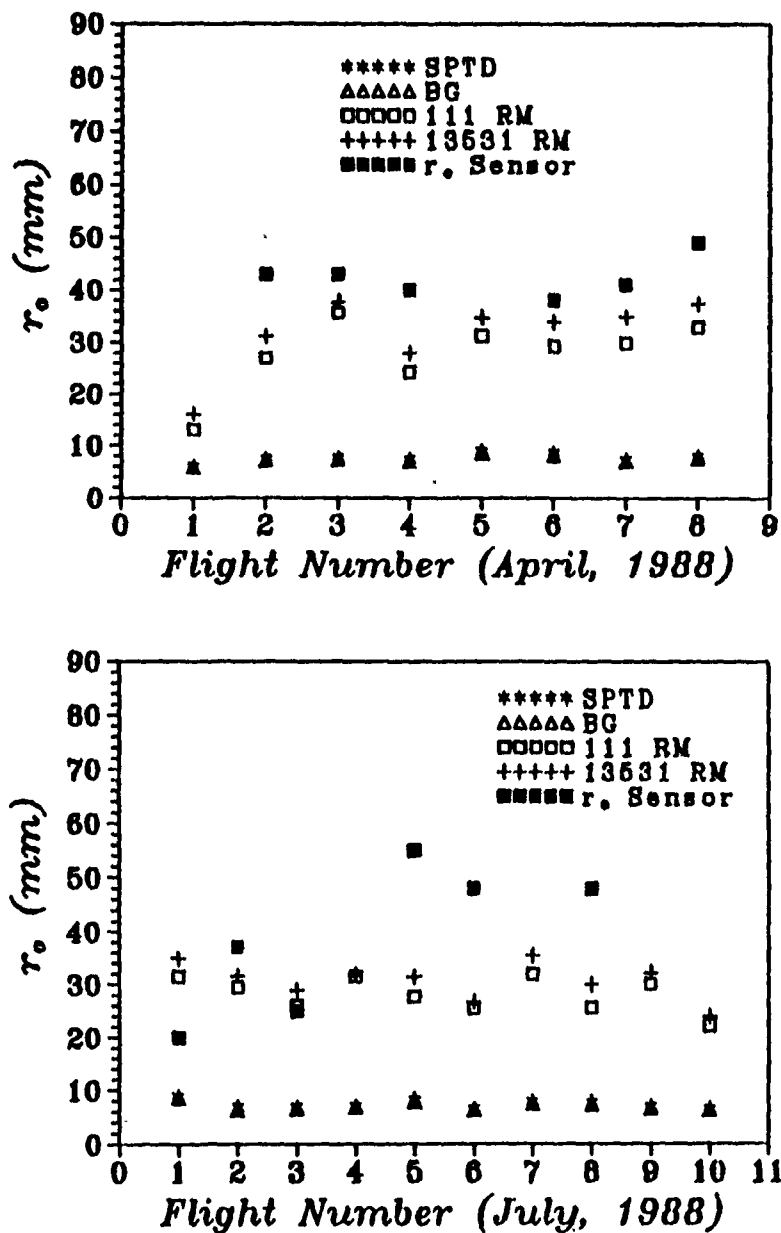


Fig. 9. Measured and Calculated r_o (All Values Included)

Transverse Coherence Length

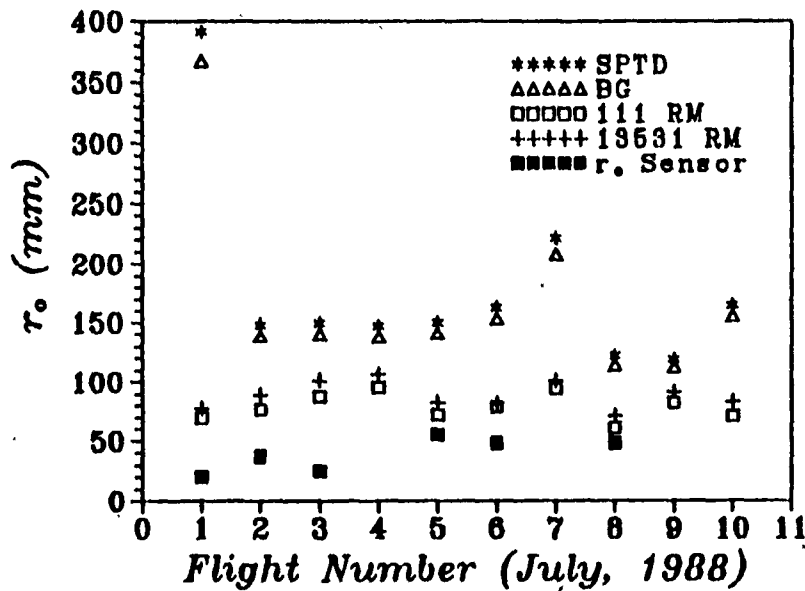
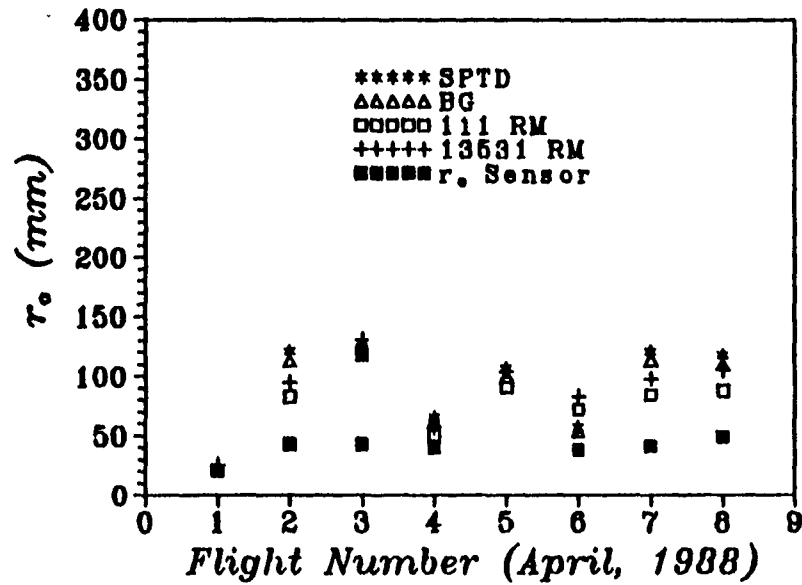


Fig. 10. Measured and Calculated r_0 ($Ri < 0.25$)

Transverse Coherence Length

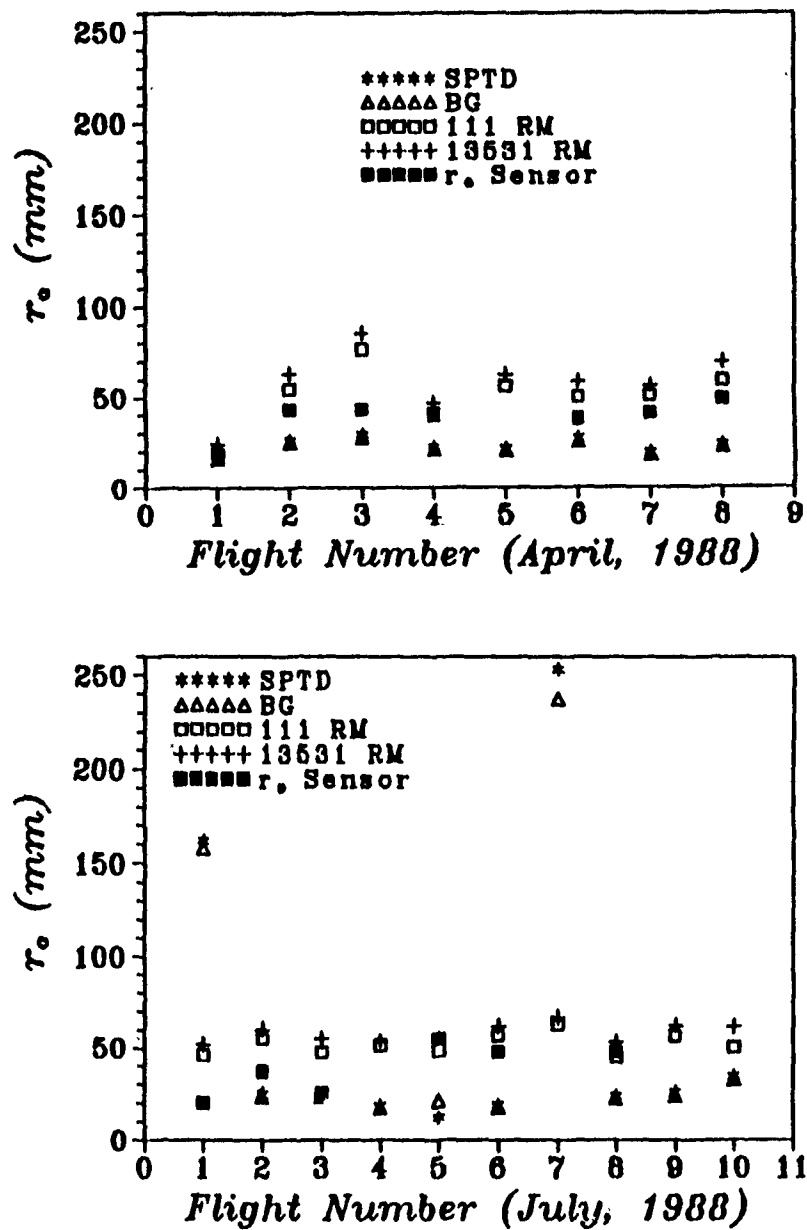


Fig. 11. Measured and Calculated r_0 ($Ri < 2.0$)

B. θ_0 RESULTS

Figure 12 through Figure 14 display the θ_0 values calculated from the eight April 1988 and ten July 1988 Maui rawinsonde datasets. An estimate of the θ_0 simultaneously measured over the same Kihei, Maui site is also included.

For the measured θ_0 time series corresponding to these profiles, see Nelson (1988).

Isoplanatic Angle

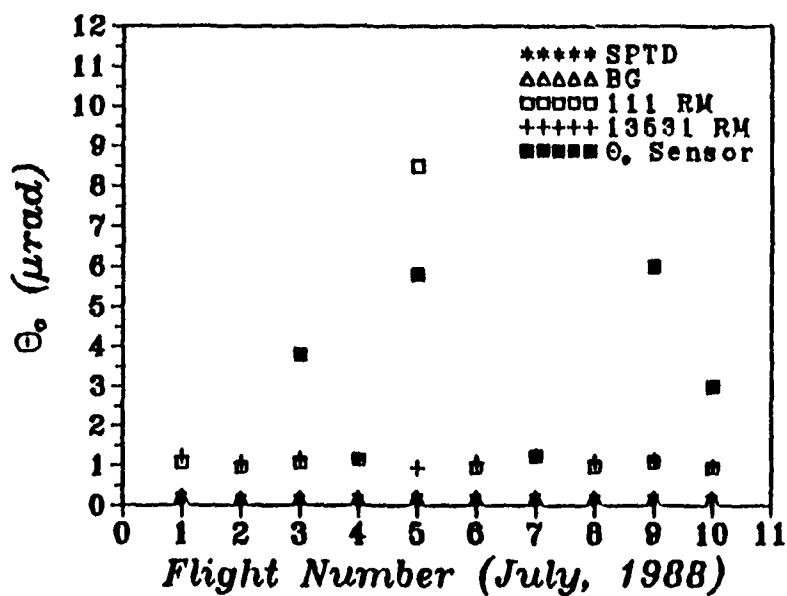
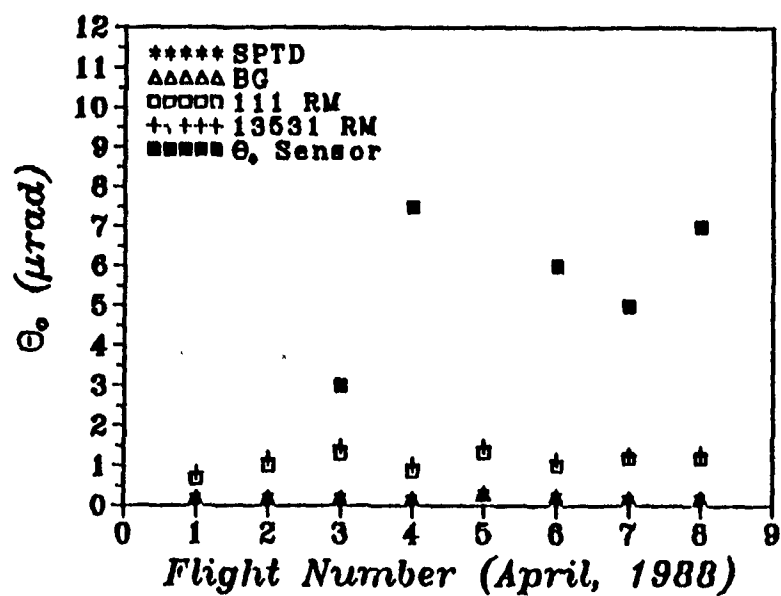


Fig. 12. Measured and Calculated Θ_0 (All Values Included)

Isoplanatic Angle

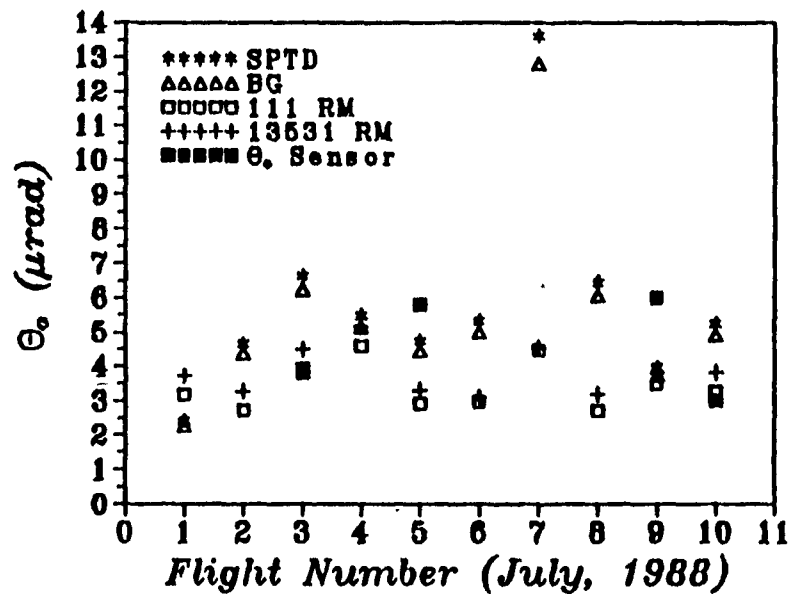
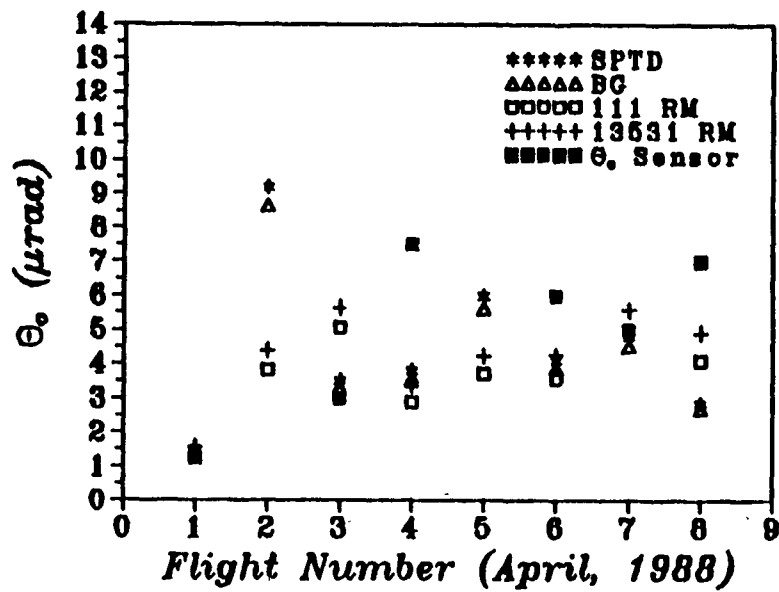


Fig. 13. Measured and Calculated θ_0 ($Ri < 0.25$)

Isoplanatic Angle

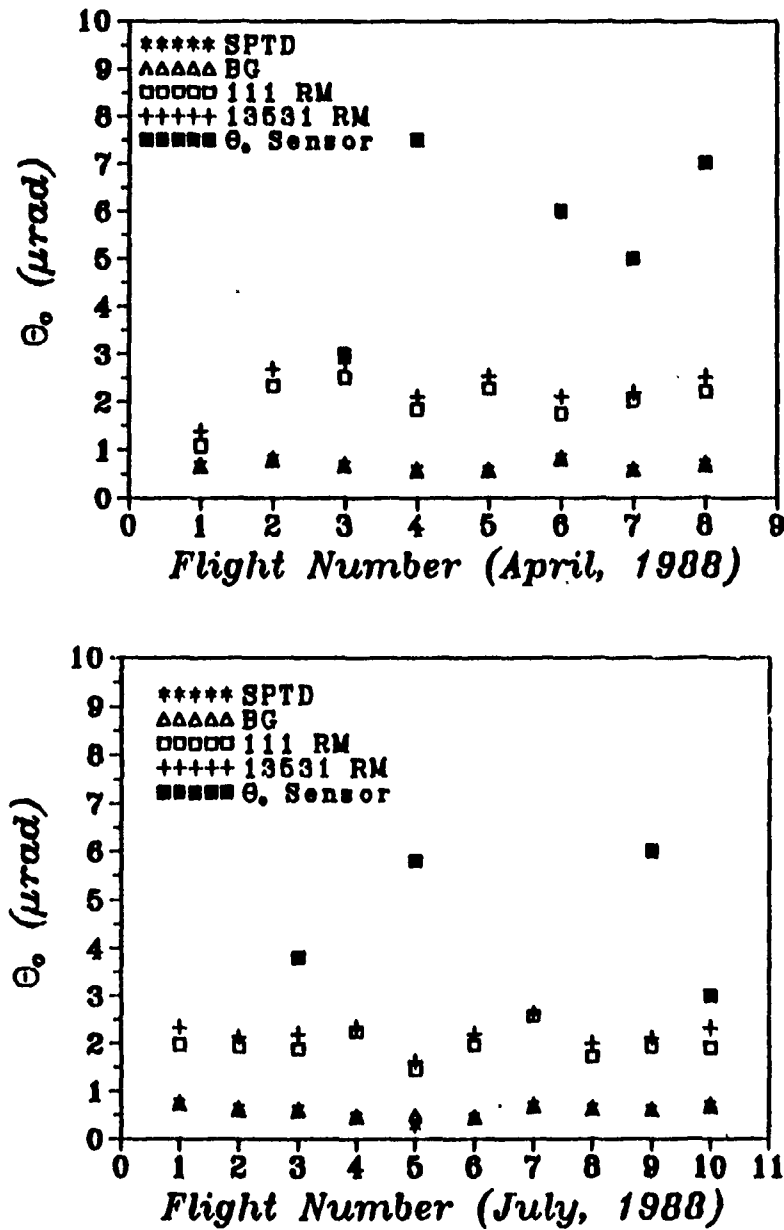


Fig. 14. Measured and Calculated Θ_0 ($Ri < 2.0$)

APPENDIX B. MAUI, HAWAII - AUGUST 1987

A. METEOROLOGICAL DATA

Appendix B includes the August 1987 vertical profiles of atmospheric data acquired during the Relay Mirror Experiment at Kihei, Maui. The data acquisition system used was a VIZ WO-8000 RP+ rawinsonde system. Vertical resolution is approximately 35 m. Launch site was at 20.45° latitude, 156.27° longitude. Table 8 couples the rawinsonde flight numbers and launch times for all the August 1987 Kihei soundings.

Table 8. AUGUST 1987 KIHAI, MAUI RAWINSONDE LAUNCHES

FLIGHT NO.	TIME (UTC)	DATE (DAY MON YR)
1	0658	18 August 1987
2	1440	18 August 1987
3	0722	19 August 1987
4	1103	19 August 1987
5	1512	19 August 1987
6	0607	20 August 1987
7	1011	20 August 1987
8	0650	21 August 1987
9	1106	21 August 1987
10	1559	21 August 1987
11	0541	22 August 1987
12	1053	22 August 1987

August 87 - Flight 1

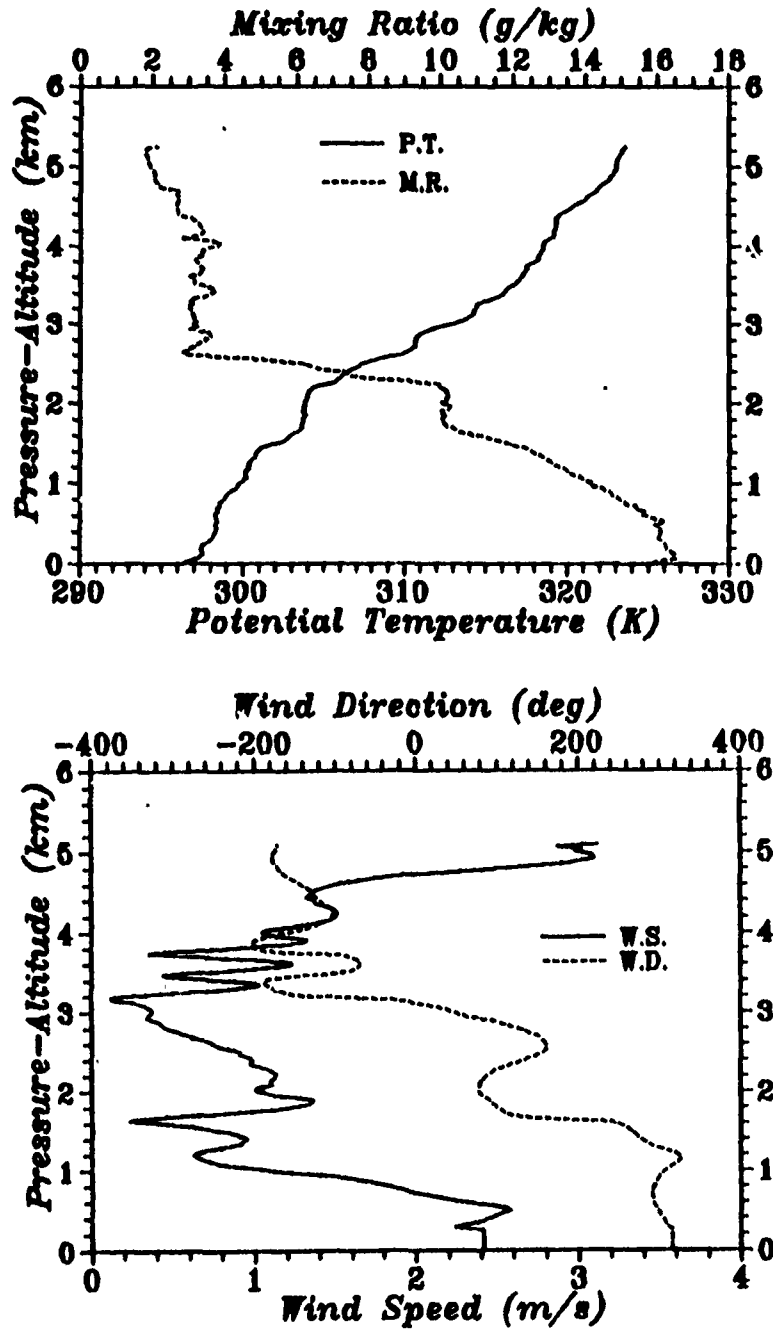


Fig. 15. Kihei, Maui Rawinsonde Data: 0658 UTC 18 August 1987

August 87 - Flight 2

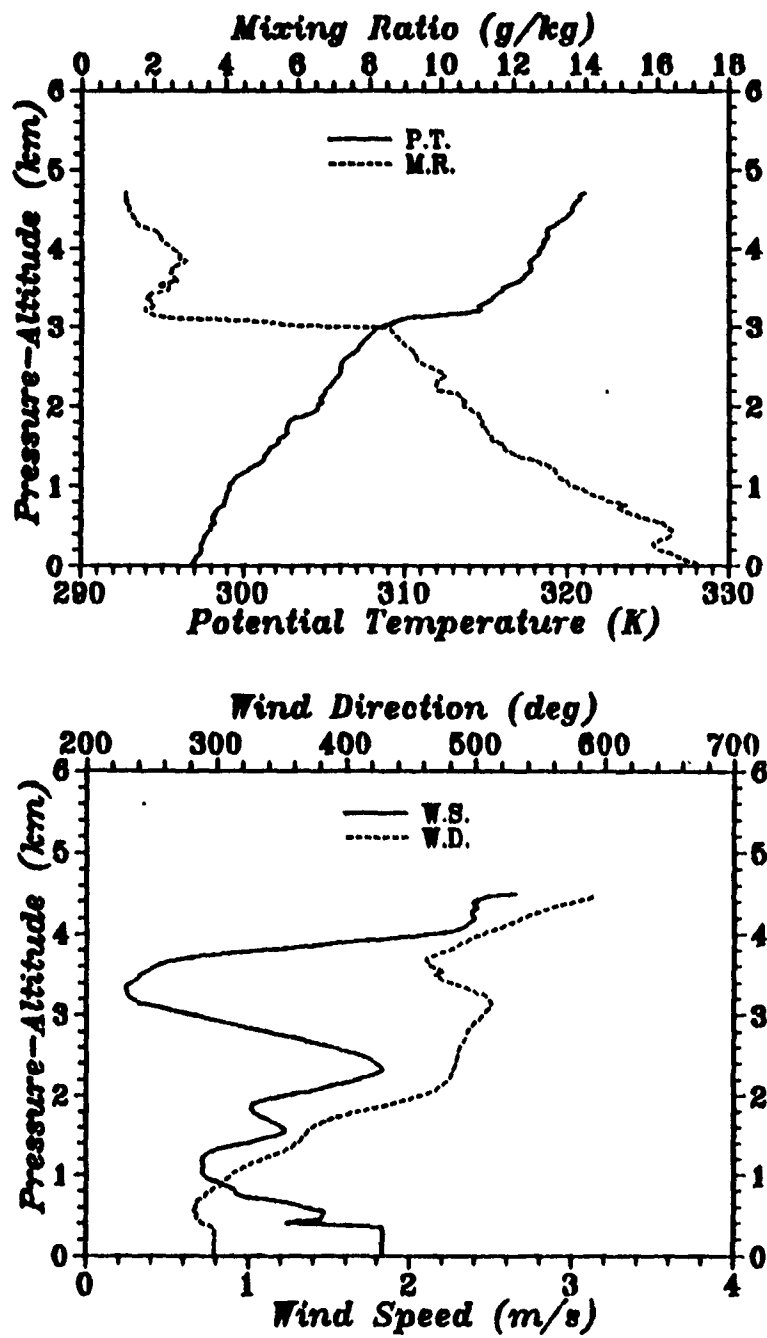


Fig. 16. Kihei, Maui Rawinsonde Data: 1440 UTC 18 August 1987

August 87 - Flight 3

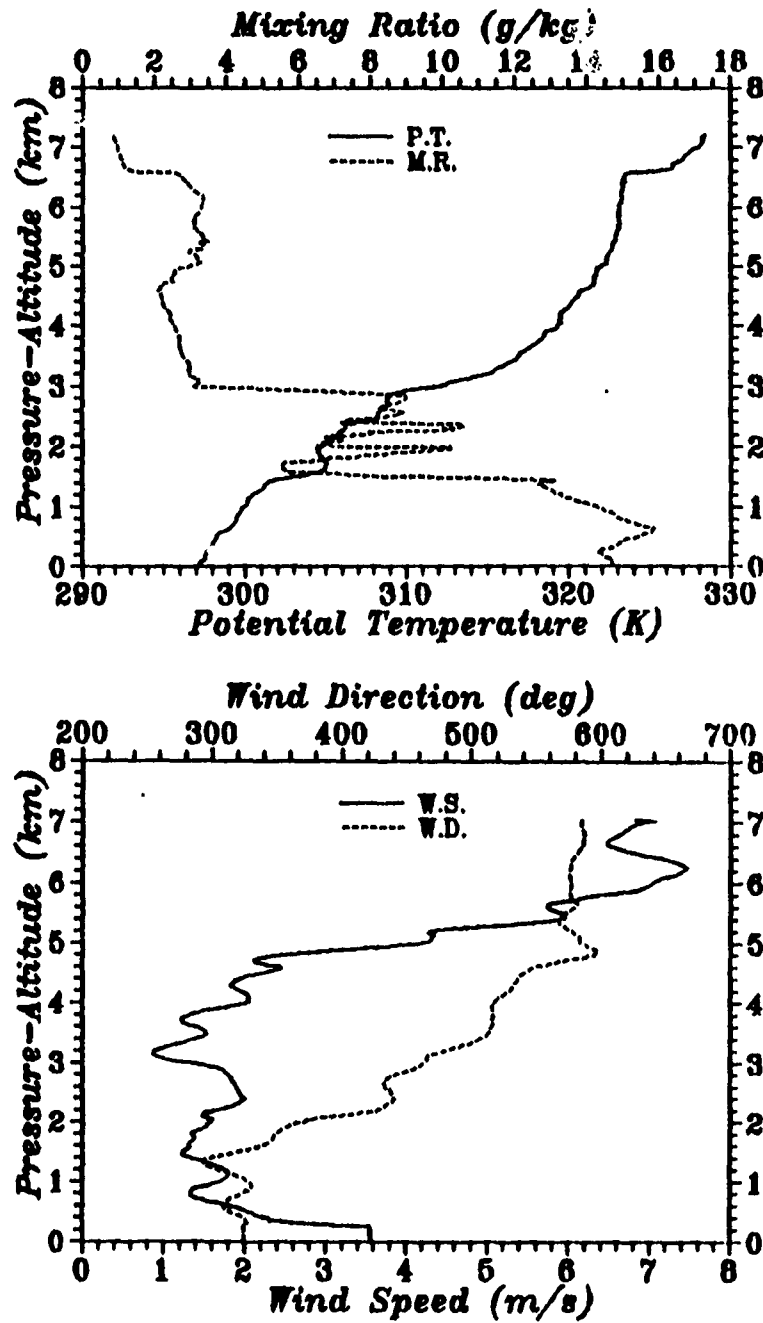


Fig. 17. Kihei, Maui Rawinsonde Data: 0722 UTC 19 August 1987

August 87 - Flight 4

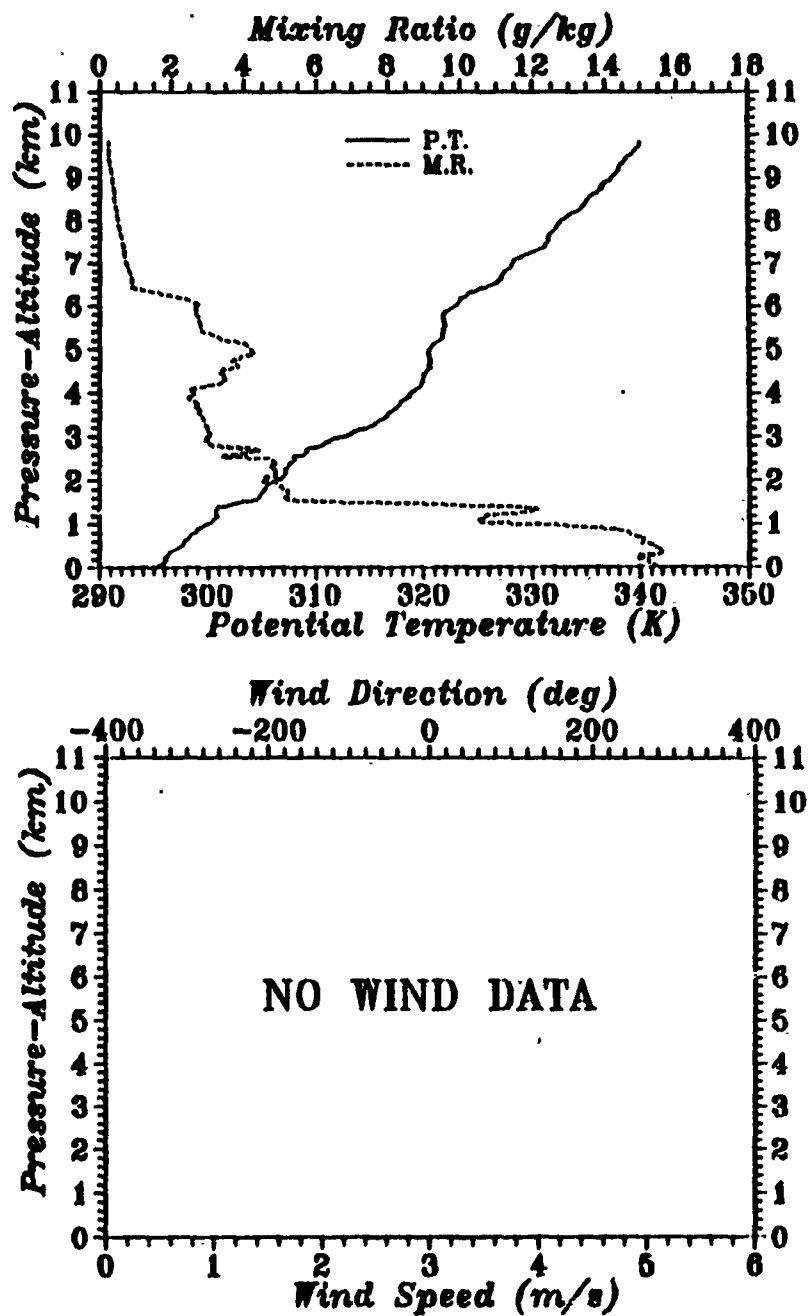


Fig. 18. Kihei, Maui Rawinsonde Data: 1103 UTC 19 August 1987

August 87 - Flight 5

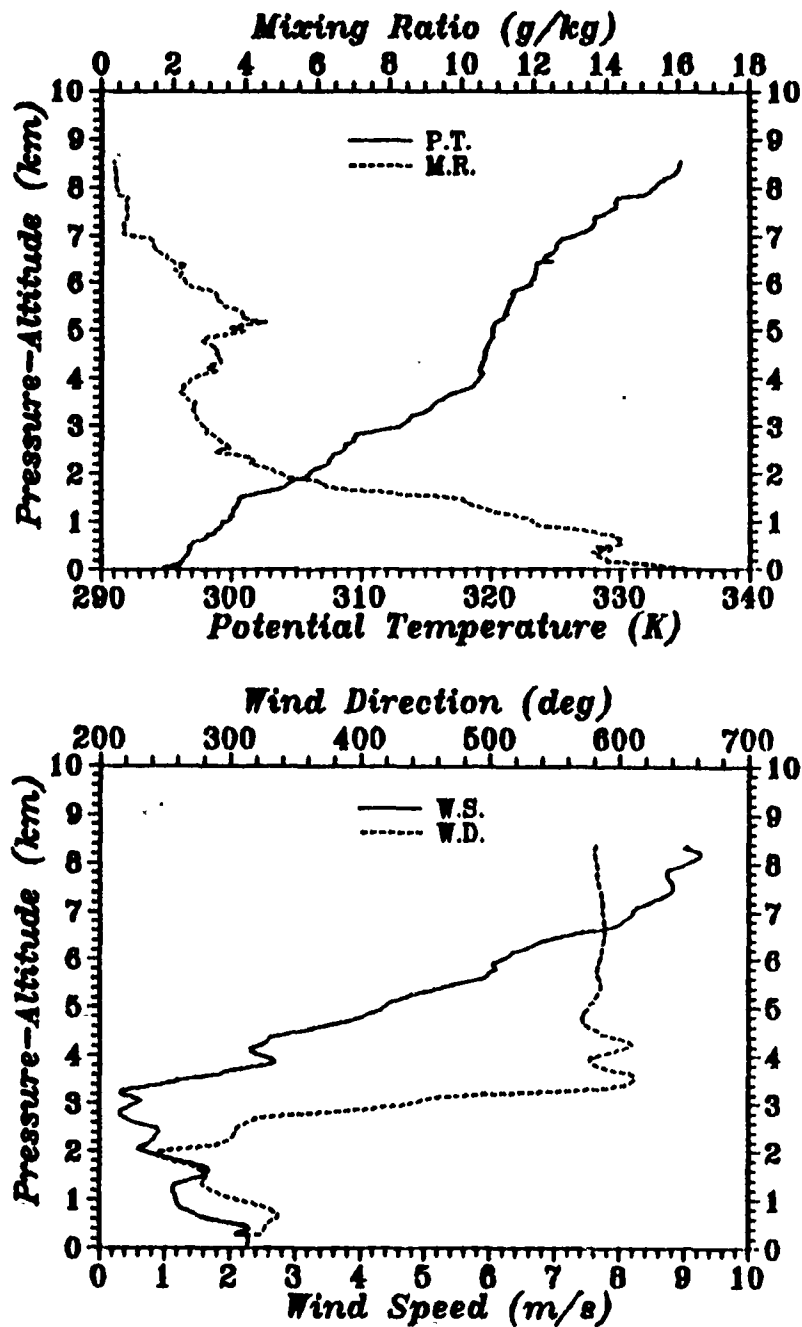


Fig. 19. Kihei, Maui Rawinsonde Data: 1512 UTC 19 August 1987

August 87 - Flight 6

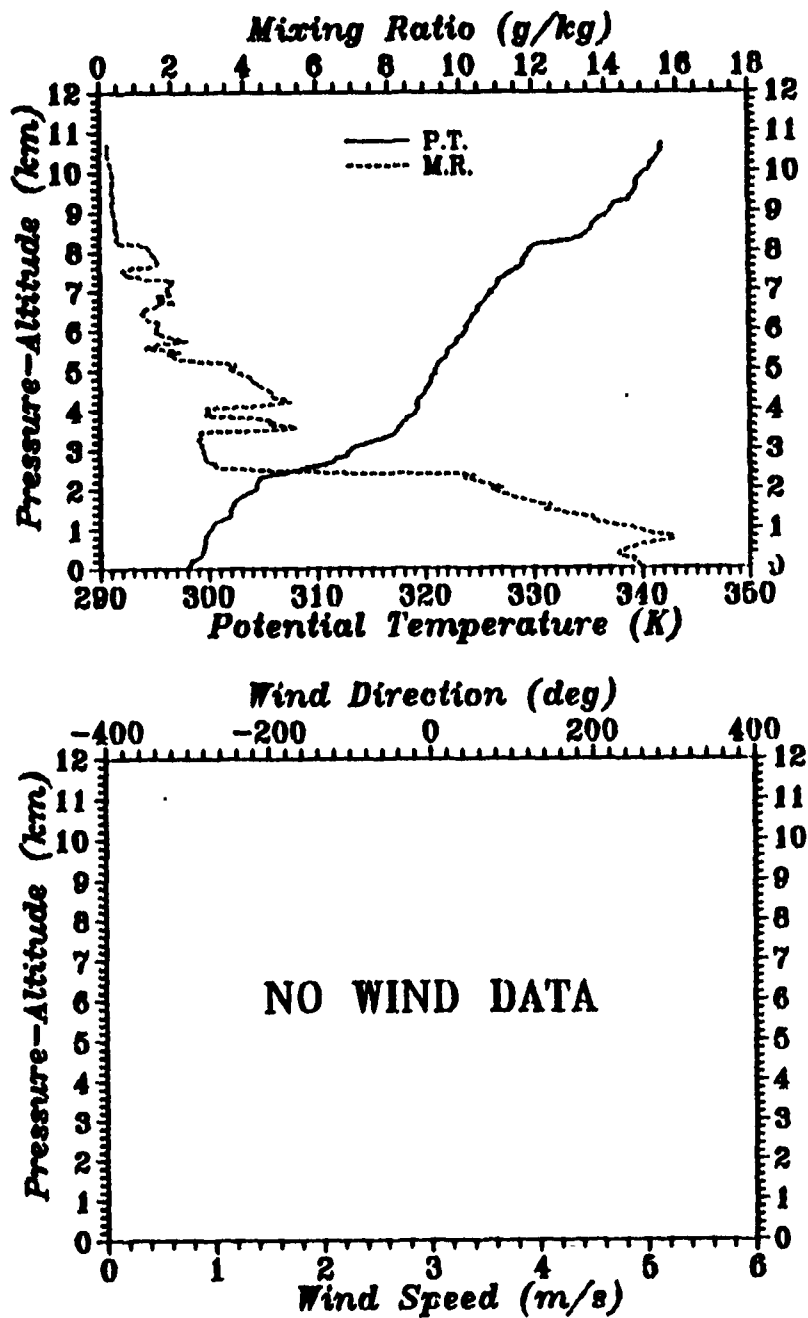


Fig. 20. Kihei, Maui Rawinsonde Data: 0607 UTC 20 August 1987

August 87 - Flight 7

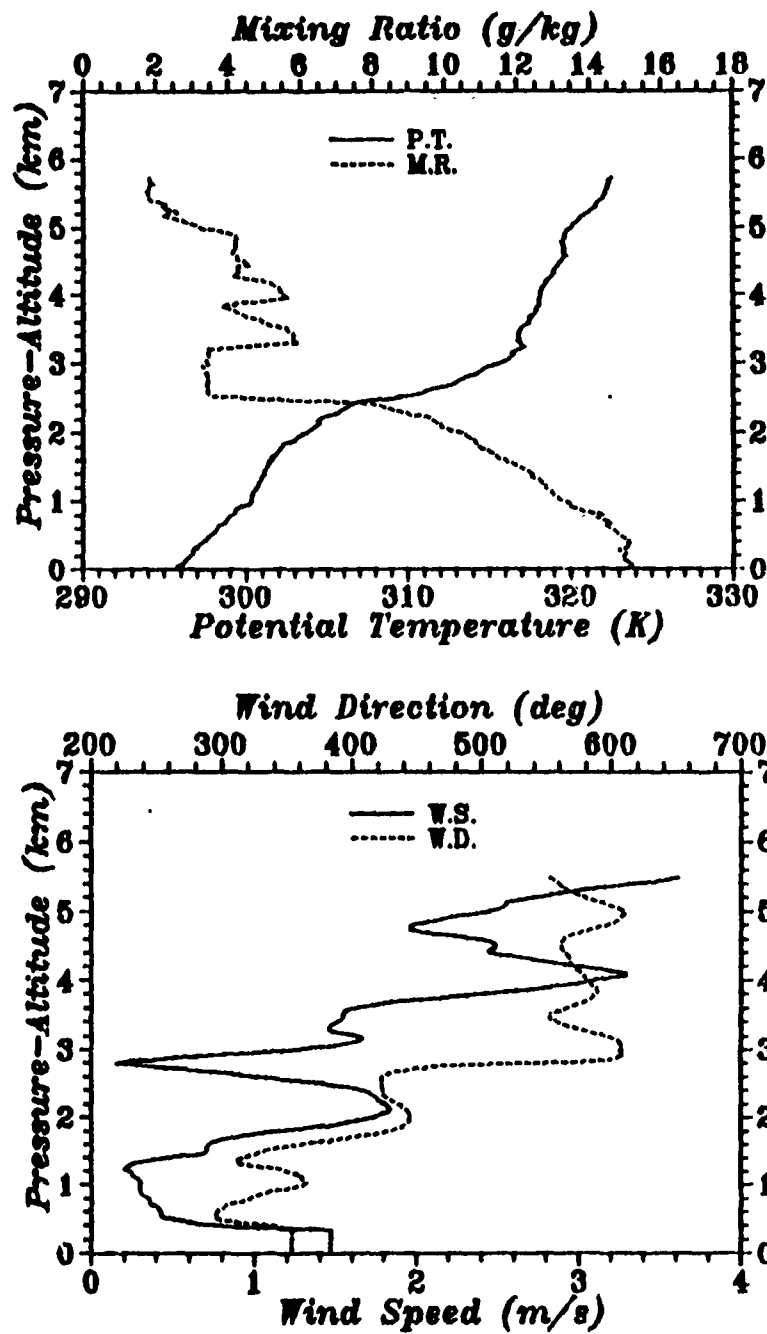


Fig. 21. Kihei, Maui Rawinsonde Data: 1011 UTC 20 August 1987

August 87 - Flight 8

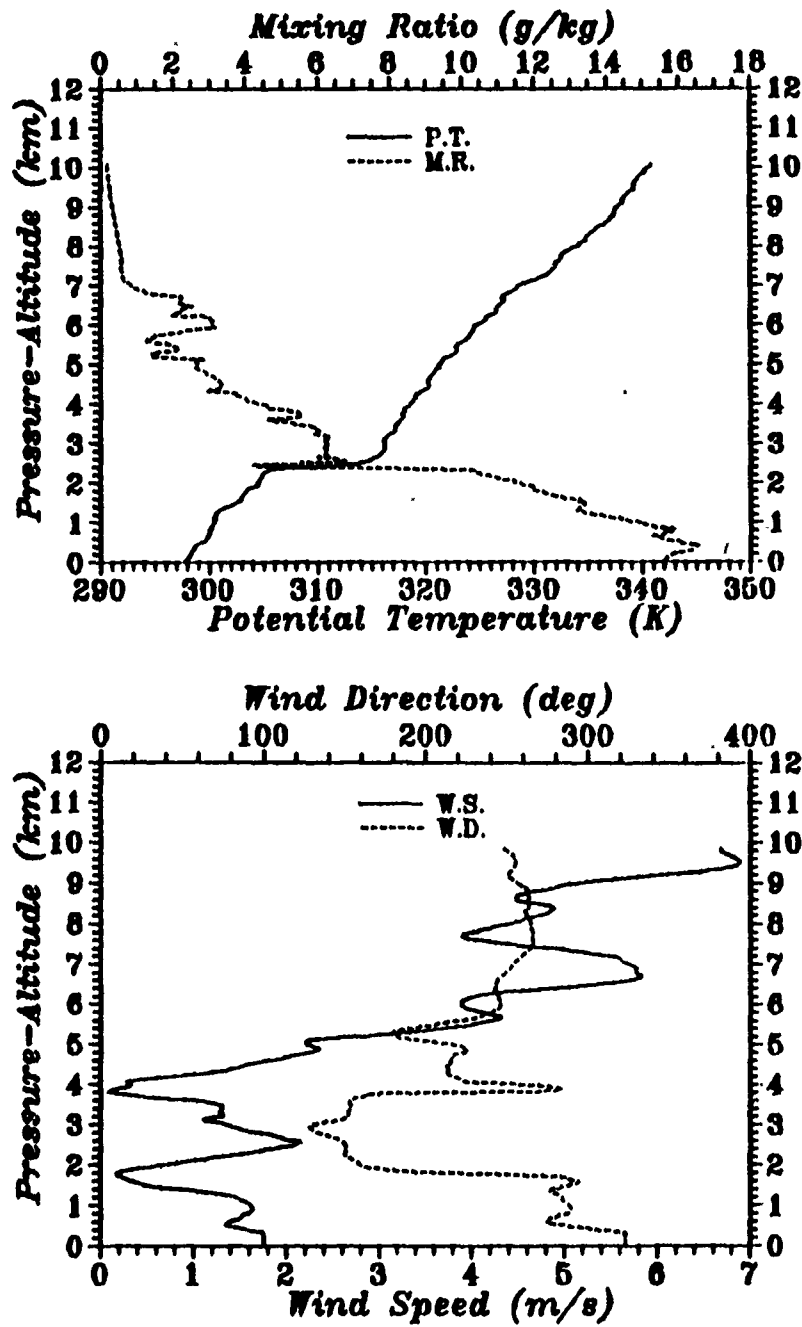


Fig. 22. Kihei, Maui Rawinsonde Data: 0650 UTC 21 August 1987

August 87 - Flight 9

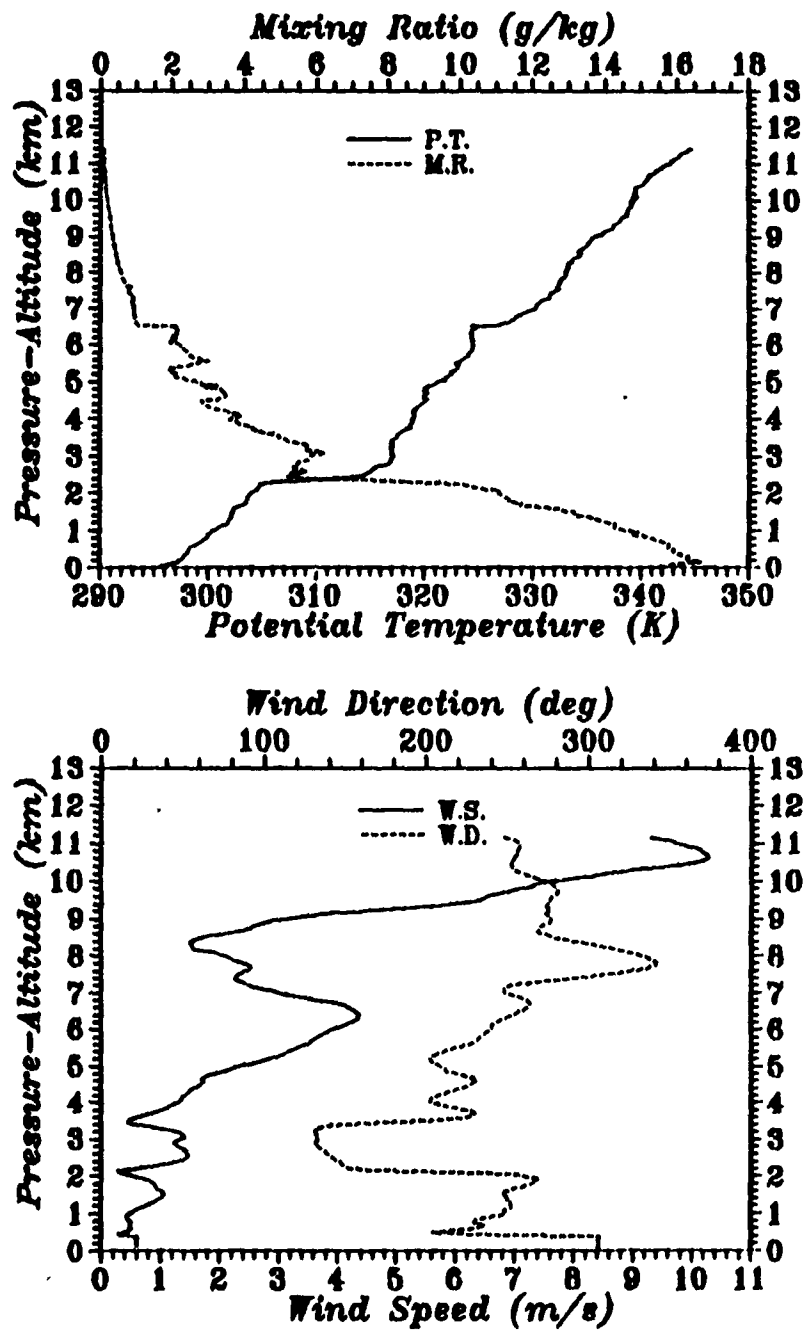


Fig. 23. Kihei, Maui Rawinsonde Data: 1106 UTC 21 August 1987

August 87 - Flight 10

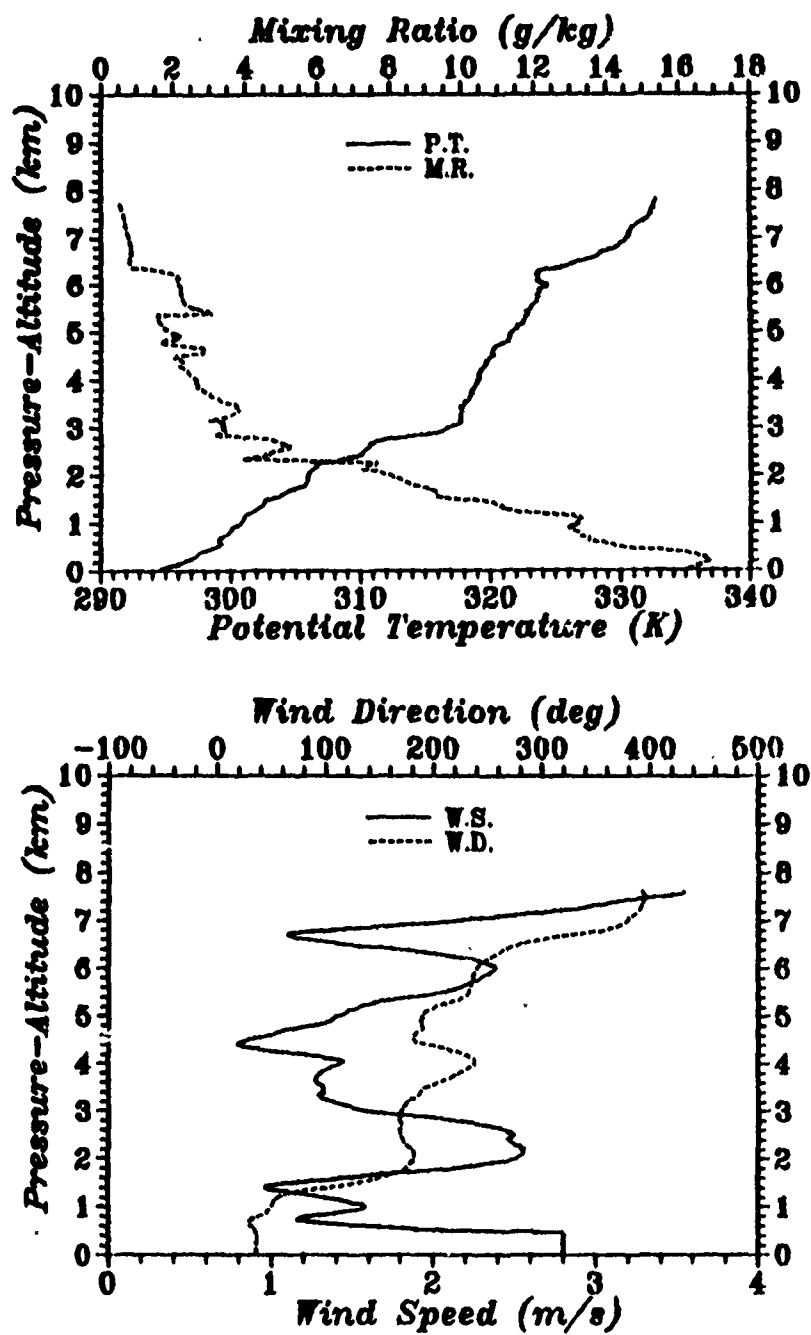


Fig. 24. Kihei, Maui Rawinsonde Data: 1559 UTC 21 August 1987

August 87 - Flight 11

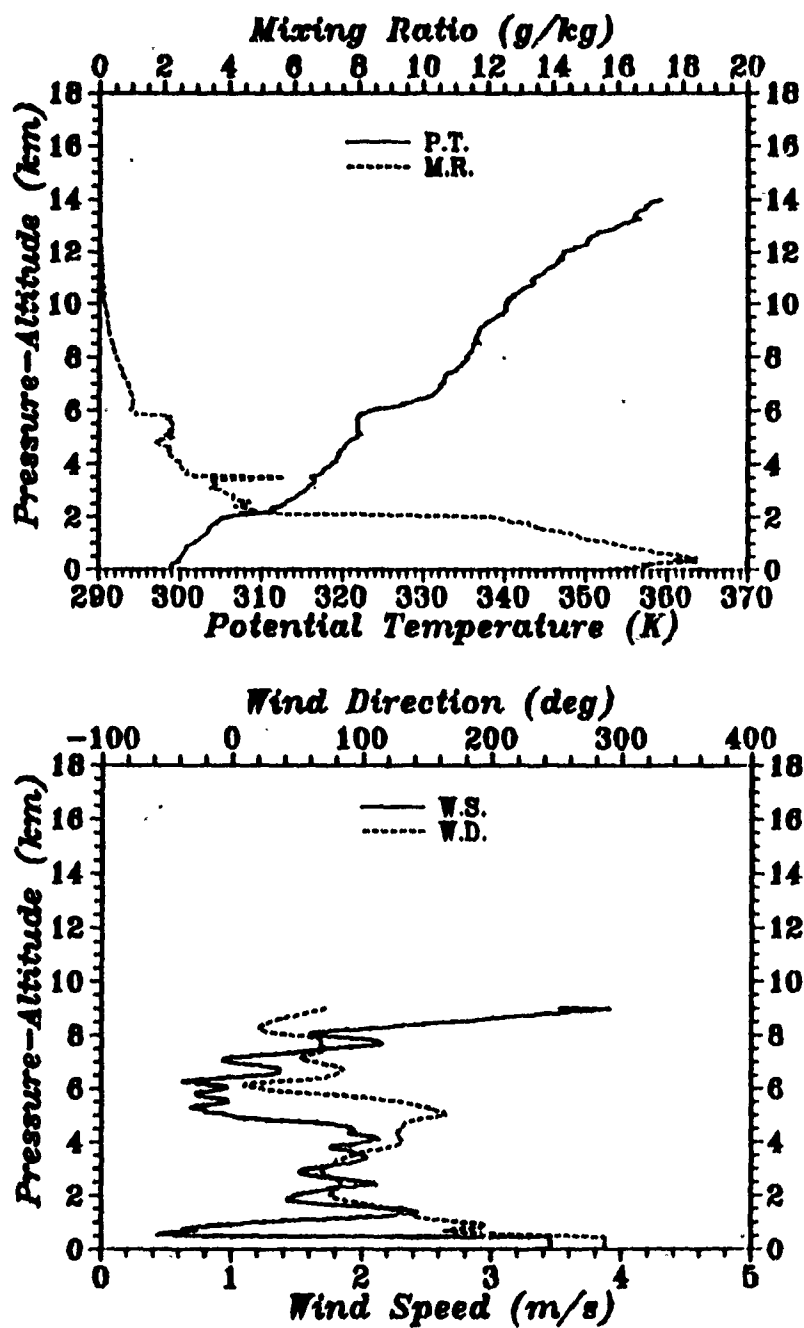


Fig. 25. Kihui, Maui Rawinsonde Data: 0541 UTC 22 August 1987

August 87 - Flight 12

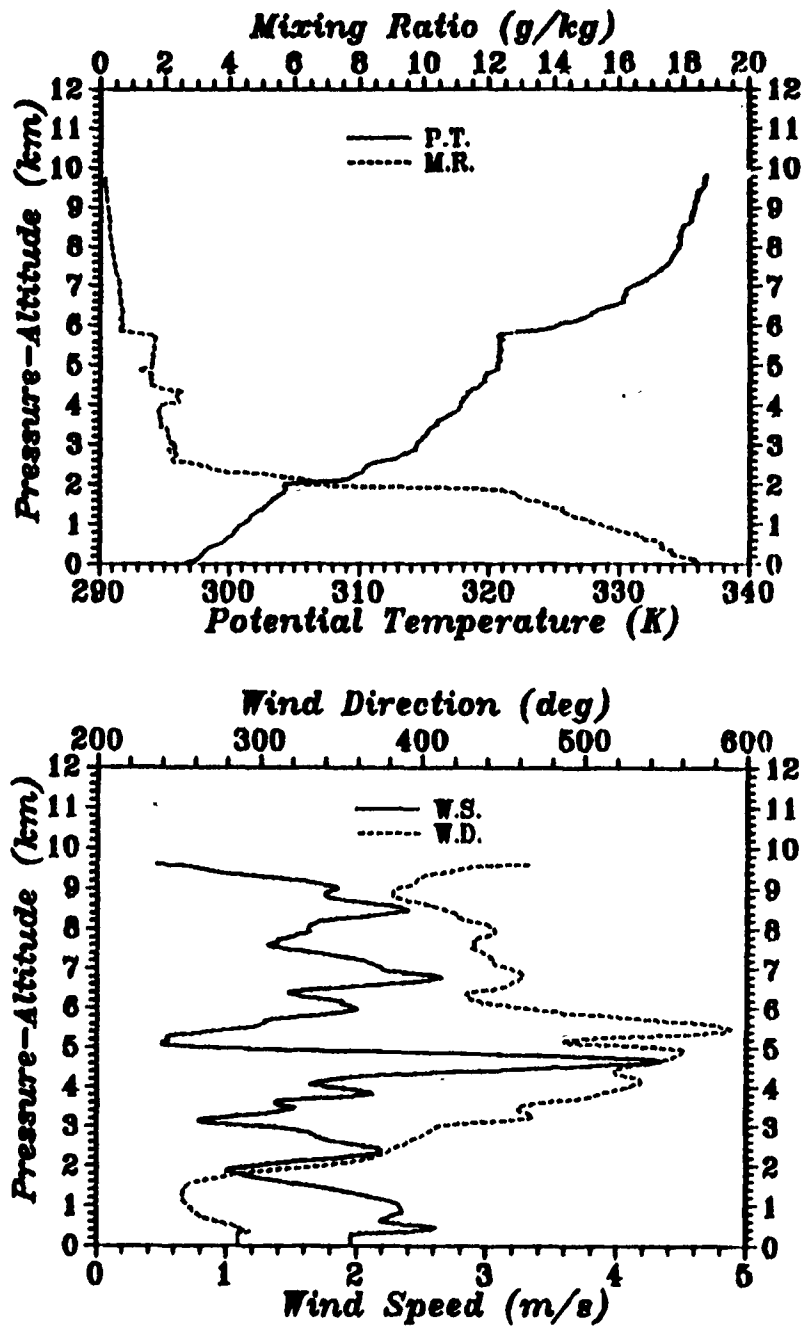


Fig. 26. Kihei, Maui Rawinsonde Data: 1053 UTC 22 August 1987

APPENDIX C. MAUI, HAWAII - DECEMBER 1987

A. METEOROLOGICAL DATA

Appendix C includes vertical profiles from the December 1987 Kihei, Maui rawinsonde launches. The VIZ WO-8000 RP+ rawinsonde system used to acquire this data sampled values approximately every 35 m. Launch site for these profiles was at 20.54° latitude, 156.27° longitude. Table 9 tabulates all the flight numbers and launch times for the December 1987 Kihei soundings.

Table 9. DECEMBER 1987 KIHAI, MAUI RAWINSONDE LAUNCHES

FLIGHT NO.	TIME (UTC)	DATE (DAY MON YR)
1	0950	5 December 1987
2	1552	5 December 1987
3	0639	6 December 1987
4	1131	6 December 1987
5	0517	7 December 1987
6	No Data	--
7	1624	7 December 1987
8	0537	8 December 1987
9	1031	8 December 1987
10	1557	8 December 1987
11	0345	9 December 1987
12	0958	9 December 1987

December 87 - Flight 1

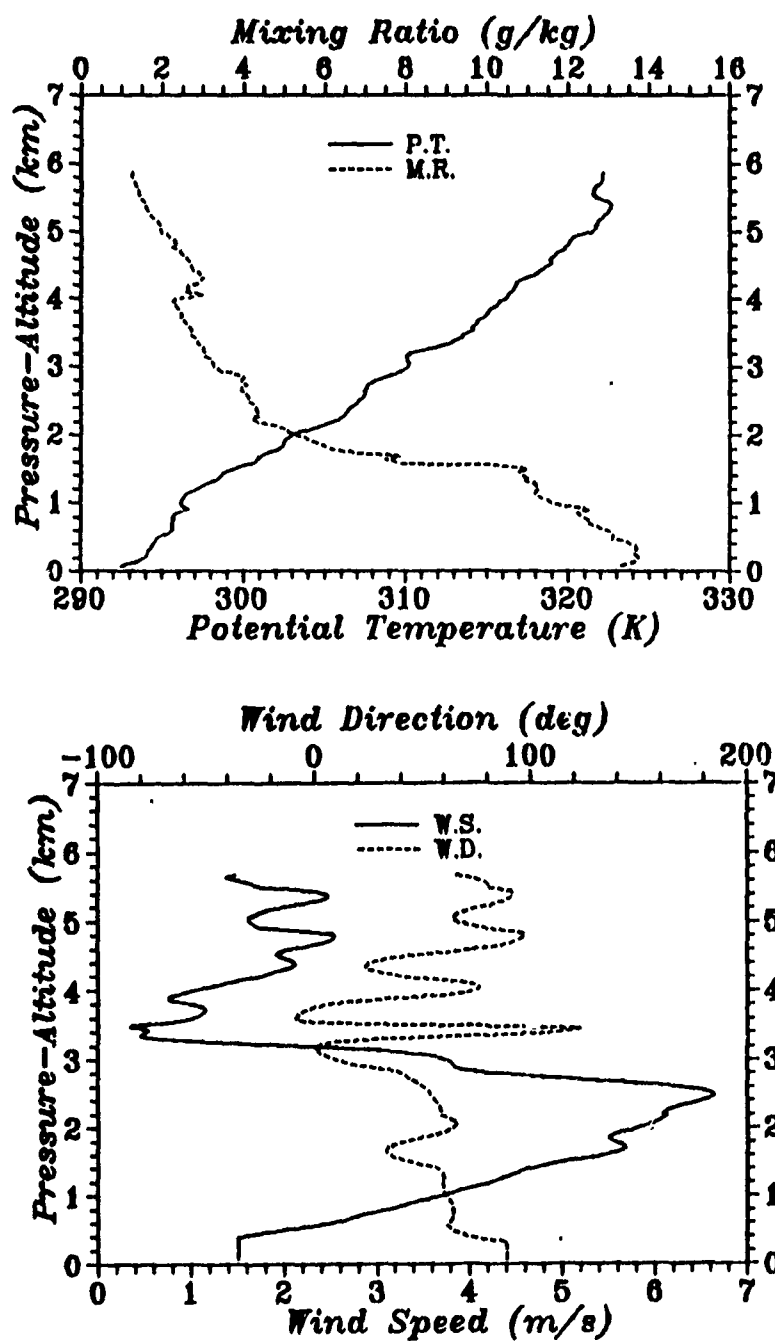


Fig. 27. Kīhei, Maui Rawinsonde Data: 0950 UTC 5 December 1987

December 87 - Flight 2

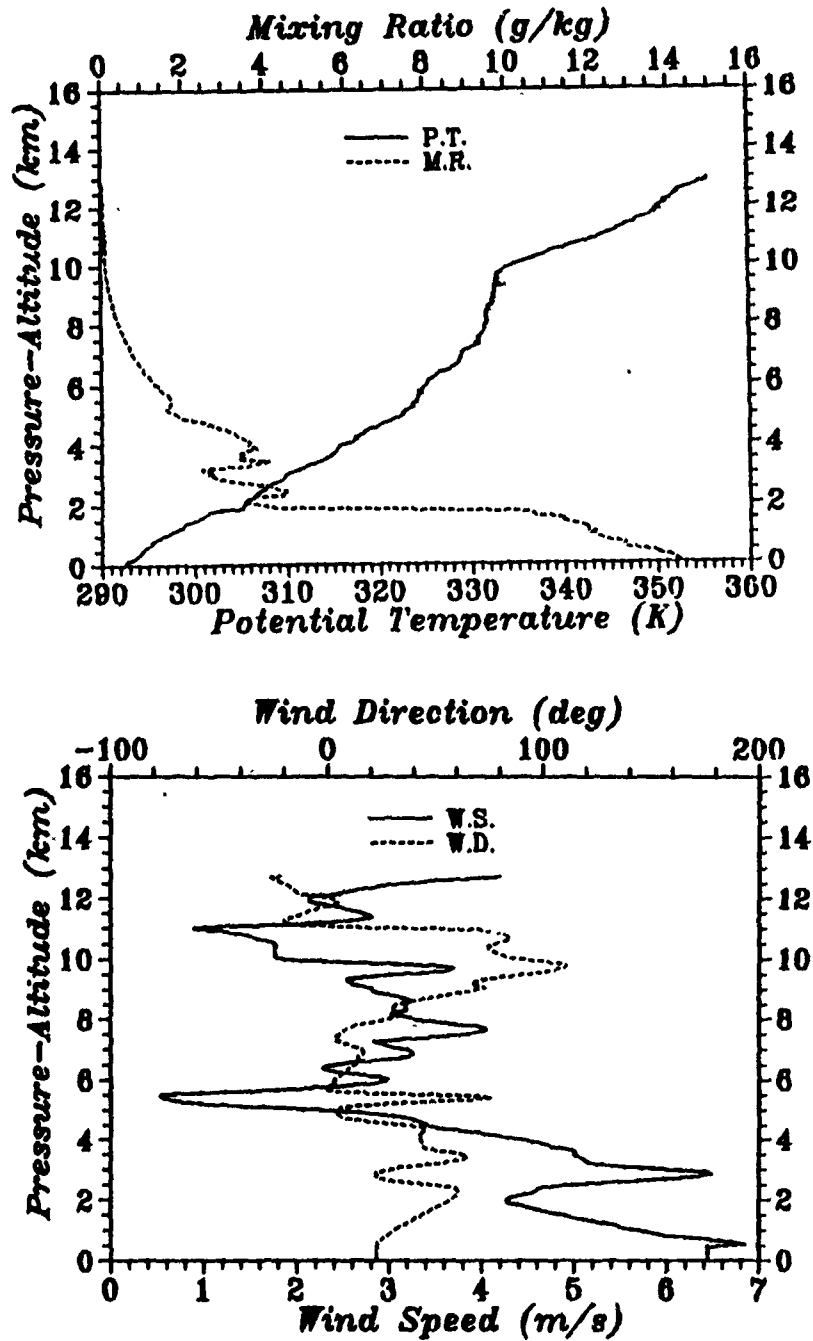


Fig. 28. Kilauea, Maui Rawinsonde Data: 1552 UTC 5 December 1987

December 87 - Flight 3

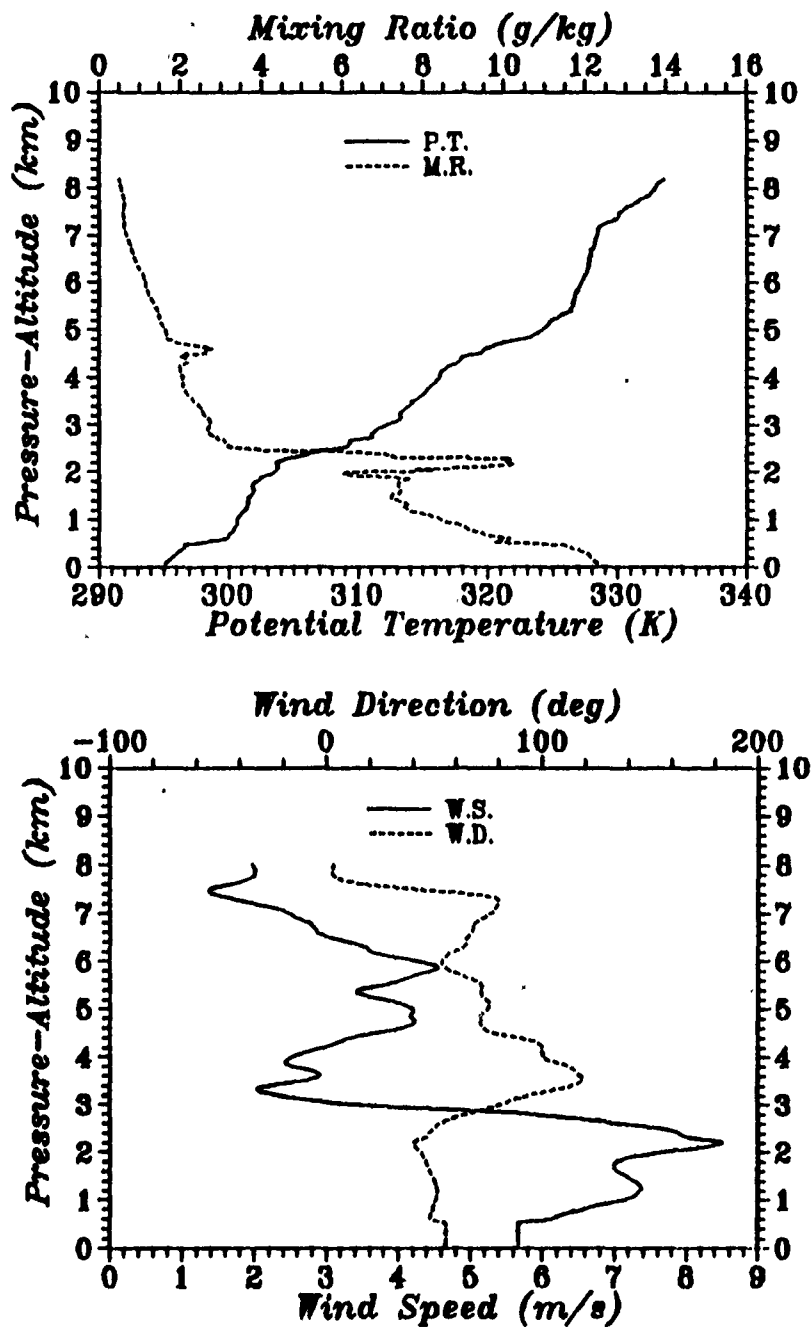


Fig. 29. Kilauea, Maui Rawinsonde Data: 0639 UTC 6 December 1987

December 87 - Flight 4

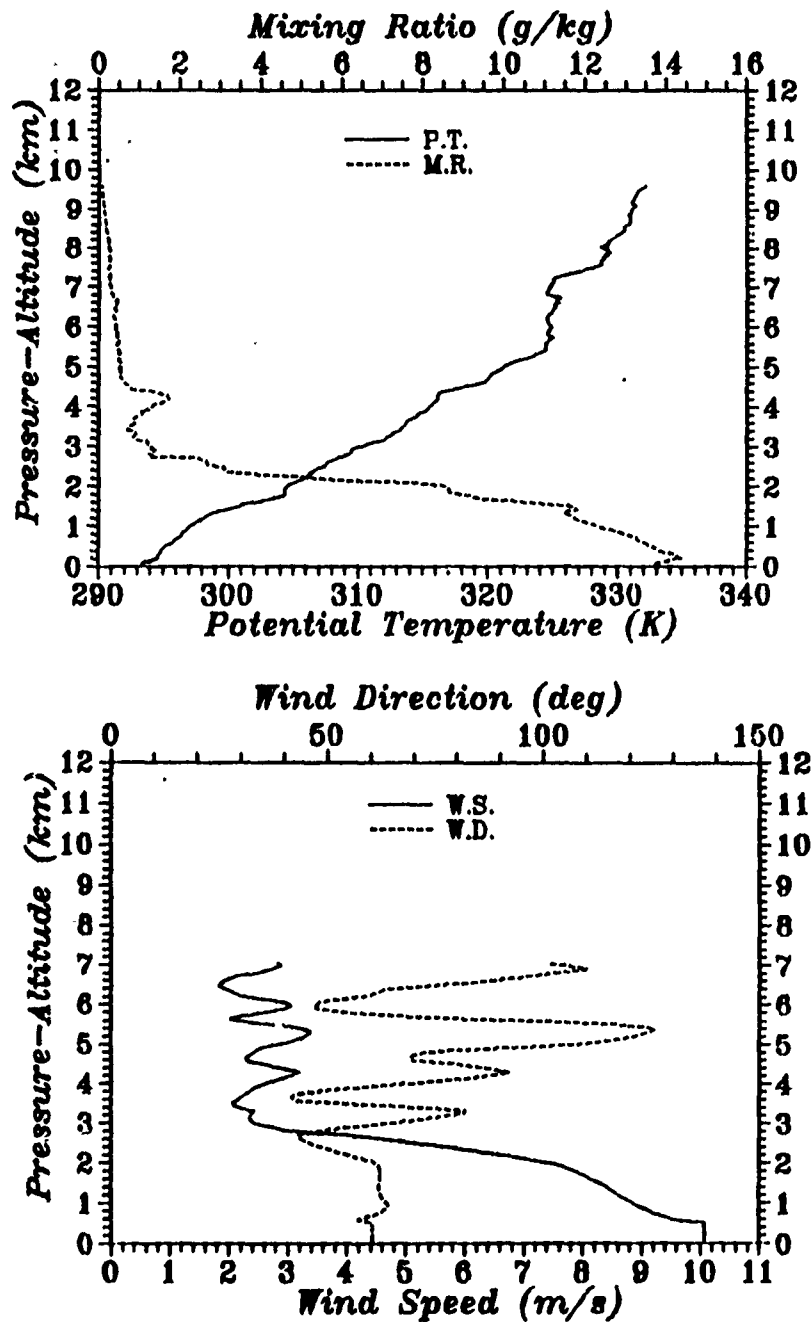


Fig. 30. Kilauea, Maui Rawinsonde Data: 1131 UTC 6 December 1987

December 87 - Flight 5

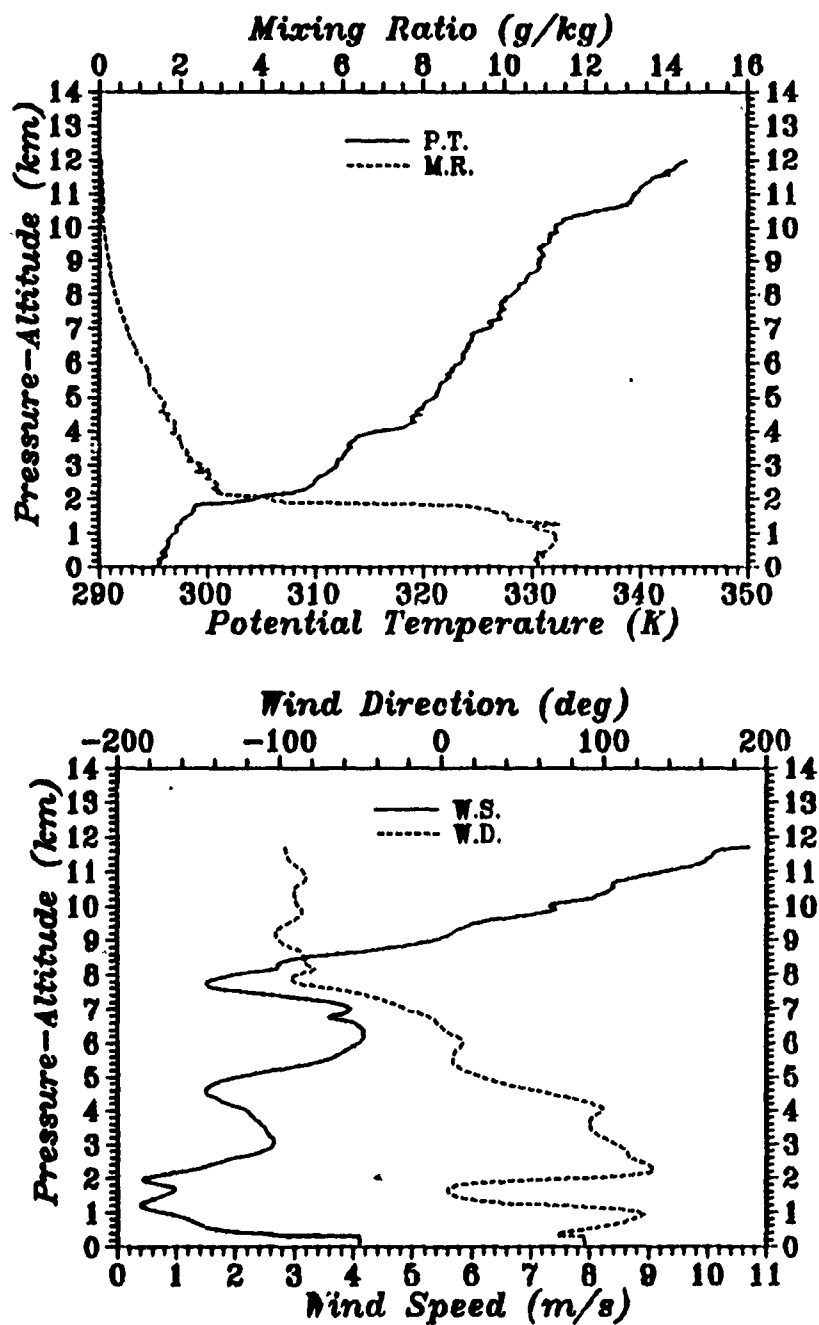


Fig. 31. Kihei, Maui Rawinsonde Data: 0517 UTC 7 December 1987

December 87 - Flight 7

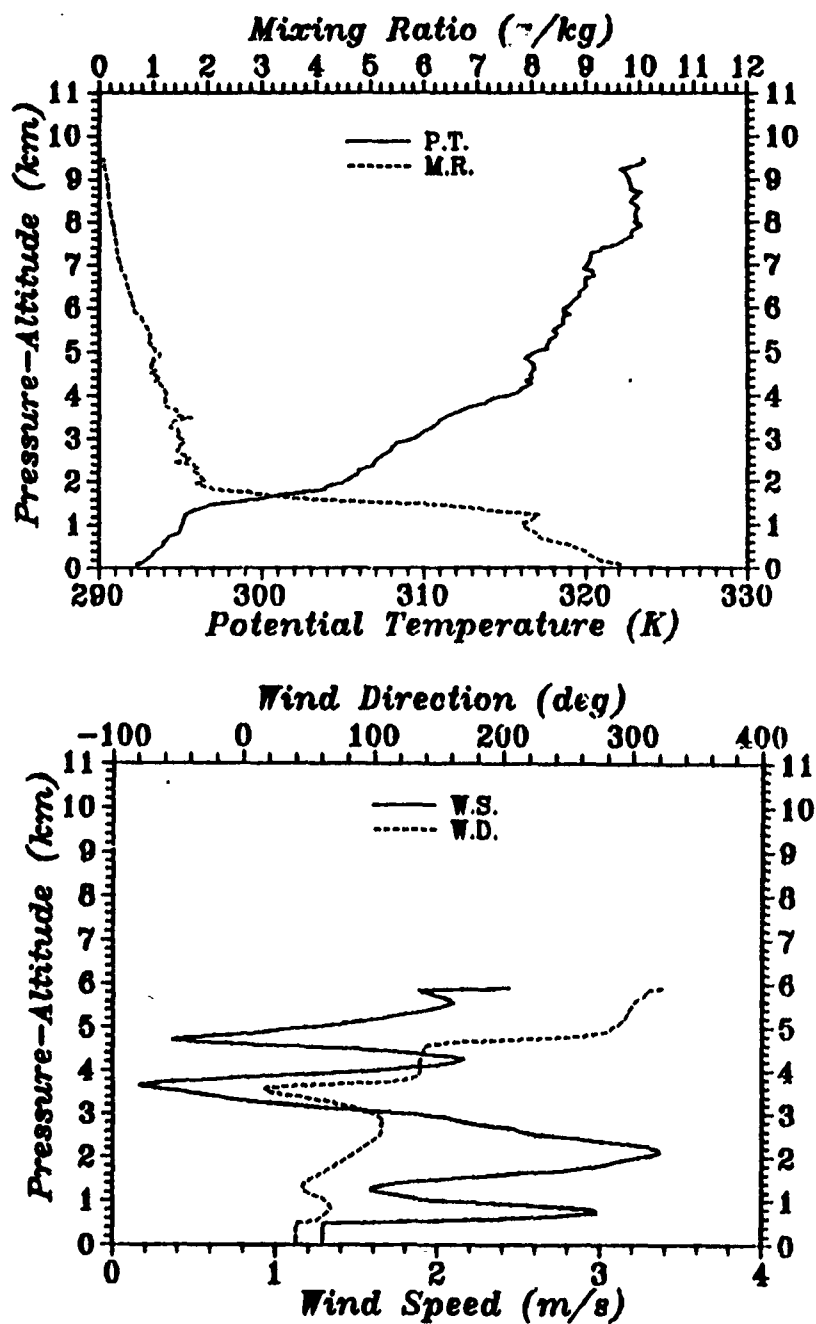


Fig. 32. Kihei, Maui Rawinsonde Data: 1624 UTC 7 December 1987

December 87 - Flight 8

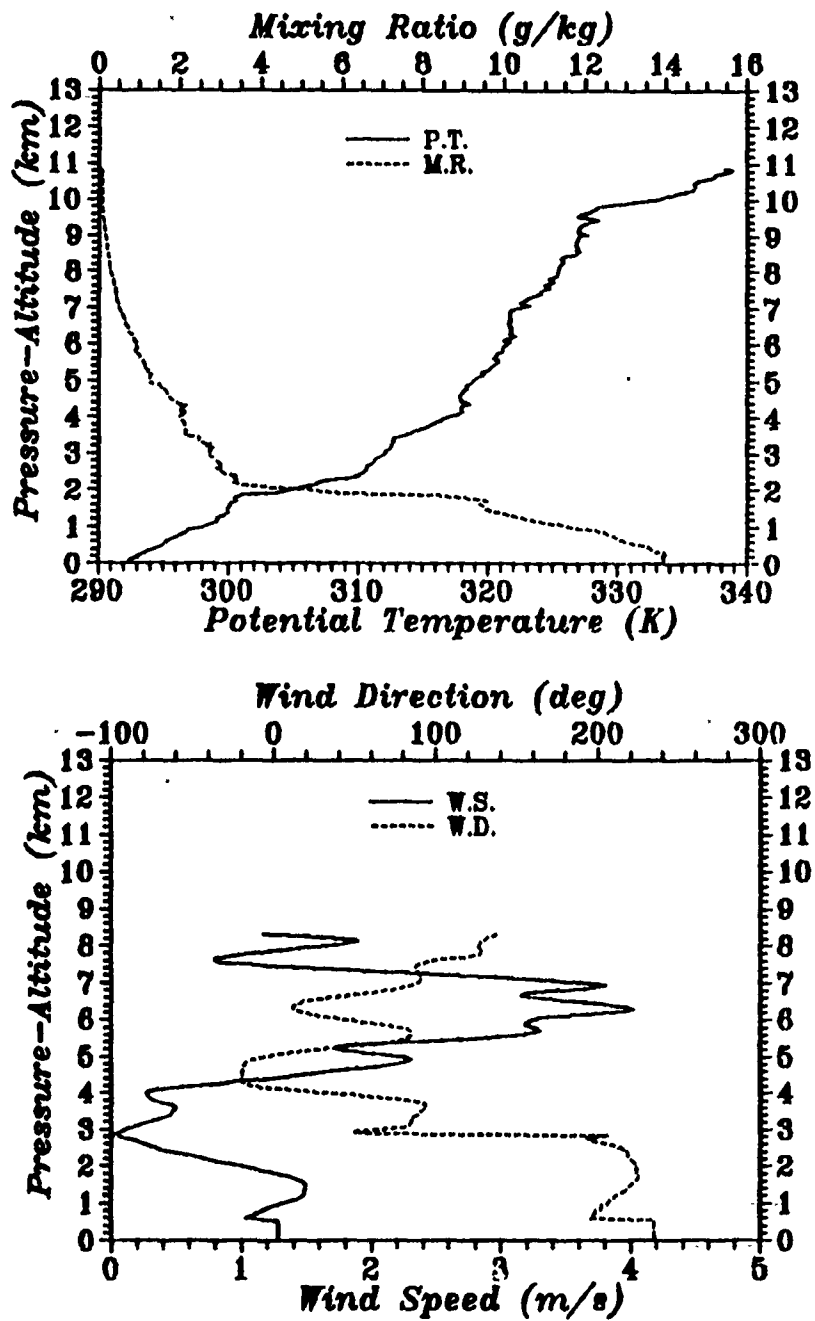


Fig. 33. Kihei, Maui Rawinsonde Data: 0537 UTC 8 December 1987

December 87 - Flight 9

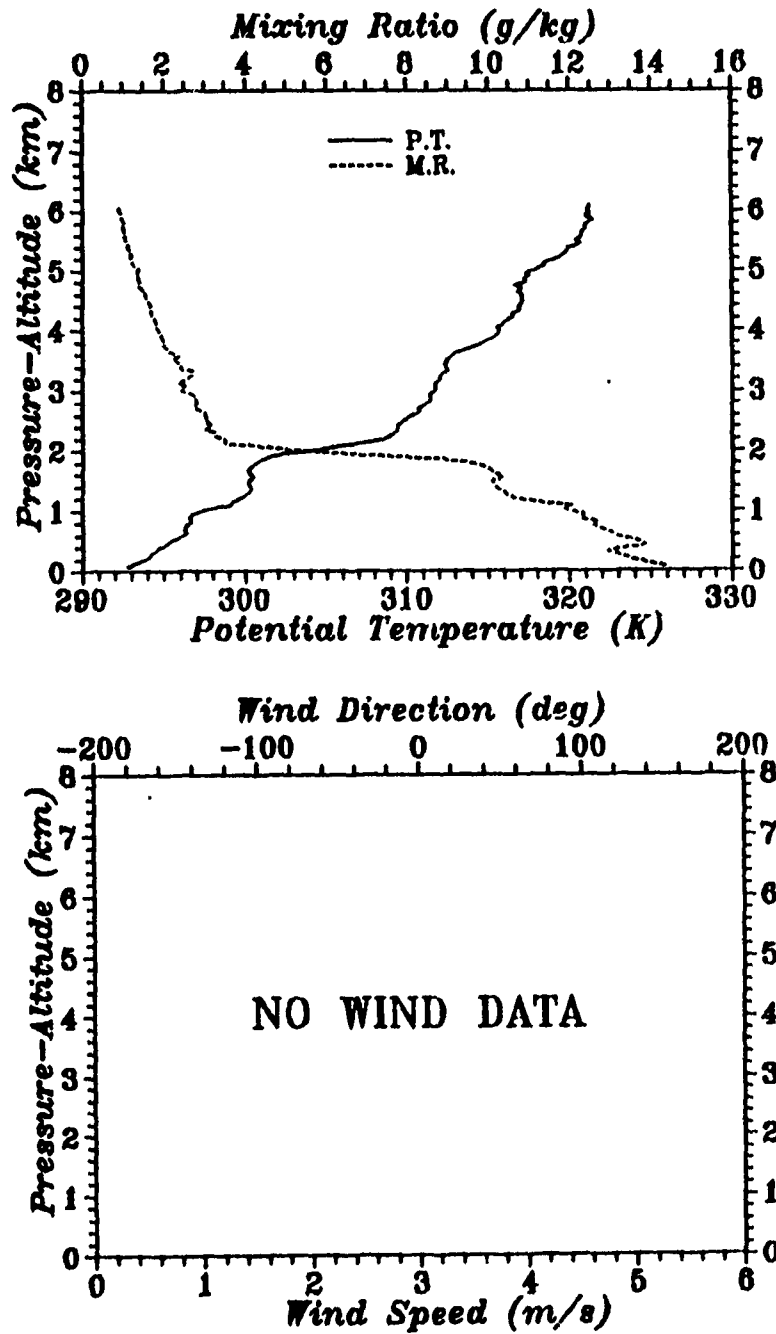


Fig. 34. Kilauea, Maui Rawinsonde Data: 1031 UTC 8 December 1987

December 87 - Flight 10

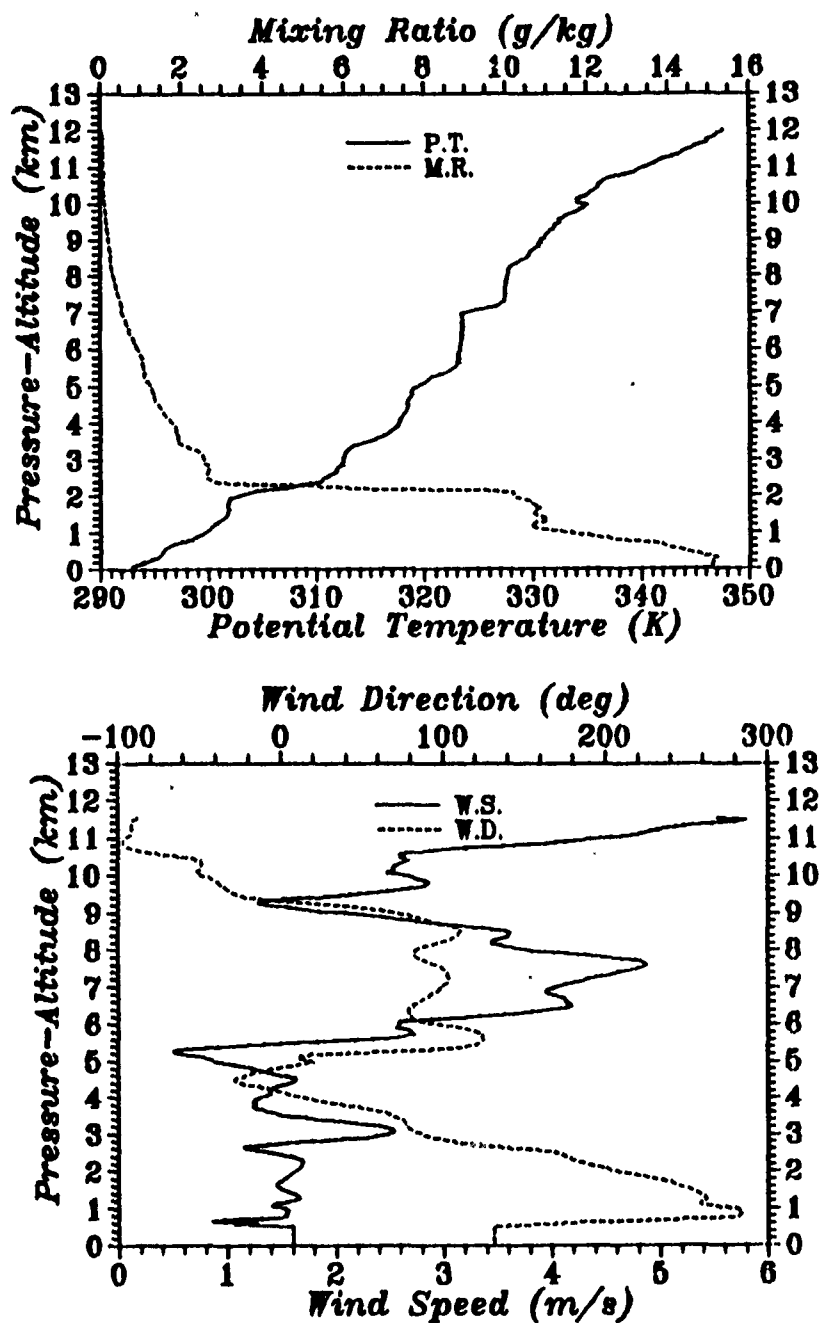


Fig. 35. Kihei, Maui Rawinsonde Data: 1557 UTC 8 December 1987

December 87 - Flight 11

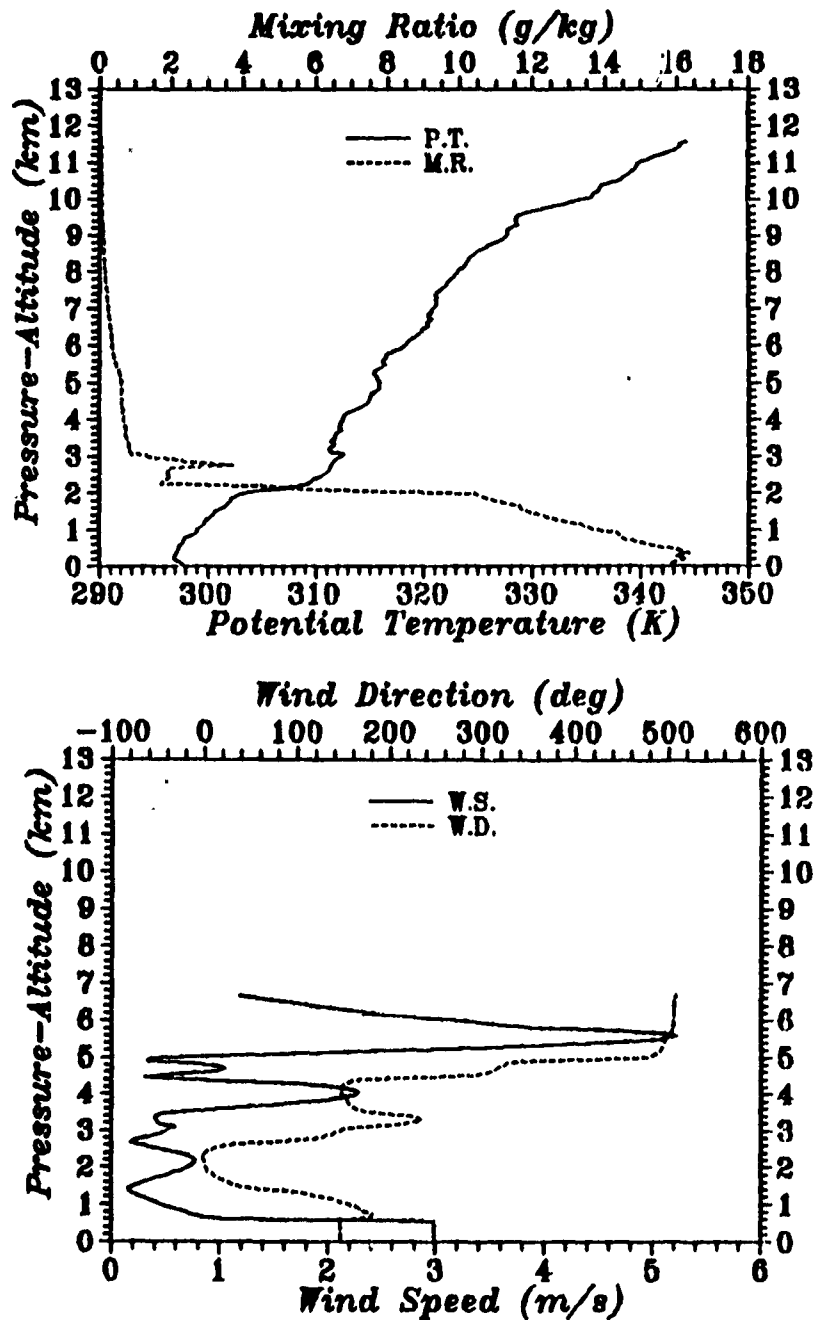


Fig. 36. Kilauea, Maui Rawinsonde Data: 0345 UTC 9 December 1987

December 87 - Flight 12

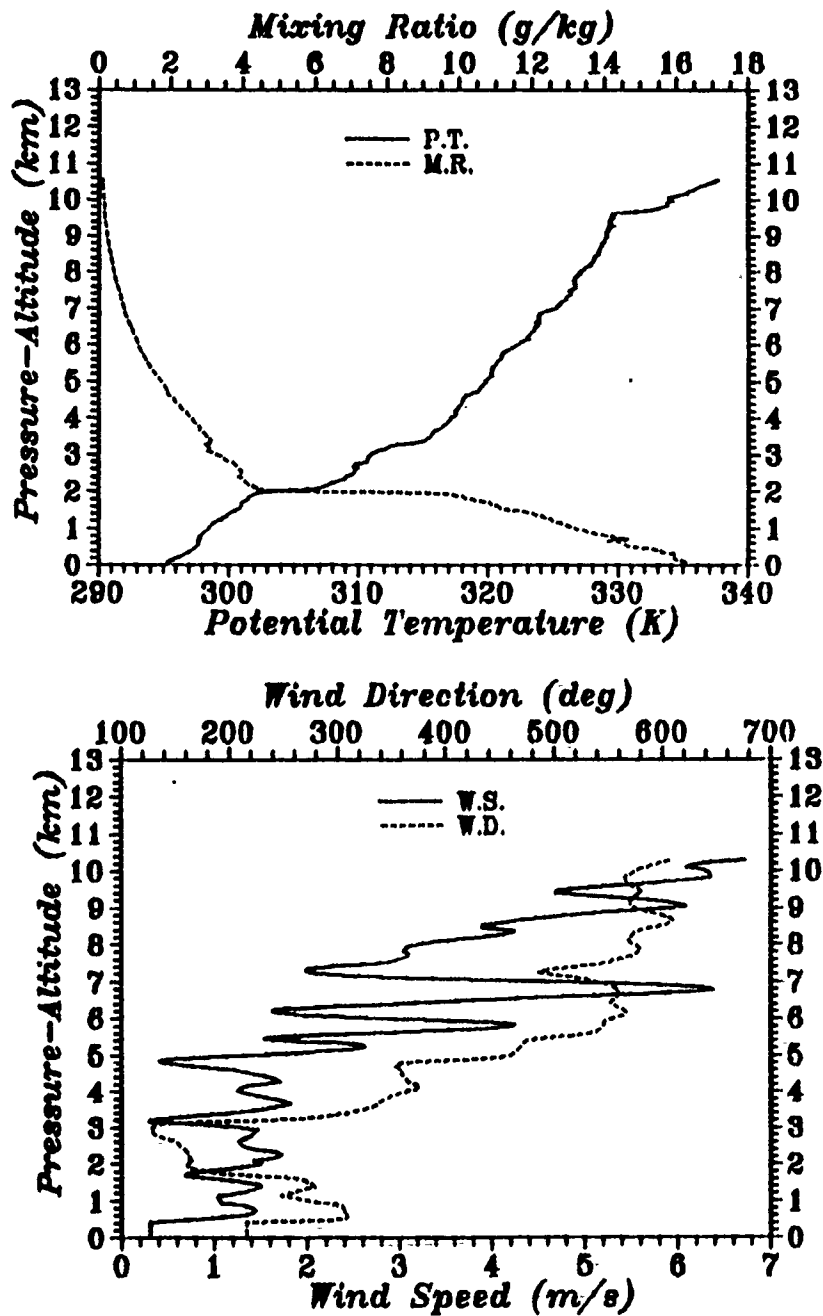


Fig. 37. Kihei, Maui Rawinsonde Data: 0958 UTC 9 December 1987

APPENDIX D. MAUI, HAWAII - APRIL 1988

A. METEOROLOGICAL DATA

Appendix D includes the April 1988 vertical profiles of atmospheric data acquired for the Relay Mirror Experiment at Kihei, Maui. The data acquisition system used was a Vaisala DigiCORA MW 11 rawinsonde system. Launch site was at 20.75° latitude, 156.43° longitude. The initial 2 km were sampled every two seconds (8-10 m). Data acquisition above 2 km was once every ten seconds (40-45 m). Flight number and launch times for all the April 1988 soundings are provided in Table 10.

Table 10. APRIL 1988 KIHAI, MAUI RAWINSONDE LAUNCHES

FLIGHT NO.	TIME (UTC)	DATE (DAY MON YR)
1	0610	27 April 1988
2	1548	27 April 1988
3	0605	28 April 1988
4	1549	28 April 1988
5	0605	29 April 1988
6	1558	29 April 1988
7	0544	30 April 1988
8	1434	30 April 1988

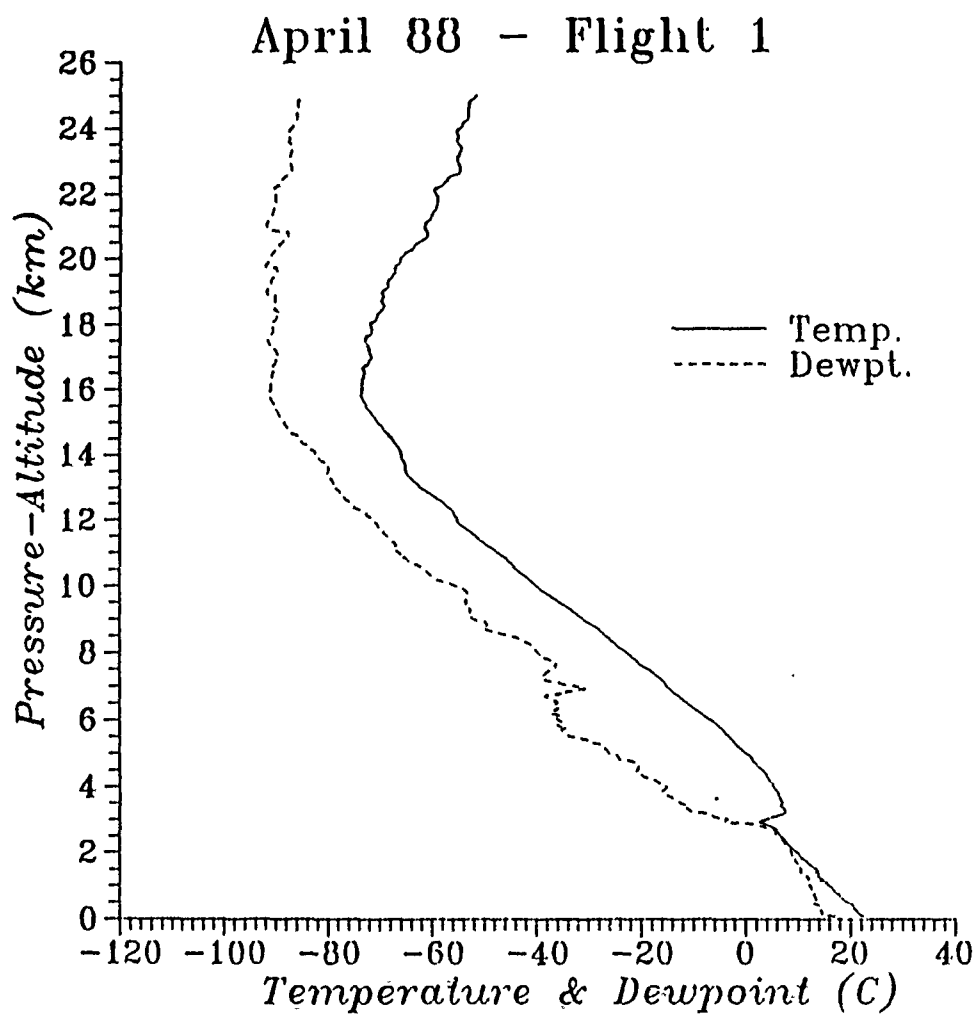


Fig. 38. Kihei, Maui Rawinsonde Data: 0610 UTC 27 April 1988

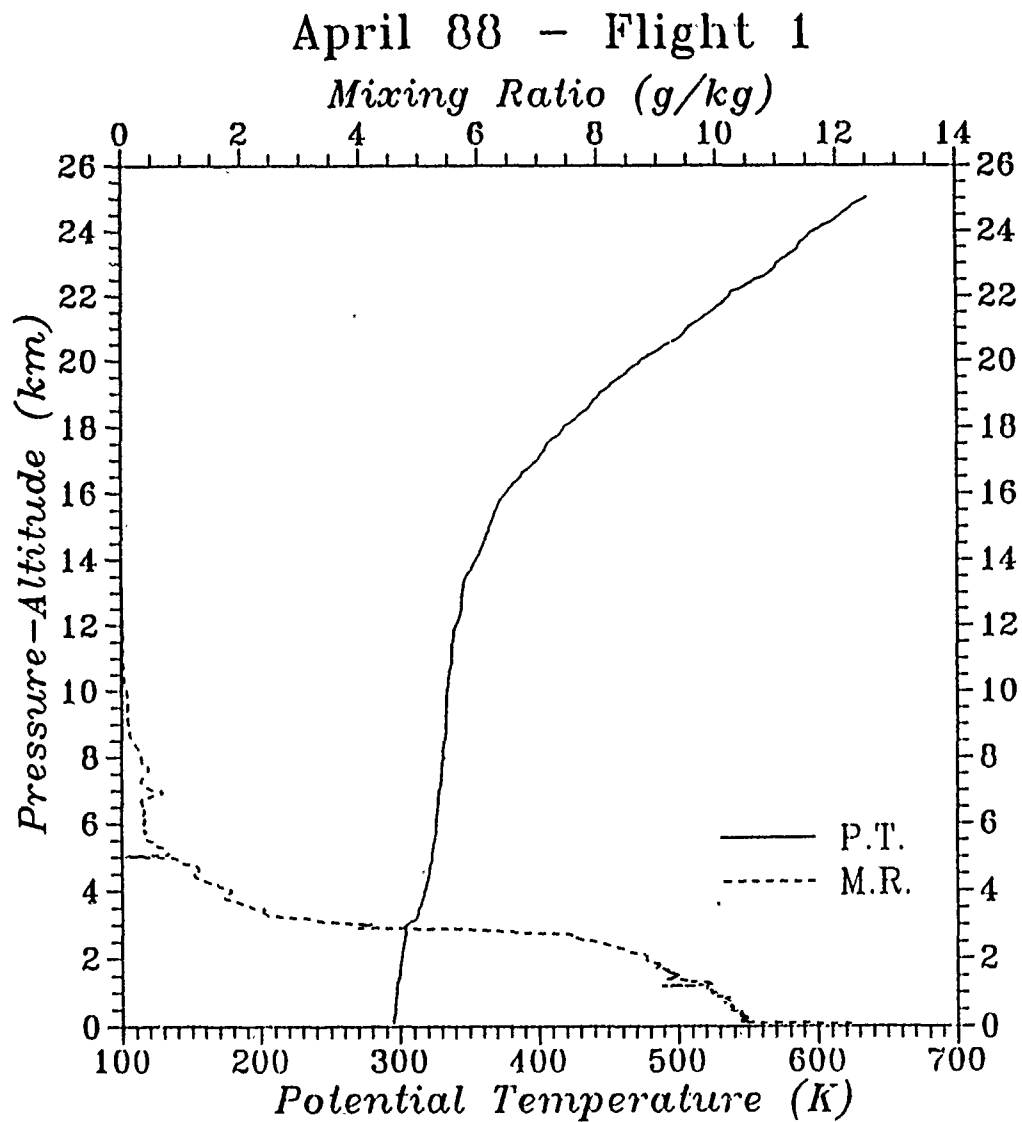


Fig. 39. Kilauea, Maui Rawinsonde Data: 0610 UTC 27 April 1988

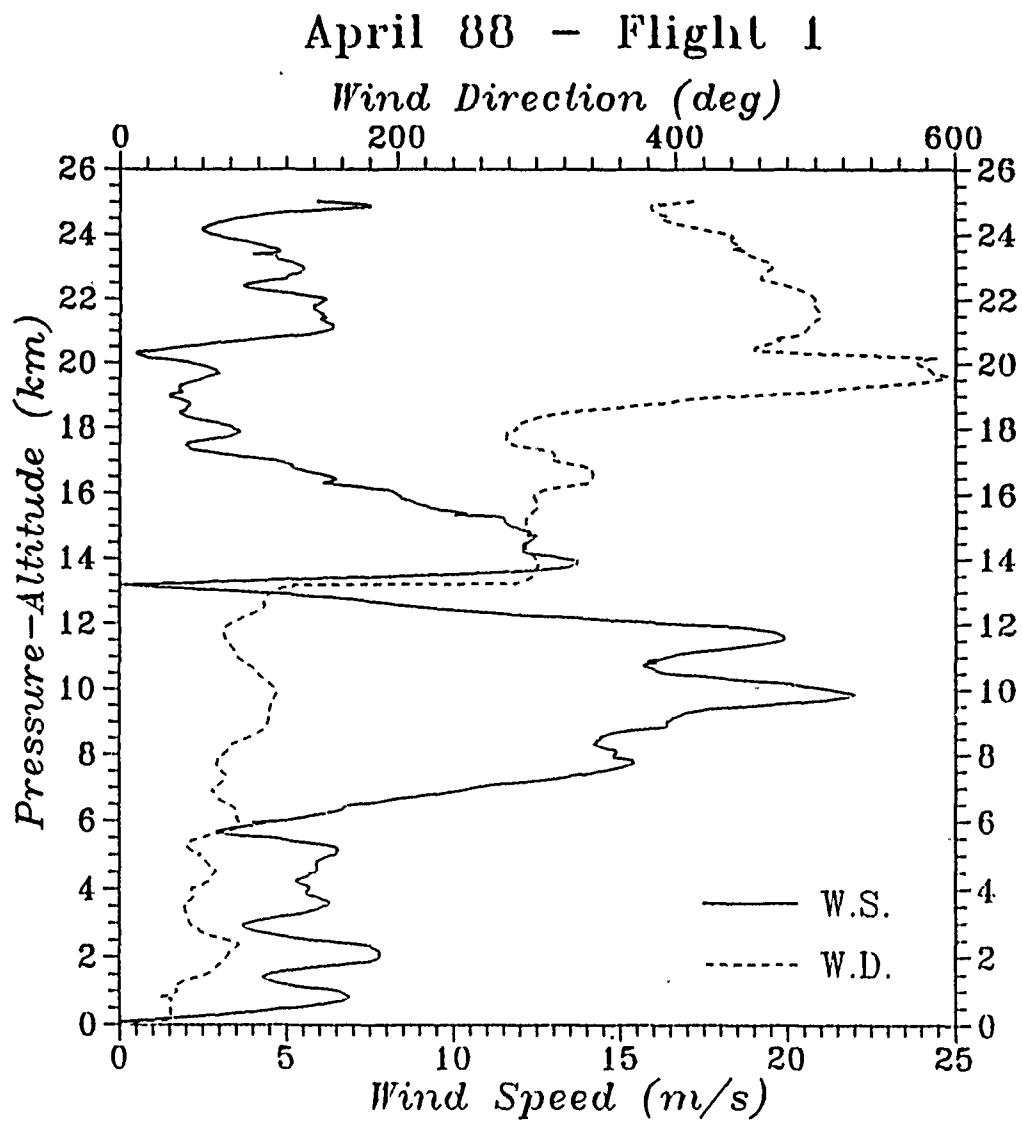


Fig. 40. Kilauea, Maui Rawinsonde Data: 0610 UTC 27 April 1988

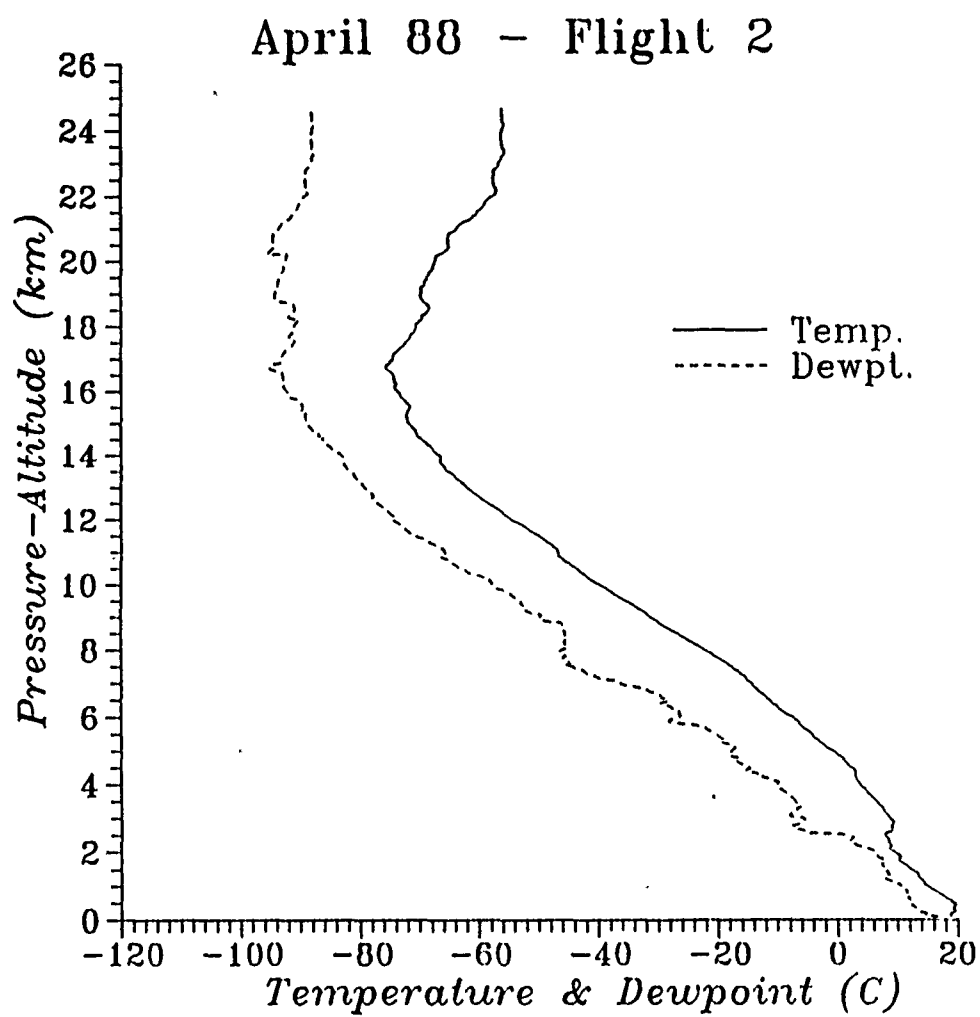


Fig. 41. Kihei, Maui Rawinsonde Data: 1548 UTC 27 April 1988

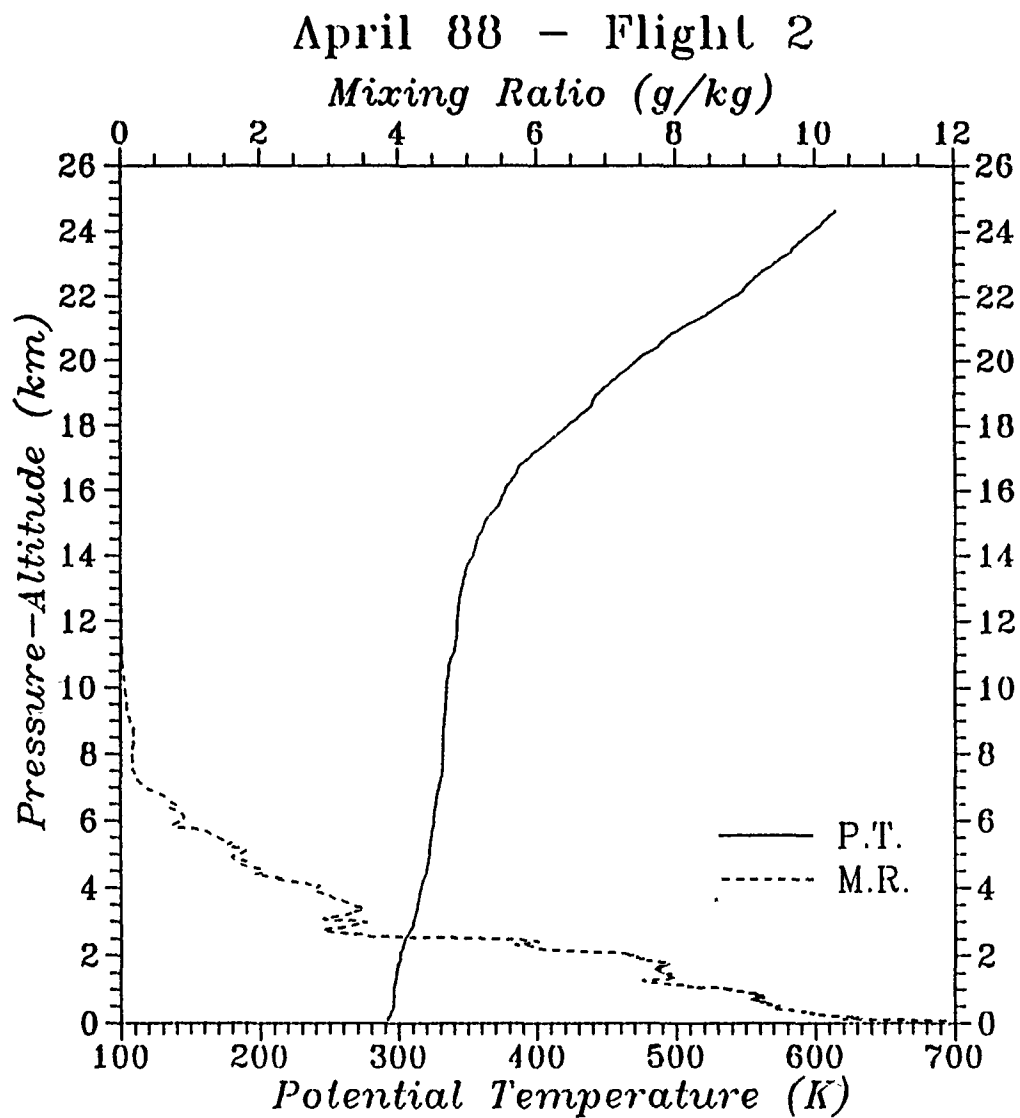


Fig. 42. - Kihei, Maui Rawinsonde Data: 1548 UTC 27 April 1988

April 88 - Flight 2

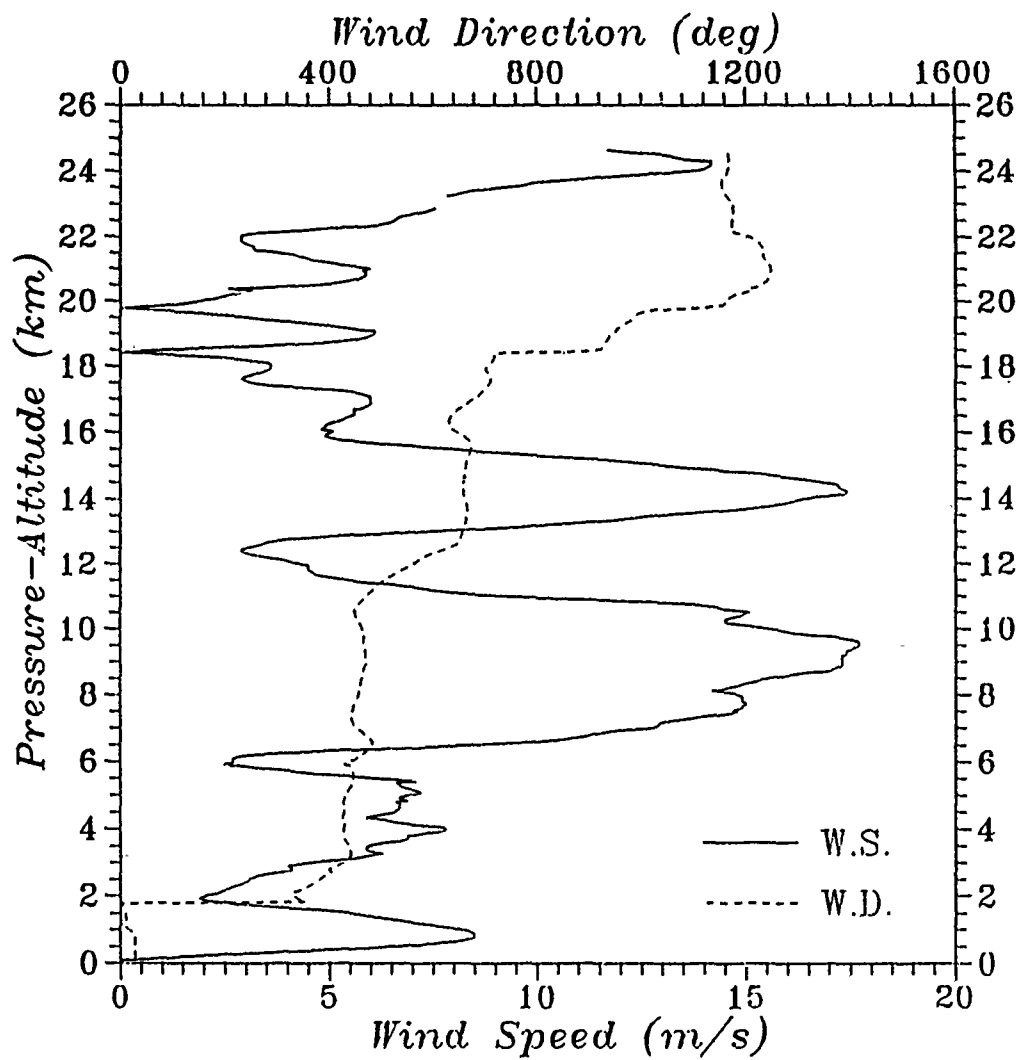


Fig. 43. Kihci, Maui Rawinsonde Data: 1548 UTC 27 April 1988

April 88 - Flight 3

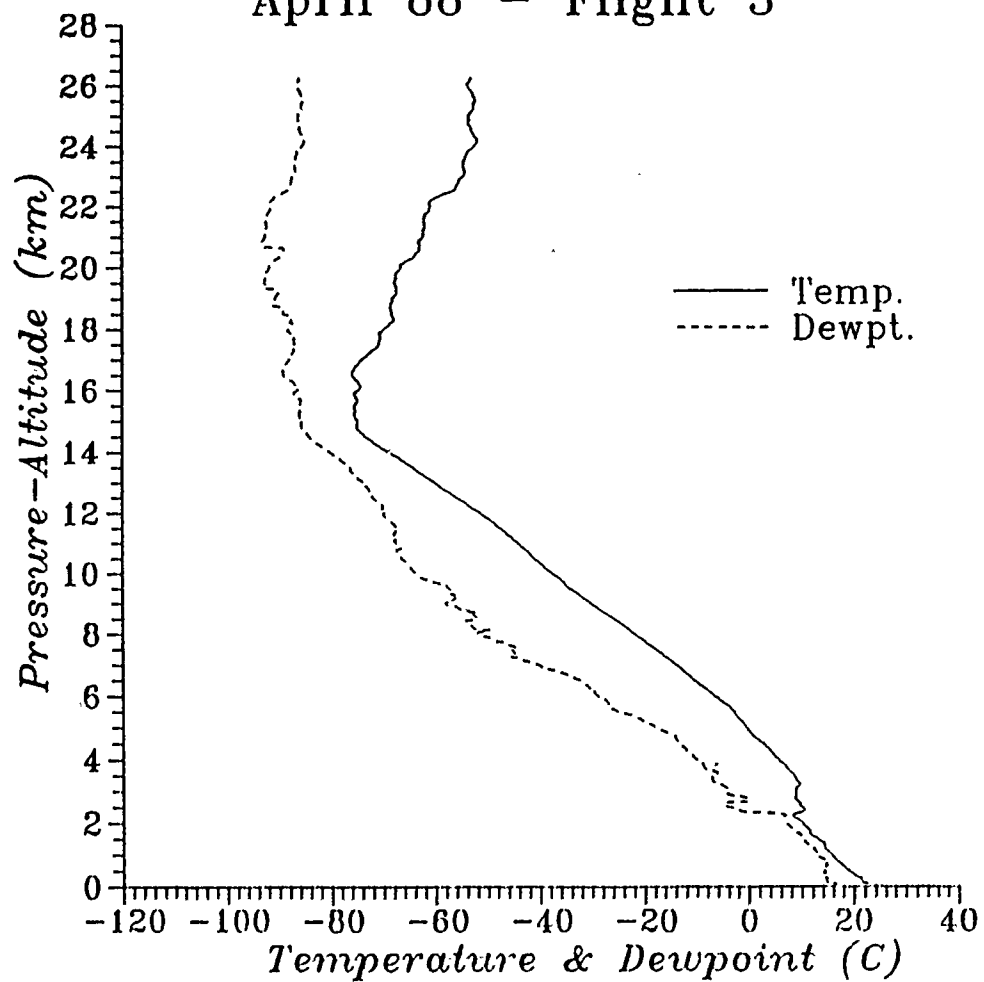


Fig. 44. Kihei, Maui Rawinsonde Data: 0605 UTC 28 April 1988

April 88 - Flight 3

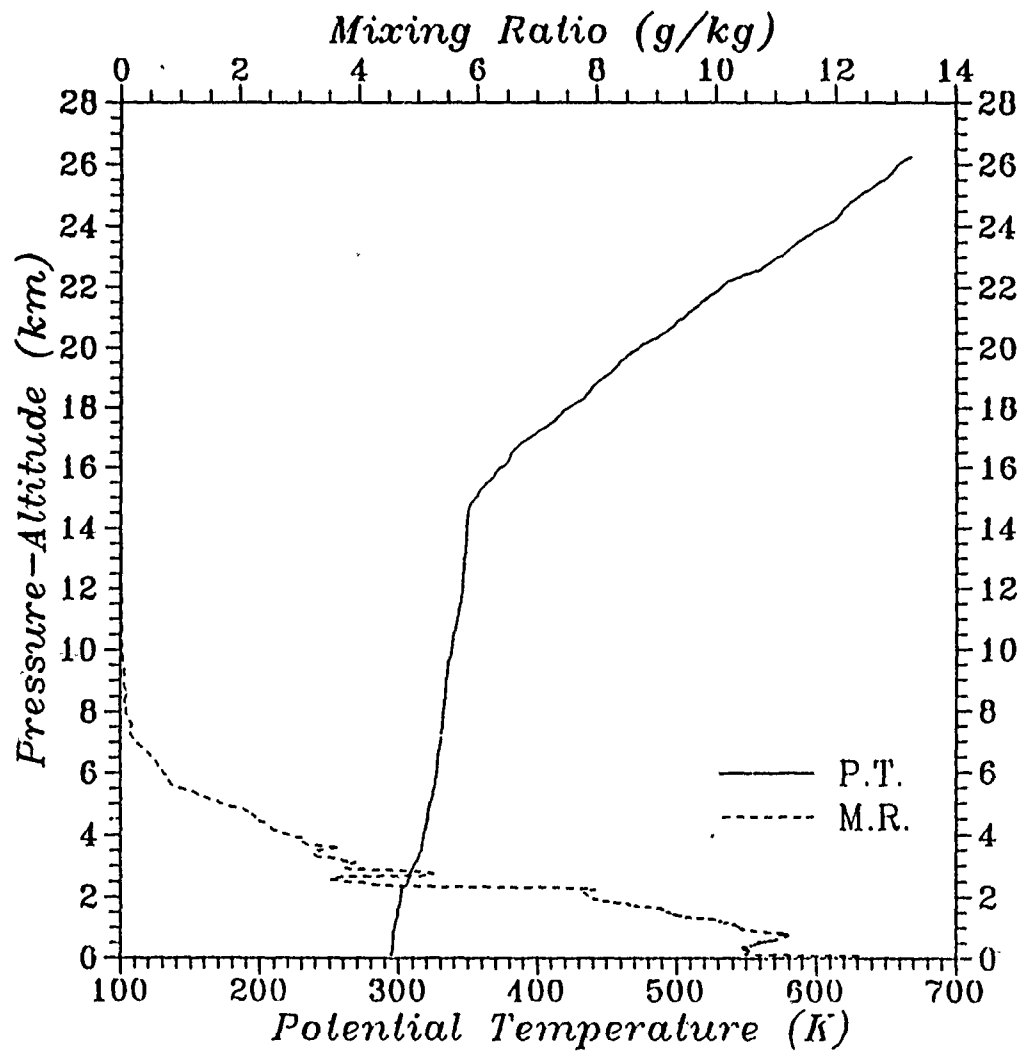


Fig. 45. Kihei, Maui Rawinsonde Data: 0605 UTC 28 April 1988

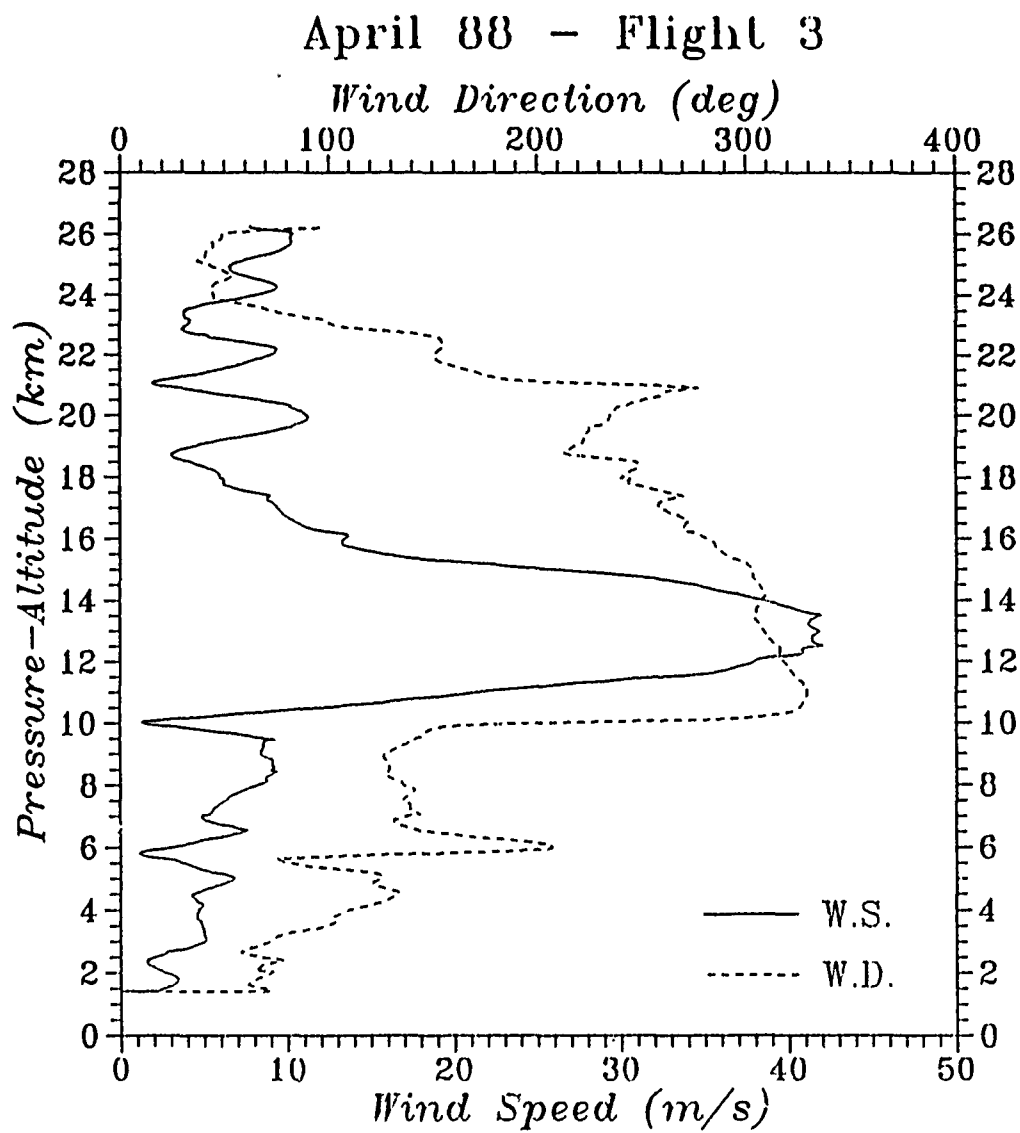


Fig. 46. Kihel, Maui Rawinsonde Data: 0605 UTC 28 April 1988

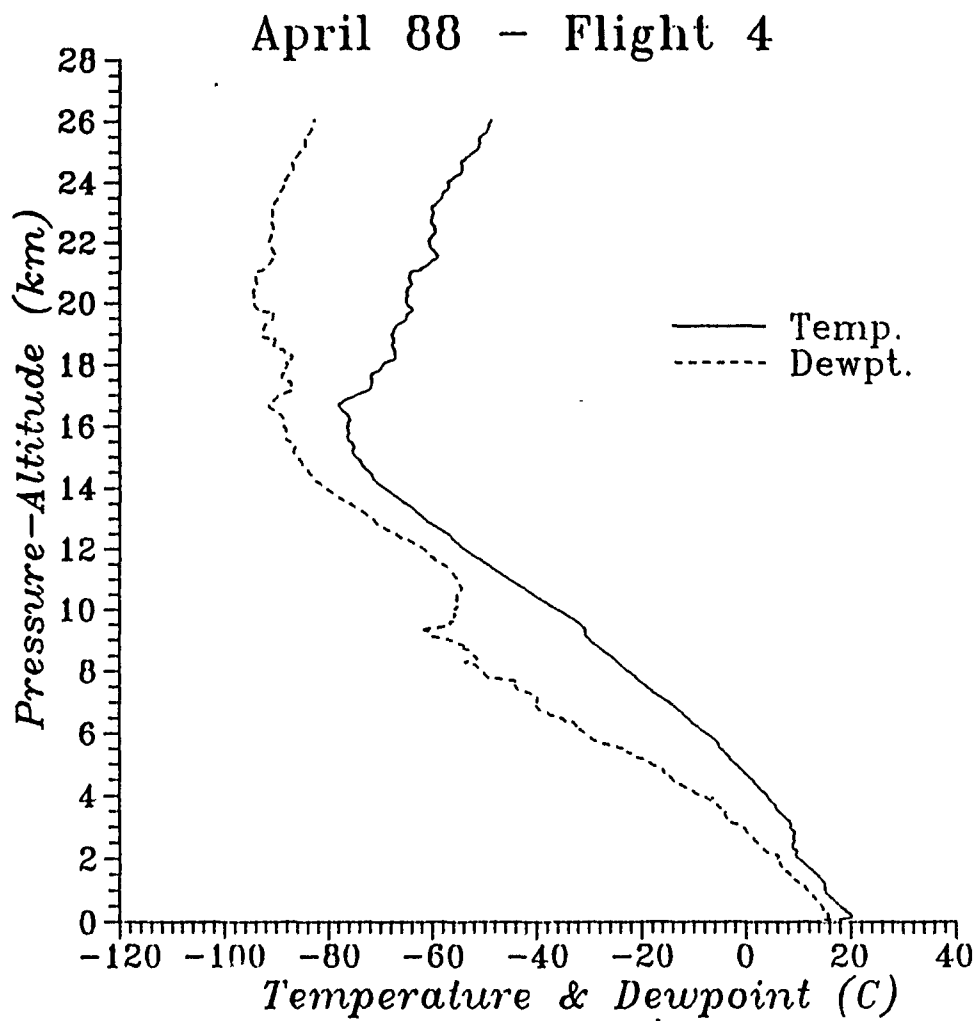


Fig. 47. Kihei, Maui Rawinsonde Data: 1549 UTC 28 April 1988

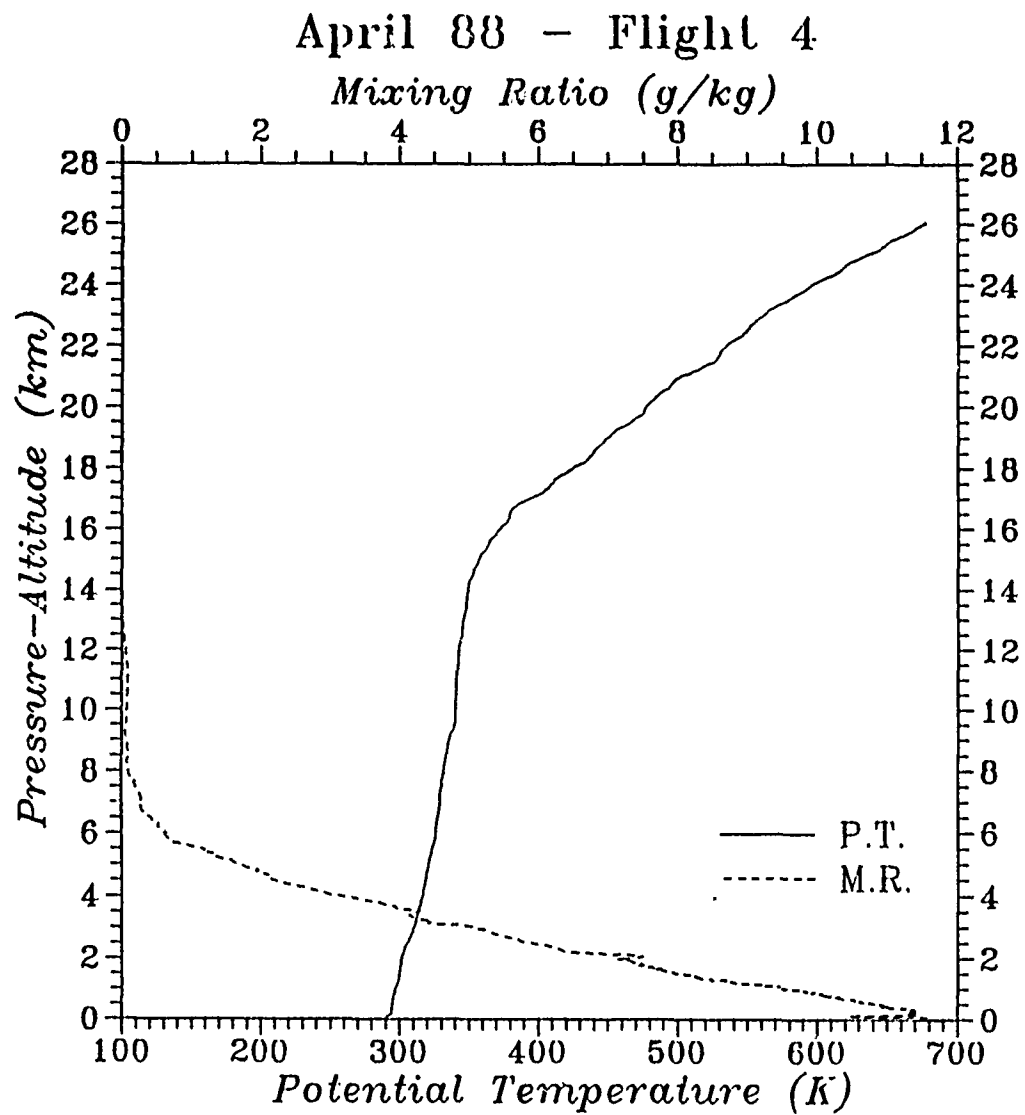


Fig. 48. Kihei, Maui Rawinsonde Data: 1549 UTC 28 April 1988

April 88 - Flight 4

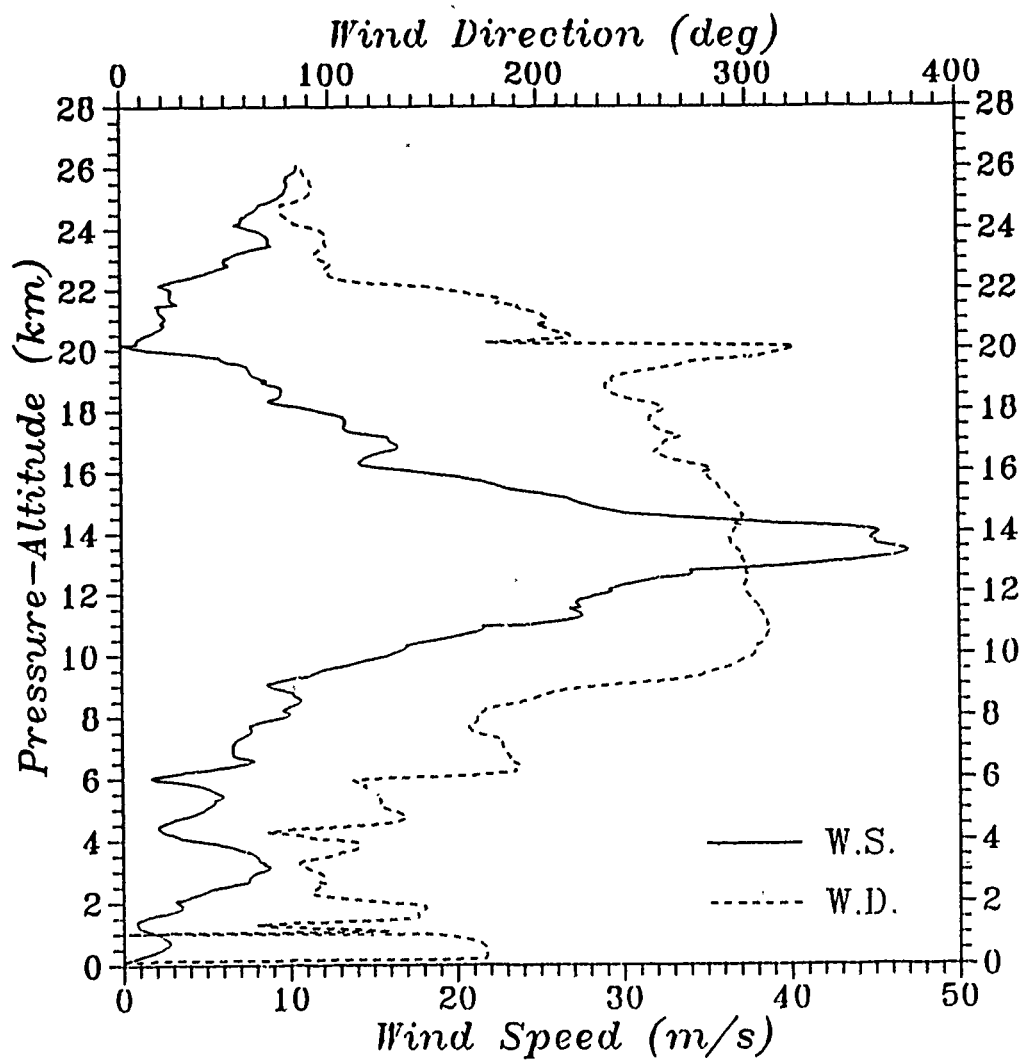


Fig. 49. Kihui, Maui Rawinsonde Data: 1549 UTC 28 April 1988

April 88 - Flight 5

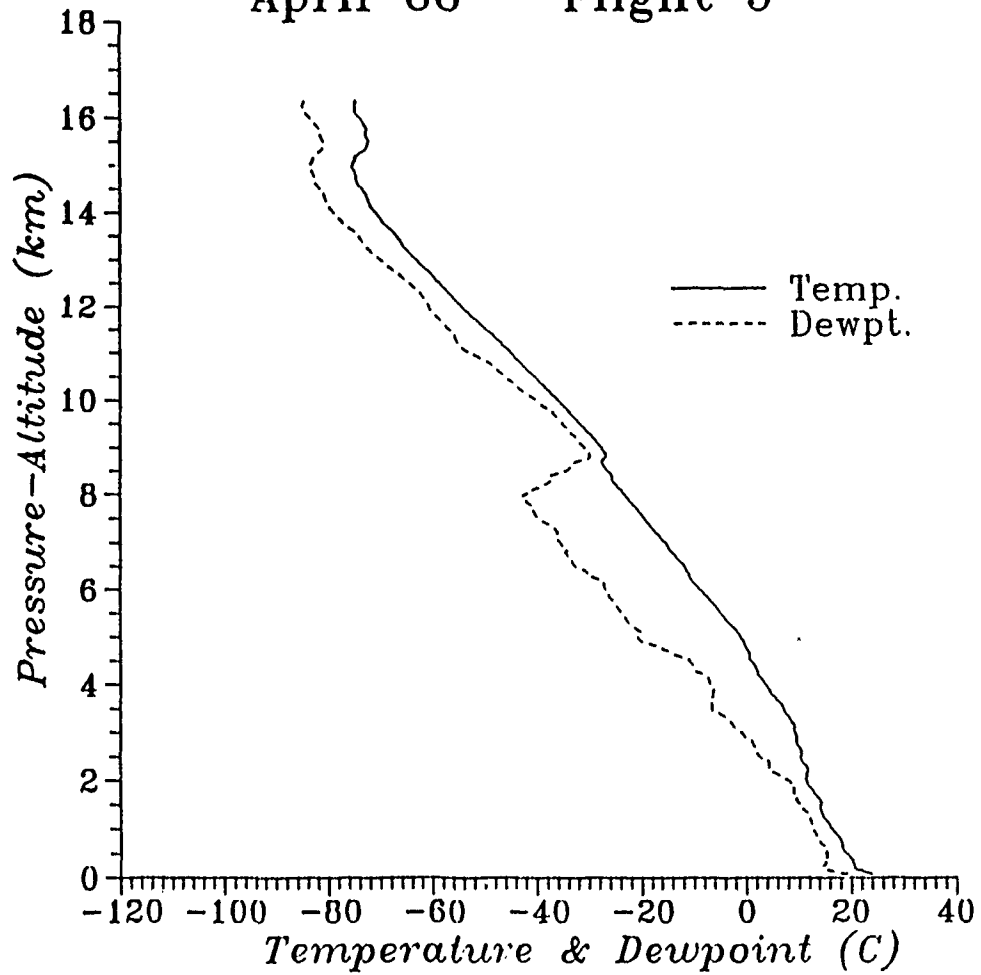


Fig. 50. Kihei, Maui Rawinsonde Data: 0605 UTC 29 April 1988

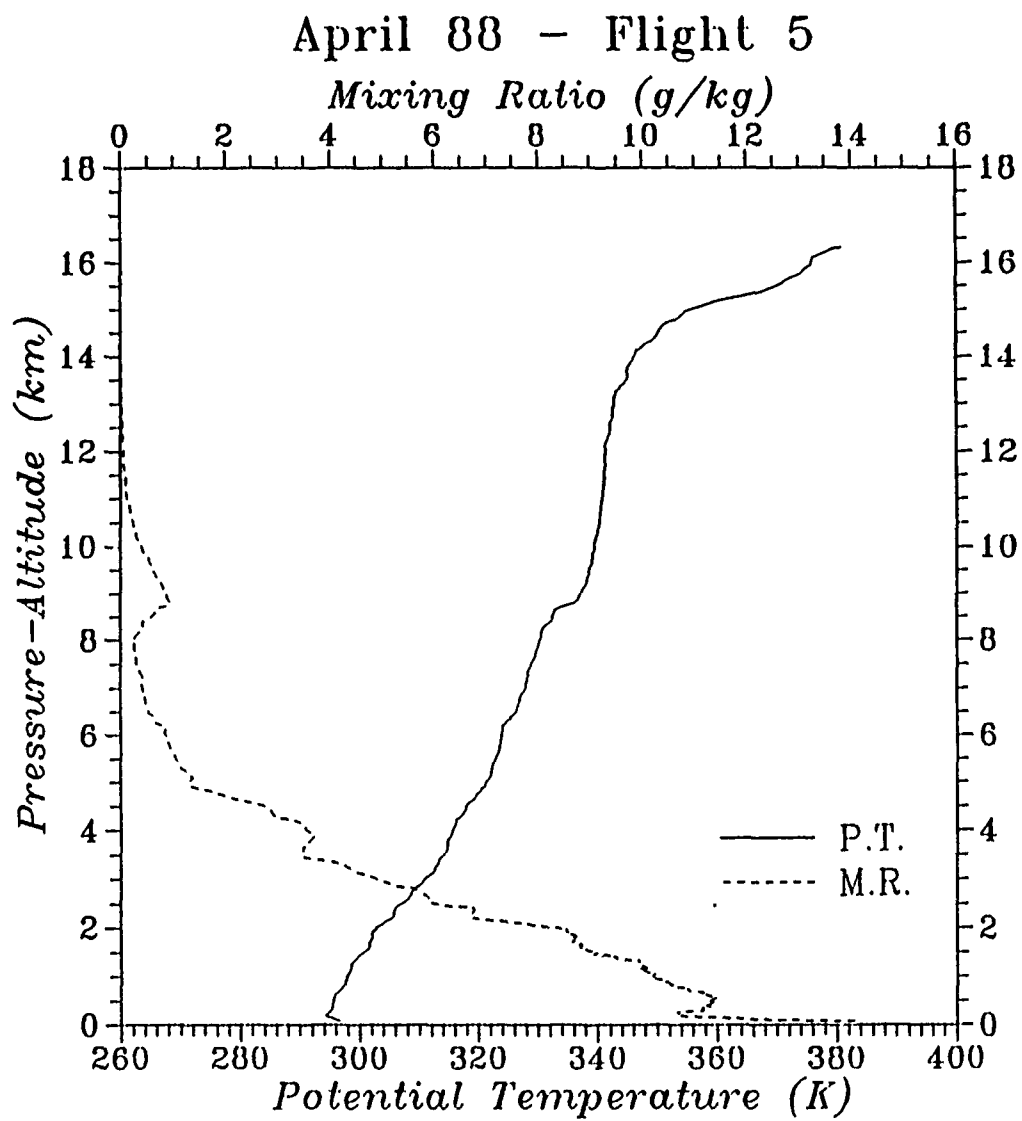


Fig. 51. Kihei, Maui Rawinsonde Data: 0605 UTC 29 April 1988

April 88 - Flight 5

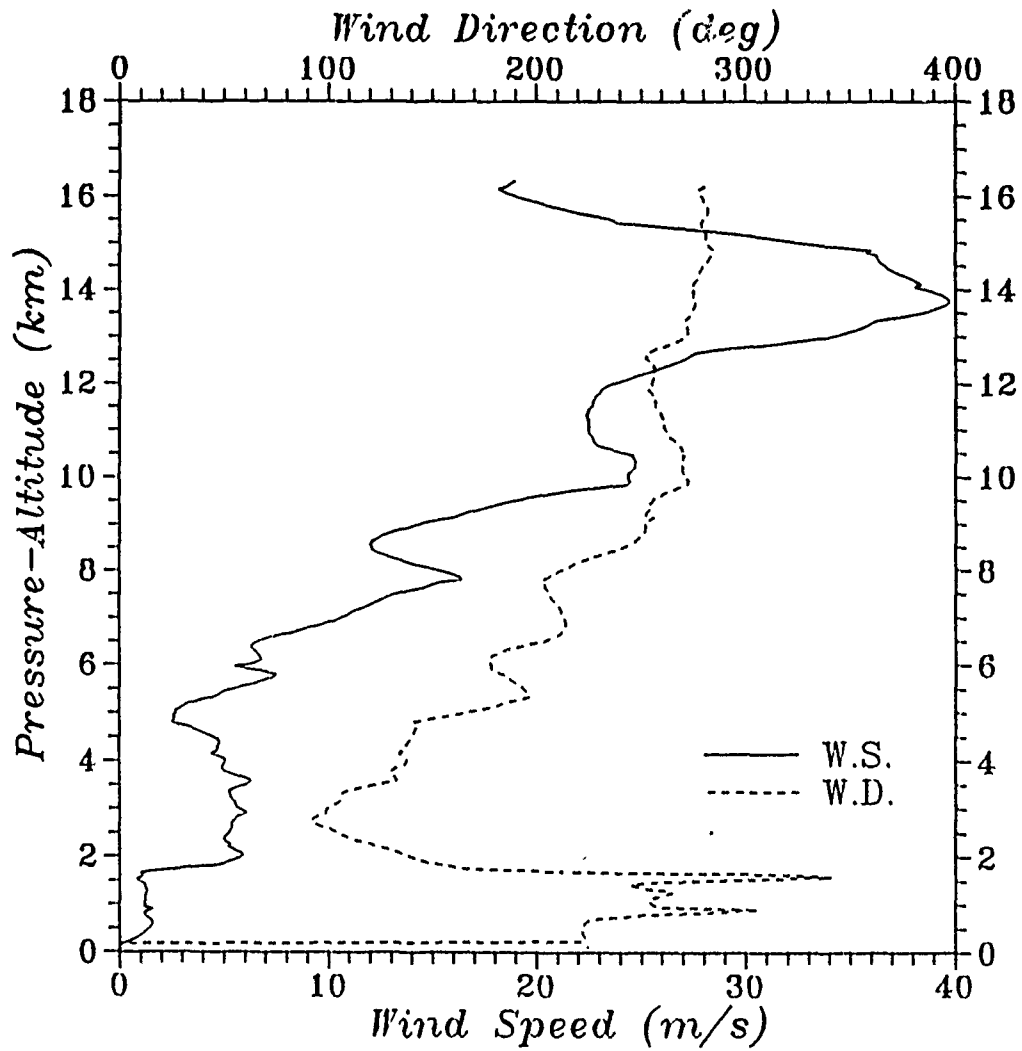


Fig. 52. Kihei, Maui Rawinsonde Data: 0605 UTC 29 April 1988

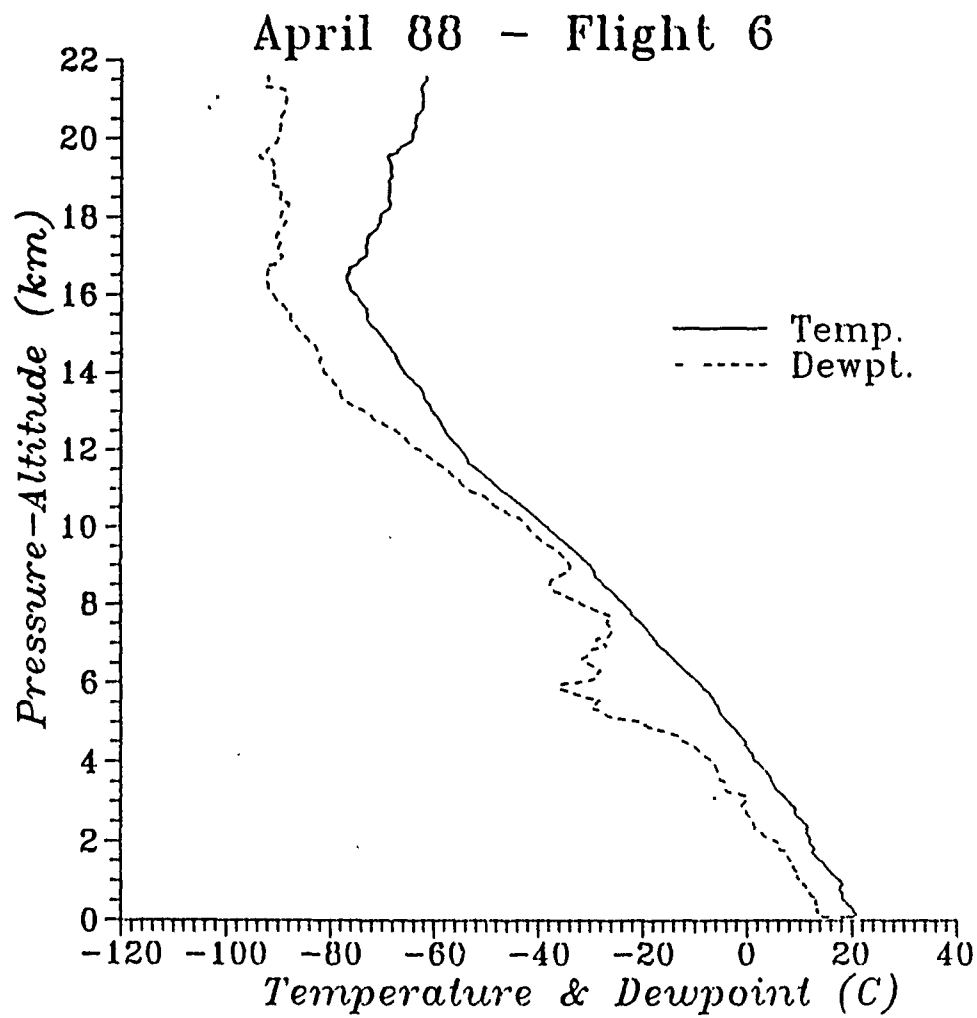


Fig. 53. Kilauea, Maui Rawinsonde Data: 1558 UTC 29 April 1988

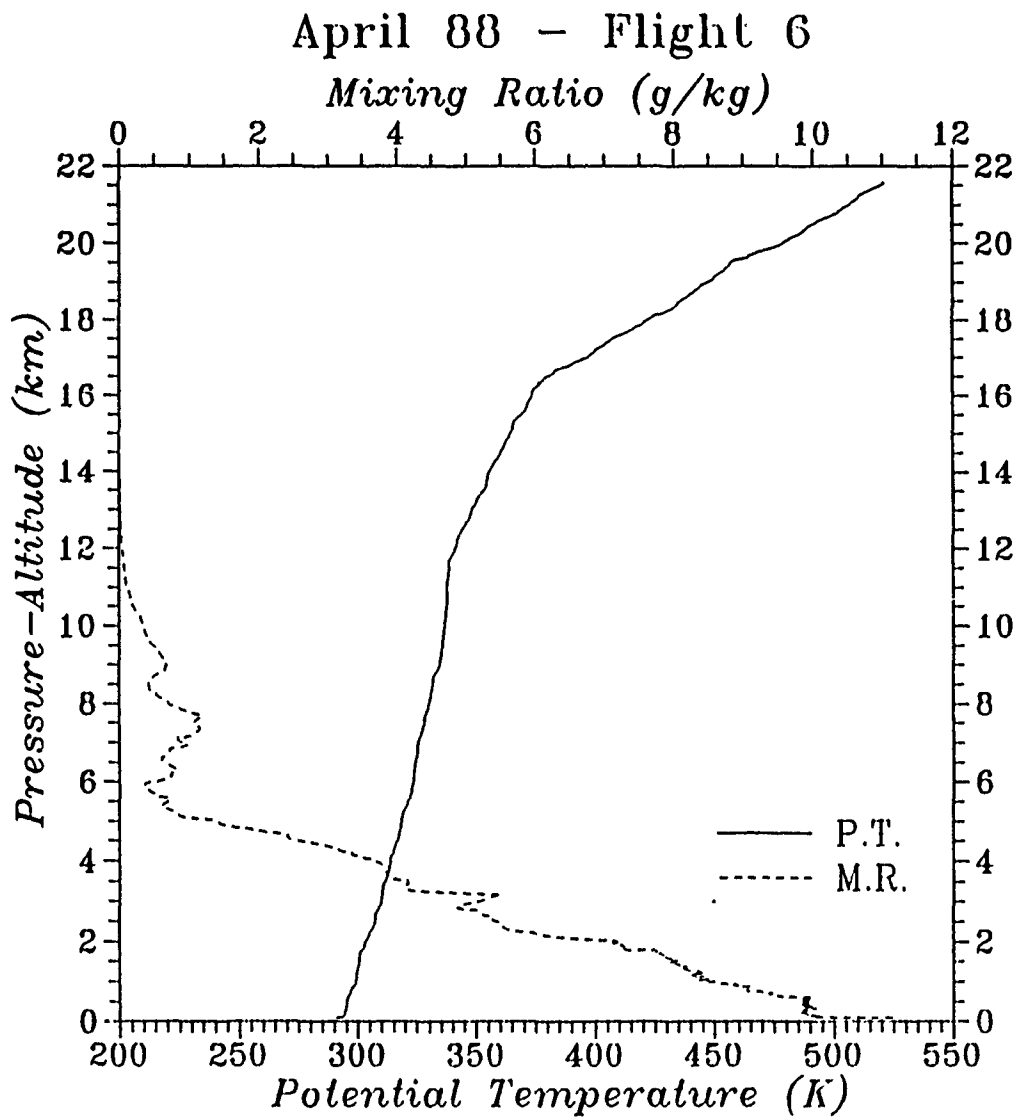


Fig. 54. Kihei, Maui Rawinsonde Data: 1558 UTC 29 April 1988

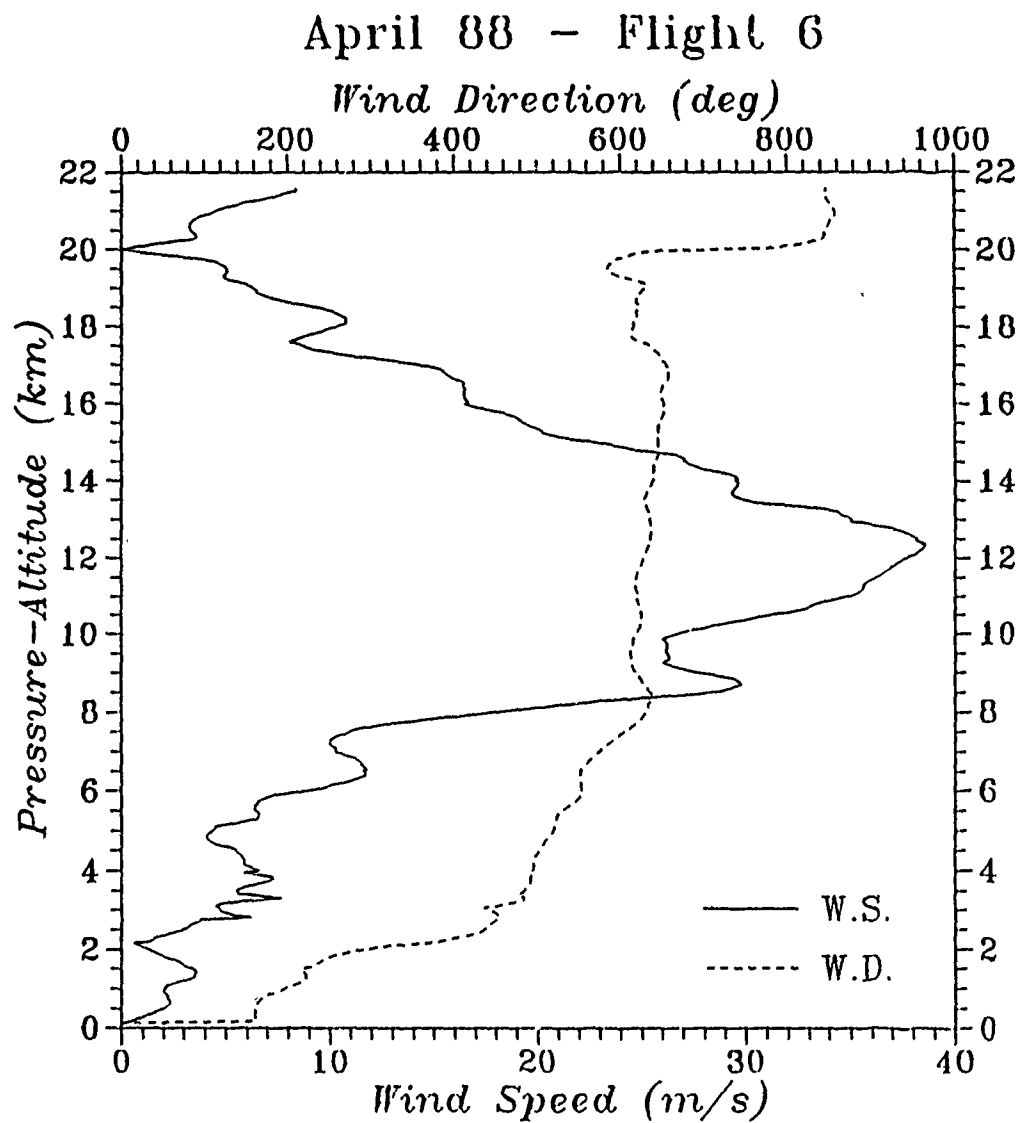


Fig. 55. Kilauea, Maui Rawinsonde Data: 1558 UTC 29 April 1988

April 88 - Flight 7

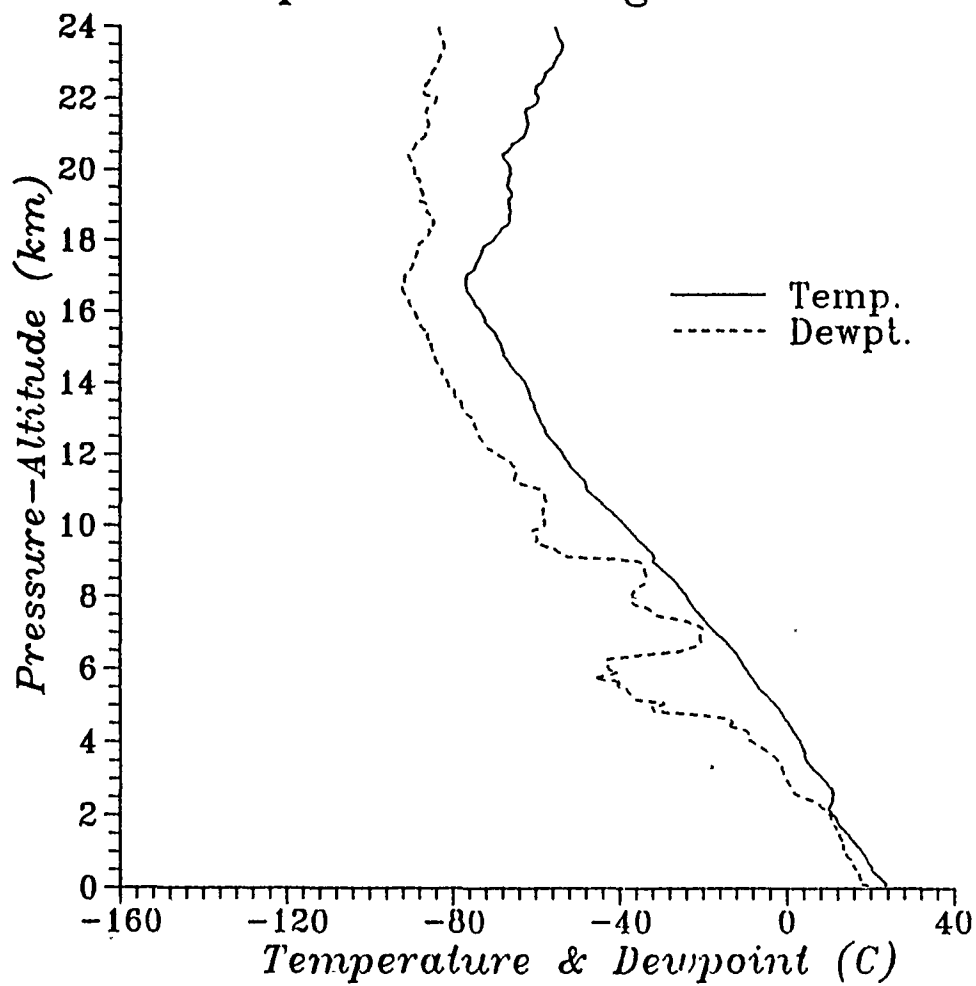


Fig. 56. Kihei, Maui Rawinsonde Data: 0544 UTC 30 April 1988

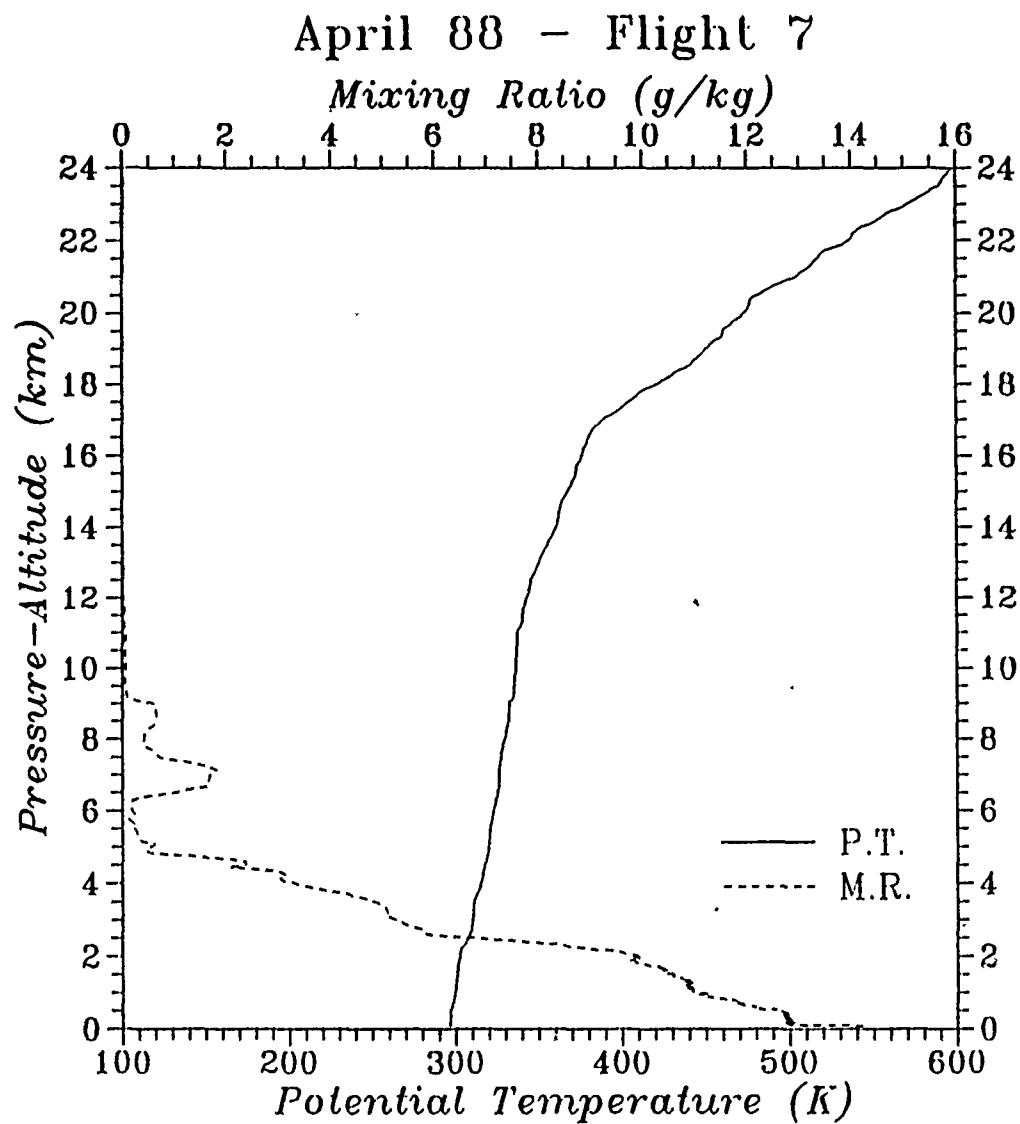


Fig. 57. Kīhei, Maui Rawinsonde Data: 0544 UTC 30 April 1988

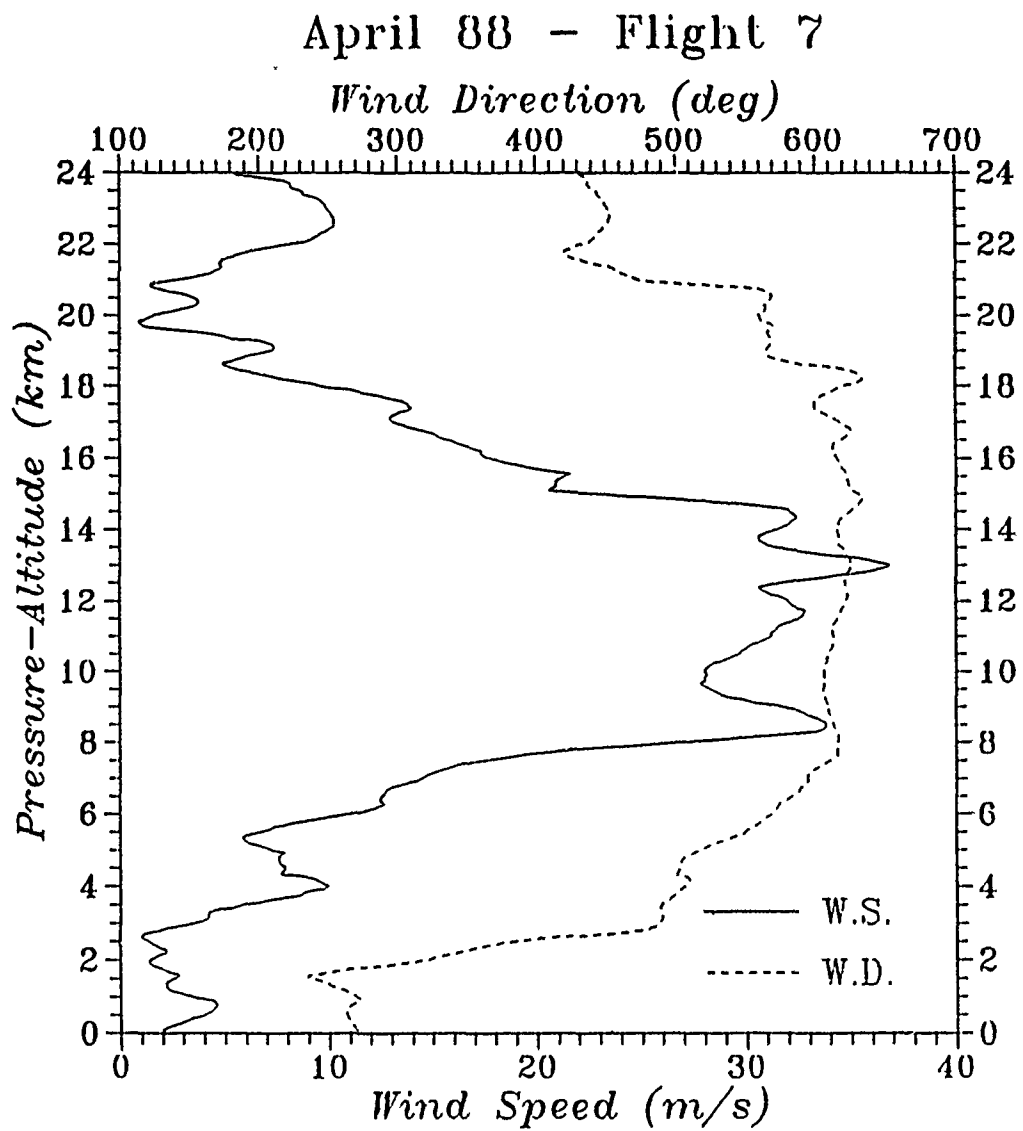


Fig. 58. Kihei, Maui Rawinsonde Data: 0544 UTC 30 April 1988

April 88 - Flight 8

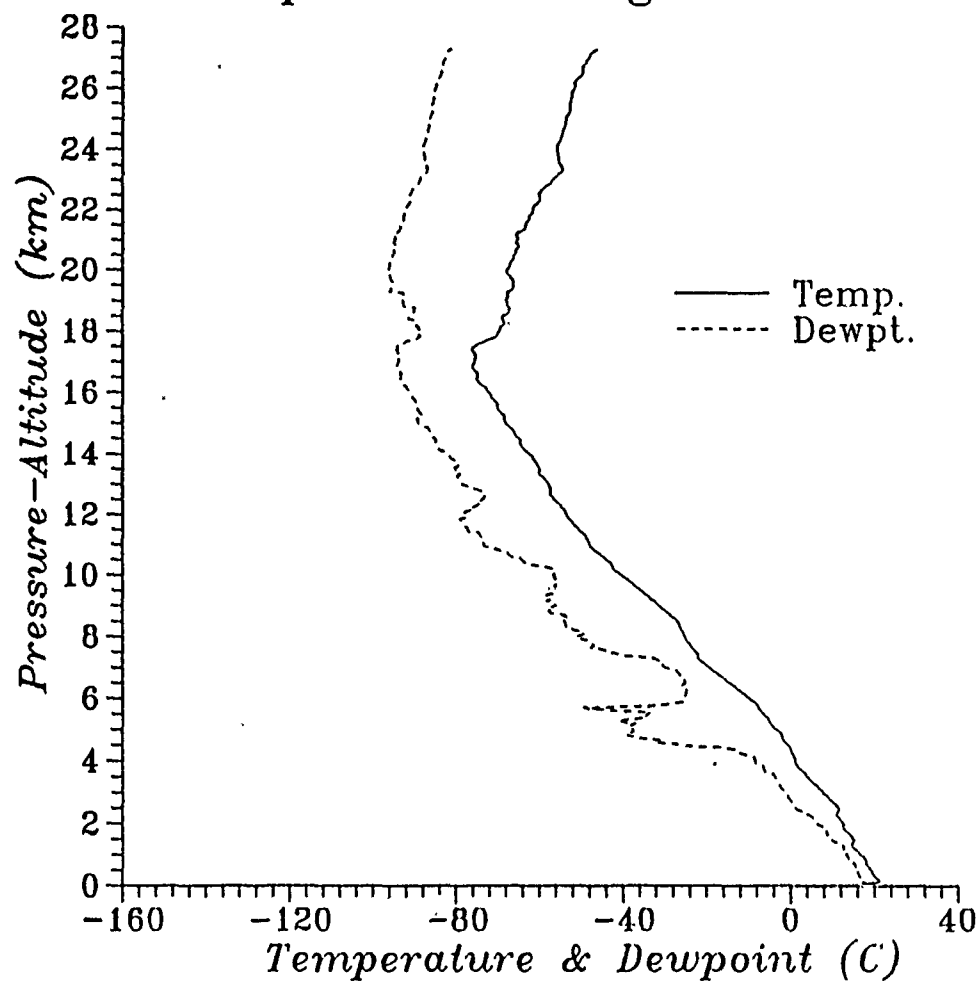


Fig. 59. Kilauea, Maui Rawinsonde Data: 1434 UTC 30 April 1988

April 88 - Flight 8

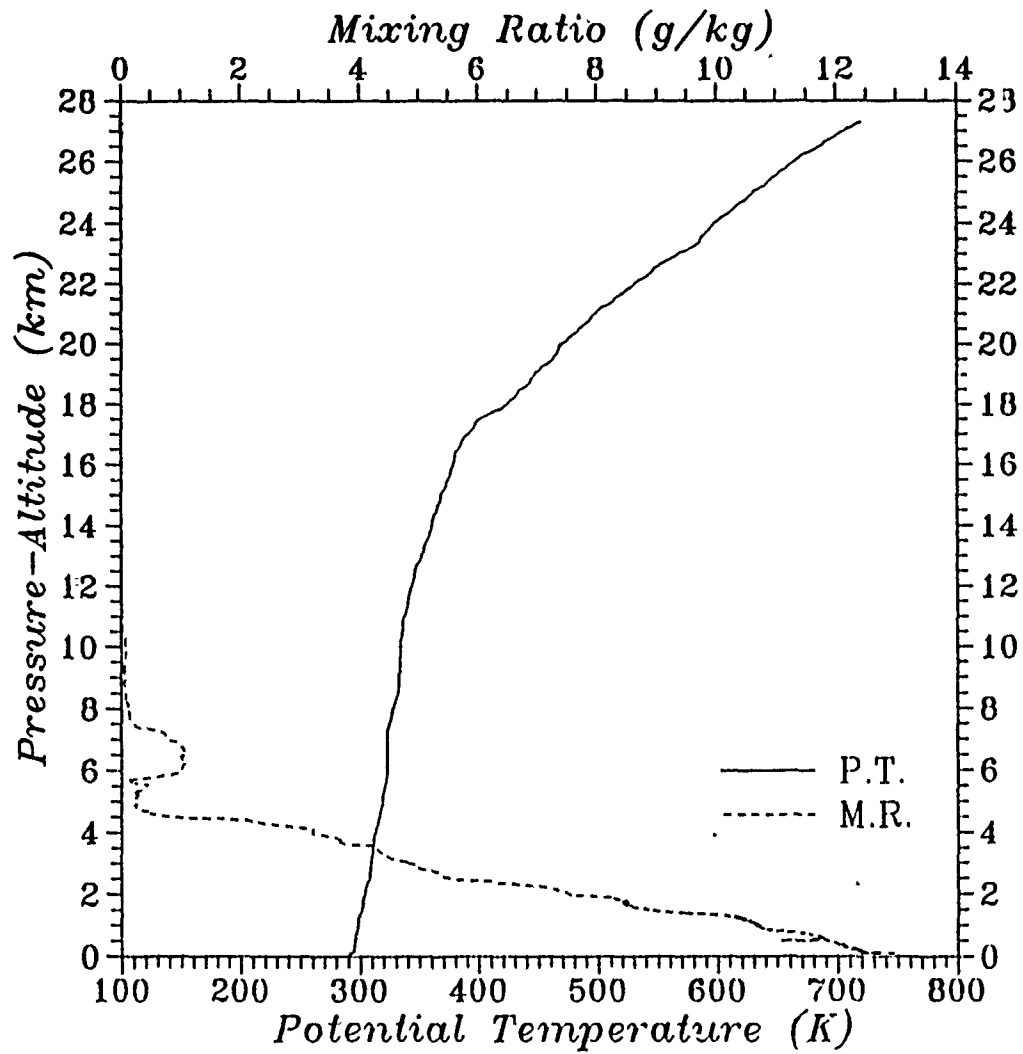


Fig. 60. Kilauea, Maui Rawinsonde Data: 1434 UTC 30 April 1988

April 88 - Flight 8

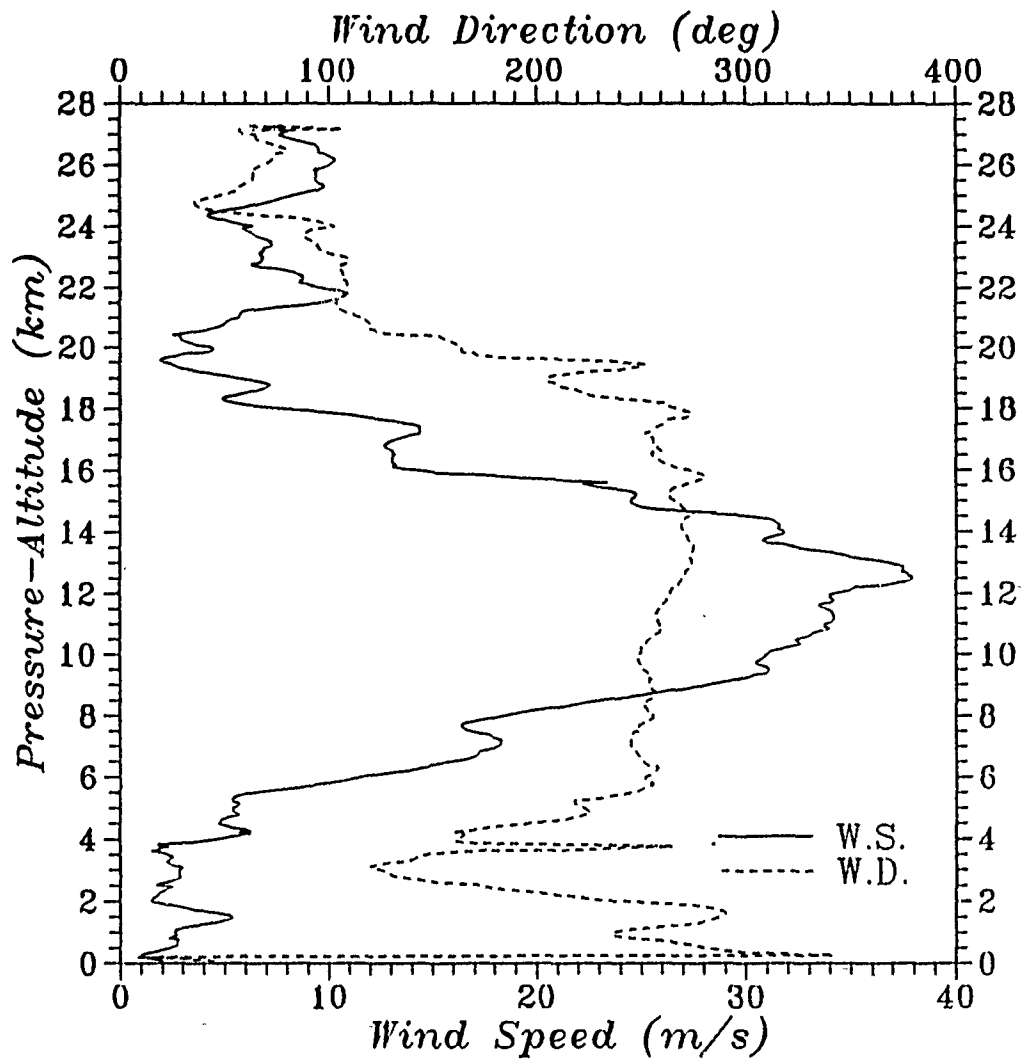


Fig. 61. Kihei, Maui Rawinsonde Data: 1434 UTC 30 April 1988

B. APRIL 1988, EXPERIMENT REPORT

The following is a general meteorological summary corresponding to the optical data measured during the 27 April 1988 (UTC) through 01 May 1988 (UTC) Kihei, Maui, Hawaii Experiment.

1. 0600-1730 UTC 27 April 1988

Extensive cloud cover prohibited optical measurements until approximately 1100 UTC. The 0610 UTC Kihei rawinsonde launch includes the following surface parameters:

P (Pressure) = 1005.9 mb

T (Temperature) = 22.6° C

RH (Relative Humidity) = 71%

Wind Speed, Wind Direction = calm (< 2m/s), N/A

Stability = unstable between surface and 0.2 km

The stratus deck restricting optical measurements occurs between 2.2-2.7 km, and extends horizontally to the NE 3-5° latitude according to the GOES-WEST Infrared (IR) Satellite Image taken within 30 minutes of balloon launch time. A temperature inversion of 5.1° C between 2.9 and 3.2 km caps the cloud layer, and is coupled with light winds (< 5 m/s) from the NE.

Winds gradually increase with height until 9.9 km (289.7 mb) where a maximum wind speed of 22.0 m/s is reported. Wind direction remains from the eastern quadrants (0-180° from the North) up to 13.2 km (173.1 mb). Within the next 97m (174.4-171.1 mb) moderate winds become calm and veer 201 degrees. The subsequent increase in wind speed peaks at 13.7 m/s (143.2 mb) before it gradually decreases to winds of less than 10 m/s. Wind direction continues to be from the NW until 18.7 km (well after the initial signature of the tropopause) where it crosses into the eastern quadrants for the remainder of the vertical sampling. The rawinsonde flight is terminated after 90 minutes 10 seconds at 25.019 km (24.9 mb).

Comparing the 0546 UTC and the 1246 UTC IR Satellite Images, the dense stratus deck moves from NE of the site to SW. The 1246 UTC and 1446 UTC IR Satellite Images display very little change in the intermittent stratus deck, though r_0 measurements indicate a 1 cm increase over the same time interval.

Shortly before sunrise (1548 UTC 27 April 1988) a second rawinsonde launch records the following surface parameters:

P (Pressure) = 1005.3 mb

T (Temperature) = 18.8° C

RH (Relative Humidity) = 87%

Wind Speed, Wind Direction = calm (< 2m/s), N/A
Stability = stable conditions

The first of two inversions is found between the surface (0.083 km) and 0.257 km. A second slight temperature increase of 0.4°C (0.365-0.430 km) is capped by a small humidity increase of 13% between 0.459-1.012 km. The small temperature inversion is supported by 0.9 m/s increase in wind speed. Wind direction remains constant at 28° . Another increase in moisture content is displayed between 1.270-1.737 km. The RH maximum of 83% is reported at 1.737 km. Winds sampled thus far are light and from the NE, NNE. For a thin layer, 1.782-2.275 km, the light winds back to northwesterlies. A sharp decrease of 52% RH (2.075-2.713 km) overlaps the variable winds. Embedded within this layer is a 1.5°C inversion between 2.511-2.824 km. Except for a slight moisture increase between 7.754-8.824 km, the remainder of the sounding displays an extremely dry atmosphere. At 9.520 km, winds reach a peak velocity of 17.7 m/s. At a slightly higher level, 10.558-12.396 km, wind speed decreases 11.9 m/s and veers 163 degrees. The veering continues another 54 degrees over the next 0.943 km. The temperature gradient associated with the 217 degree wind shift is $-20^{\circ}\text{C}/2.781\text{ km}$ ($2.61^{\circ}\text{C}/\text{km}$ less than the dry-adiabatic lapse rate). The tropopause begins around 17.3 km.

2. 0600-1730 UTC 28 April 1988

Kihei rawinsonde surface measurements recorded at 0605 UTC include:

P (Pressure) = 1005.3 mb
T (Temperature) = 22.6°C
RH (Relative Humidity) = 72%
Wind Speed, Wind Direction = calm (< 2m/s), N/A
Stability = unstable between surface and 0.2 km

RH reaches a maximum of 91% just prior to the first of two inversions. The initial inversion is between 2.254-2.430 km (778.4-762.0 mb). This 2.3°C increase is coupled with an 8 degree veering of winds, and no change in wind speed. The second inversion is fragmented into two parts. The total layer displays a 1.1°C increase over 0.4 km (2.793-3.193 km). Winds associated with this stable layer increase by 1 m/s and veer 15 degrees. As before, the inversion is preceded by a slight increase (+18%) in RH.

Between 5.627 km and 6.004 km light winds veer 132 degrees NEE to SW. The temperature gradient associated with this large wind shift is $-3^{\circ}\text{C}/3.77\text{ km}$ ($1.842^{\circ}\text{C}/\text{km}$ less than the dry-adiabatic lapse rate).

Another large veering in wind direction is between 8.951-10.830 km. This 203 degree change is coupled with a 9.9 m/s increase in wind speed and a temperature gradient of $-13.2^{\circ}\text{C}/1.879\text{ km}$ ($2.775^{\circ}\text{C}/\text{km}$ less than the dry-adiabatic lapse rate).

The jet stream occurs between 11.561-14.431 km and flows from the NNW,NW. Peak winds of 42.1 m/s at 315° are evident at 12.493 km. The temperature gradient across the jet is $-24.7^{\circ}\text{C}/2.870\text{ km}$ ($-8.606^{\circ}\text{C}/\text{km}$). The Lihue rawinsonde data recorded about 5.25 hours after the local Kihei launch displays the jet stream between 12.354-14.580 km (wind direction across the jet backs from 292° to 279°). Temperature gradient associated with Lihue's jet stream measurements is approximately $-19.0^{\circ}\text{C}/2.652\text{ km}$ ($7.164^{\circ}\text{C}/\text{km}$). Peak wind is reported as 42.8 m/s, 286° at 13.487 km; 42.8 m/s, 283° at 13.940 km (Note: r_0 is 5 cm during both sampling intervals 0605 and 1115 UTC.)

At 1549 UTC 28 April 1988, surface measurements are:

P (Pressure) = 1005.3 mb

T (Temperature) = 17.9°C

RH (Relative Humidity) = 90%

Wind Speed, Wind Direction = calm ($< 2\text{m/s}$), N/A

Stability = stable

A 2.3°C inversion, as well as a 14% drop in RH, marks the first 84 m of the vertical profiles. Winds remain light and variable for the initial 2 km. A second minor inversion is between 2.368 and 2.807 km displaying a temperature gradient of $0.5^{\circ}\text{C}/0.438\text{ km}$ ($1.134^{\circ}\text{C}/\text{km}$). The easterly winds associated with this event increase 2.6 m/s and veer 6 degrees.

A general wind direction shift from eastern quadrants to western quadrants takes place around 500 mb (6.137 km). Note: 500 mb is often labelled a "level of non-divergence". The Level of Non-Divergence is defined as a "mid-tropospheric surface separating major regions of horizontal convergence and divergent associated with the typical vertical structure of the migratory cyclonic scale weather systems" (Huschke, 1970). In the upper half of the profile (above 500mb), RH increases at a rate of 36% in 2.664 km. This secondary peak of 49% RH is measured at 12.005 km. Nestled above the humidity influx is the jet stream, 12.765-14.448 km. Peak winds of 47.0 m/s are recorded at 13.319-13.361 km. The temperature gradient across the jet stream is $-12.3^{\circ}\text{C}/1.683\text{ km}$ ($-7.308^{\circ}\text{C}/\text{km}$).

3. 0600-1730 UTC 29 April 1988

Optical data gathering during this session was severely restricted by cloud cover from a synoptical scale weather system. Unlike previous nights, the 0605 UTC sounding reveals the near surface winds to be from the SW. (This implies the presence of an anabatic flow between Kihei and Haleakala.) The rest of the surface parameters are:

P (Pressure) = 1006.5 mb

T (Temperature) = 24.0° C

RH (Relative Humidity) = 75%

Wind Speed, Wind Direction = calm (< 2m/s), N/A

Stability = unstable between surface and 0.2 km

The vertical humidity profile displays two peaks. The first, a gradual 13%/km increase climaxing at 84% between 1.261-1.330 km. A minor 0.1° C/0.008 m inversion caps this first humidity maximum. The second peak follows a sharp 73%/km gradient that sends the humidity soaring to 75% at 8.976 km. Most significant to this sampling, however, is the wind profile. As stated before, near surface winds (0.219-1.682 km) are light and SW. A backing into the eastern quadrants follows and persists between 1.759-5.104 km. A 0.5° C inversion interrupts the atmospheric structure between 2.017-2.211 km. Above 5.1 km, winds veer into the western quadrants where they remain for the rest of the vertical sounding. The jet stream begins at 13.046 km and extends to 14.902 km. The maximum velocity sampled is 39.7 m/s (13.721-13.773 km). The temperature gradient accompanying the jet is -11.4° C/1.856 km (-6.142° C/km).

Using the 0546 UTC IR Satellite Image, the site appears in the area of a comma cloud where one would expect overrunning and warm advection; the warm front would be to the south. At 1146 UTC, the site appears to straddle the cold front. The Lihue sounding launched at 1115 UTC, records a surface pressure of approximately 3 mb greater than Kihei, after interpolating to 83 m (height of the Kihei site). Since Lihue is approximately 2° north and 3° west of Kihei, this post-cold front characteristic is expected. Associated with the approximate time of cold front crossing (and all the expected tightening of gradients), the r_0 sensor displays a 20+ mm drop (!) within the same time interval. At 1300 UTC, r_0 measurements indicate a 15 mm plunge in magnitude. The corresponding satellite image implies the passing of additional cloud lines associated with smaller fractions of the larger cold front during that time period. The 1446 UTC image displays the passing of the most extensive cloud cover associated with the cold front in the comma cloud. By 1546 UTC (12 minutes prior to Kihei sonde launch 6), the site is bordering the area that is normally (in more northerly latitudes) associated with

the dry tongue, "a protrusion of relatively dry air into a region of higher moisture content" (Huschke, 1970). In this sector, one expects cold advection and sinking air.

The 1558 UTC Kihei rawinsonde launch records the following surface parameters:

P (Pressure) = 1006.6 mb
T (Temperature) = 18.0° C
RH (Relative Humidity) = 86%
Wind Speed, Wind Direction = calm (< 2m/s), N/A
Stability = stable

A small inversion of 2.8° C over 57 m initials the profile. Winds remain light and variable throughout the first 5 km. Humidity measurements indicate a small peak of 72% at 0.561 km followed by two minor inversions. A second peak of 71% at 1.715 km precedes a small 0.5° C increase between 1.768-1.815 km. A third humidity maximum of 62% is recorded at 3.159 km with yet another maximum of 69% at 7.658 km. The highest humidity measurement (apart from the surface) occurs at 9.307 km (73%), with a second strong influx of humidity at 10.151 km (72%). This moist layer immediately precedes a westerly jet stream (10.964-13.037 km). Unlike the former soundings, this jet's maximum wind speed is 38.6 m/s. The temperature gradient across the jet stream is -13.6° C/2.138 km (-6.361° C/km). Winds remain out of the western quadrants well past the initial signature of the tropopause (17 km). Not until 20 km, do the winds suddenly become light and variable.

4. 0500-1730 UTC 30 April 1988

The 0544 UTC Kihei launch surface parameters include:

P (Pressure) = 1007.9 mb
T (Temperature) = 23.3° C
RH (Relative Humidity) = 79%
Wind Speed, Wind Direction = light, W
Stability = stable

Surface stability is defined by a 0.5° C inversion in the first 6 m of the profile. An intermittent layer of stratus begins at 2.082 km (96% RH). A second stable layer marked by a 1.3° C increase in temperature over 0.379 km (3.430° C/km) caps the moist layer. By 2.687 km the winds pick up and veer from the NW to SE. The second of three peaks in the humidity is recorded at 7.113 km (84% RH). The third humidity maximum at 8.982 km (75%) immediately follows a layer of strong winds (33.8 m/s) from the SW. A weak 0.6° C/0.101 km (5.941° C/km) inversion ties this layer's structure together. A slow westerly jet stream (max wind speed of 36.8k m/s at 12.972-13.021 km) occurs be-

tween 12.716 km and 13.228 km. This is supported by a $-2.2^{\circ}\text{C}/0.512\text{ km}$ ($-4.297^{\circ}\text{C}/\text{km}$) temperature gradient. Despite a decrease in wind speed with height, winds remain W,SW up through 18 km. Around the height of the tropopause (20.5 km) winds back into the eastern quadrants where they remain until the sampling is terminated (23.975 km).

Consulting the 1115 UTC Lihue sounding, as well as the 1146 UTC satellite image, the overall structure of the comma cloud is now fragmented. Low level clouds are intermittently dispersed around the Hawaiian Islands. A moist layer between 1-2.1 km is implied from Lihue's sounding. Surface winds are moderate to light and from the east until about 6 km where they veer and increase in magnitude. The maximum velocity recorded, however, is 34.0 m/s from the west (12.536 km). This is hardly the strength of the system just monitored less than 48 hours ago. The r_0 measurements reflect this lack of gross turbulence with an increase from 45 mm to nearly 70 mm sampled over the same 5-6 hour time period.

The last Kihei rawinsonde launch of the experiment (1434 UTC) records the following surface measurements:

P (Pressure) = 1007.4 mb
T (Temperature) = 18.0°C
RH (Relative Humidity) = 100%
Wind Speed, Wind Direction = light, NE
Stability = stable

The vertical profile begins with a 3.4°C inversion in the first 36 m. Surface humidity of 100% (a measurement confirmed by condensation on the telescope lenses) decreases 20% in the initial 0.312 km. The light NE surface winds back to light W,SW within 0.265 km of the surface. Humidity increases to a peak of 83% at 0.638 km, dips about 5%, then increases to 87% by 1.241 km. A 0.5°C increase occurs between 1.324-1.440 km ($4.310^{\circ}\text{C}/\text{km}$), followed by another inversion of 0.6°C between 2.315-2.464 km. Winds display an increasing trend until approximately 4.6 km (SW). At this same level, humidity plunges to values of less than 10%. The westerly jet stream is nestled between 12.060-13.196 km carrying a peak velocity of 37.9 m/s between 12.444-12.521 km. The tropopause occurs around 19.1 km.

5. 0600-1730 UTC 01 May 1988

Early evening r_0 data indicates intermittent cloud cover. The 0546 UTC satellite image displays cloud cover as a local event. The closest cyclone is NW of the site by approximately 10° latitude (1100 km). The storm system that traveled through the area

earlier in the week has dissolved into the high pressure ridge NE of Hawaii. The two available soundings (Hilo and Lihue) launched at 1100 UTC and 1115 UTC, respectively, correspond to relatively high r_0 measurements (80 mm). Both rawinsonde soundings indicate an absence of surface inversion. Dewpoint depression minimums (no RH is recorded in these two rawinsonde datasets) occur between 0.4 and 1.6 km implying a moist layer within this 1.2 km region. Super-adiabatic laypse rates are noted between surface-1000 mb ($12.327^\circ \text{ C/km}$) at Lihue, and 709-704 mb ($46.867^\circ \text{ C/km}$) at Hilo. Because there is no consistent level for these extremely large lapse rates, they are most likely locally induced. Winds below 4 km are generally from the eastern quadrants (Lihue's easterly winds extend to 5 km). Above this level, wind speed strengthens and wind direction is from the west. Jet stream velocities are recorded as W, NW between 11.792-13.922 km over Hilo, and W,SW between 10.645-14.672 km over Lihue. Maximum wind speeds of 42.8 m/s at 11.785 km (Hilo) and 39.2 m/s at 12.016 km (Lihue) are recorded. Both sites measure a lapse rate of -6.7° C/km across the jet. The two soundings also concur that the tropopasue caps the jet's subsiding winds at approximately 17.3 km.

r_0 measurements record a gradual 30 mm decrease between 1200-1300 UTC. The only available resource over that time interval is satellite images. Apart from an apparent increase in local cloud cover, there is no glaring evidence of turbulent sources. A review of 1988 May 2 reveals the development of another comma cloud structure west of Hawaii. Perhaps the sudden drop in r_0 (turbulence increase) is a results of the over-running (warm advection) often associated with the NE sector of this synoptic scale event.

APPENDIX E. MAUI, HAWAII - JULY 1988

A. METEOROLOGICAL DATA

Appendix E includes profiles from the July 1988 Kihei, Maui rawinsonde dataset. A Vaisala DigiCORA MW 11 rawinsonde system was used as the data acquisition system. Launch site for this session was located at 20.75° latitude, 156.43° longitude. The initial 2 km were sampled every two seconds (8-10 m). Above 2 km, the sampling rate was once every ten seconds (40-45 m). Flight number and launch times are provided in Table 11.

Table 11. JULY 1988 KIHAI, MAUI RAWINSONDE LAUNCHES

FLIGHT NO.	TIME (UTC)	DATE (DAY MON YR)
1	0703	7 July 1988
2	1537	7 July 1988
3	0536	8 July 1988
4	1612	8 July 1988
5	0605	9 July 1988
6	1527	9 July 1988
7	0556	10 July 1988
8	1532	10 July 1988
9	0550	11 July 1988
10	0926	11 July 1988

July 88 - Flight 1

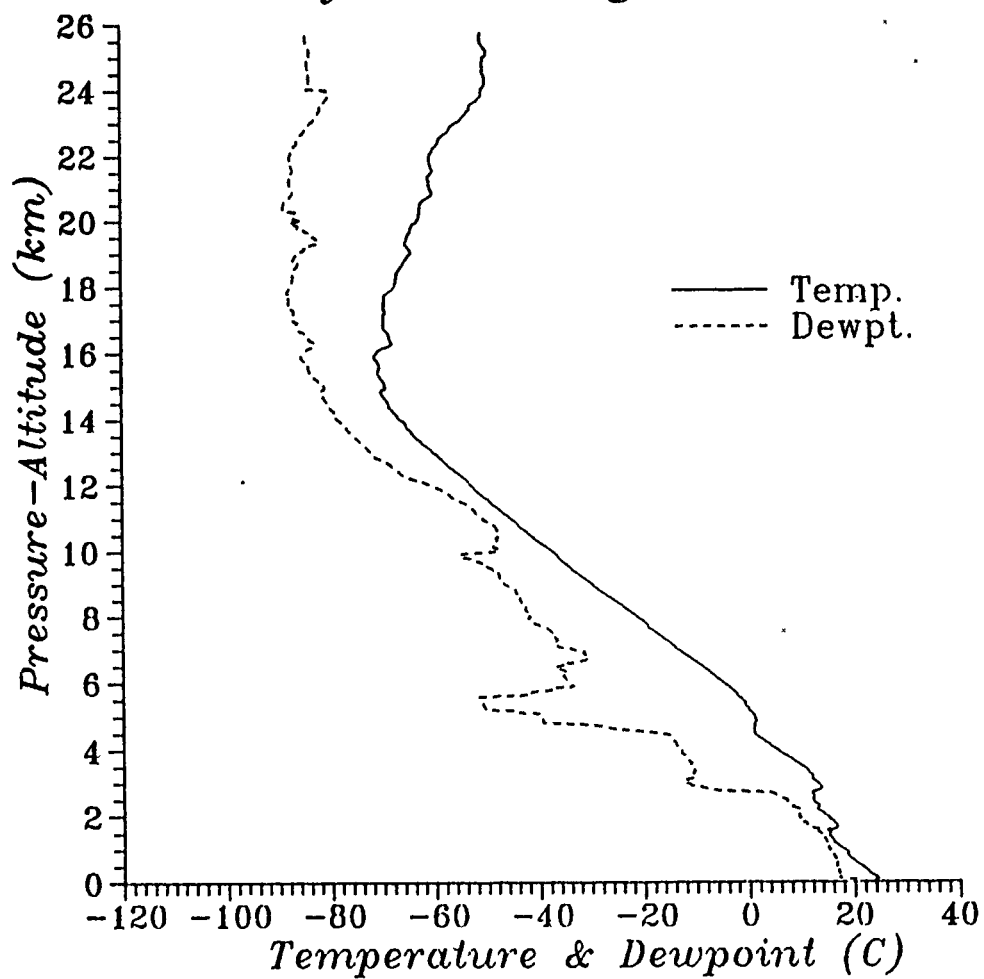


Fig. 62. Kihei, Maui Rawinsonde Data: 0703 UTC 7 July 1988

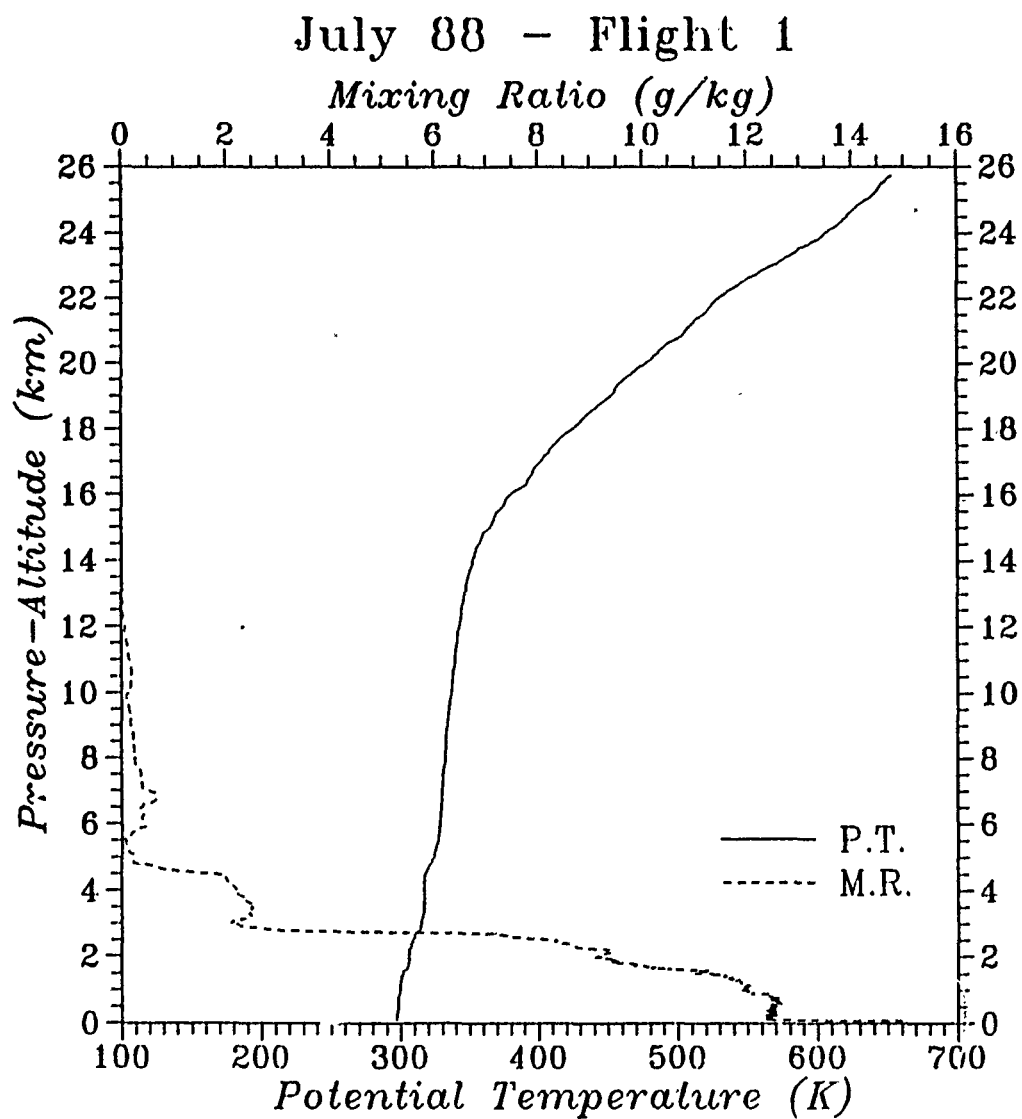


Fig. 63. Kilauea, Maui Rawinsonde Data: 0703 UTC 7 July 1988

July 88 - Flight 1

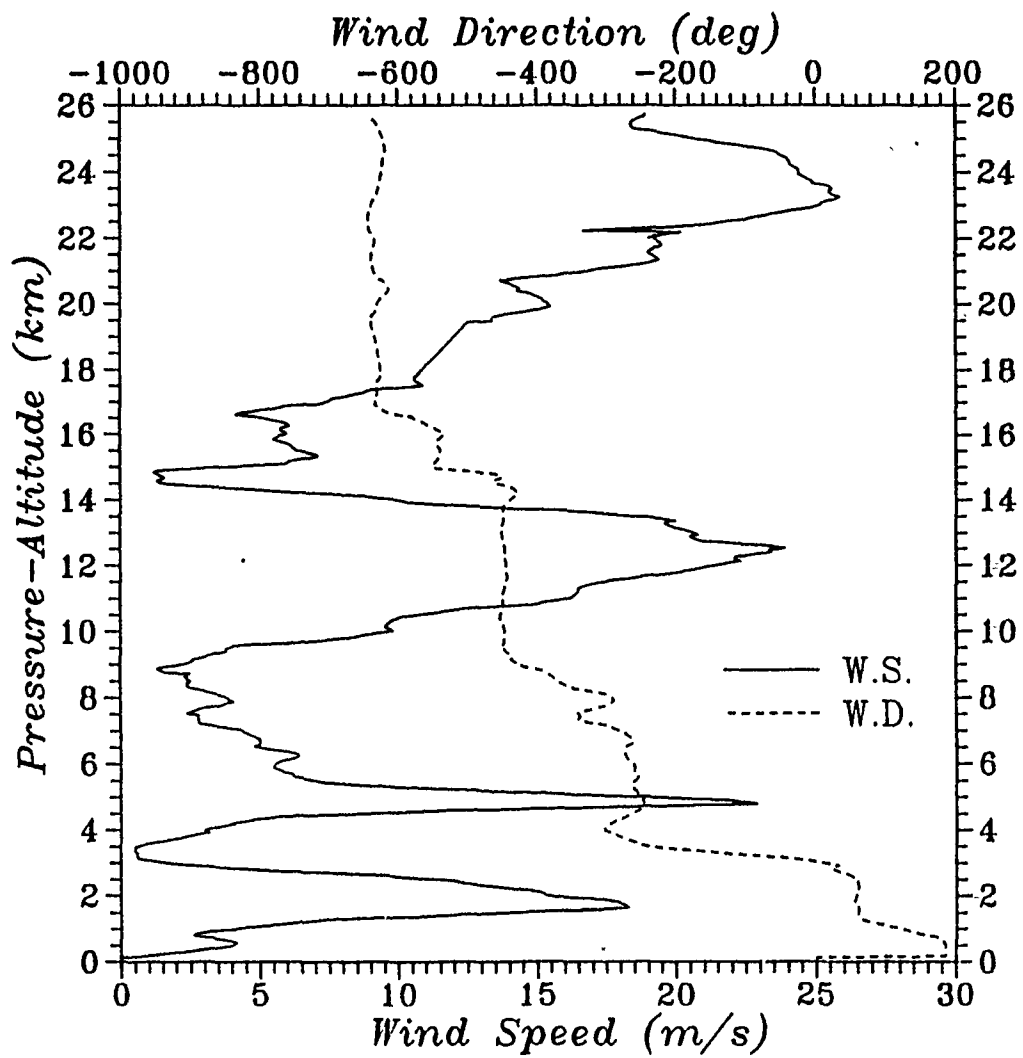


Fig. 64. Kihei, Maui Rawinsonde Data: 0703 UTC 7 July 1988

July 88 - Flight 2

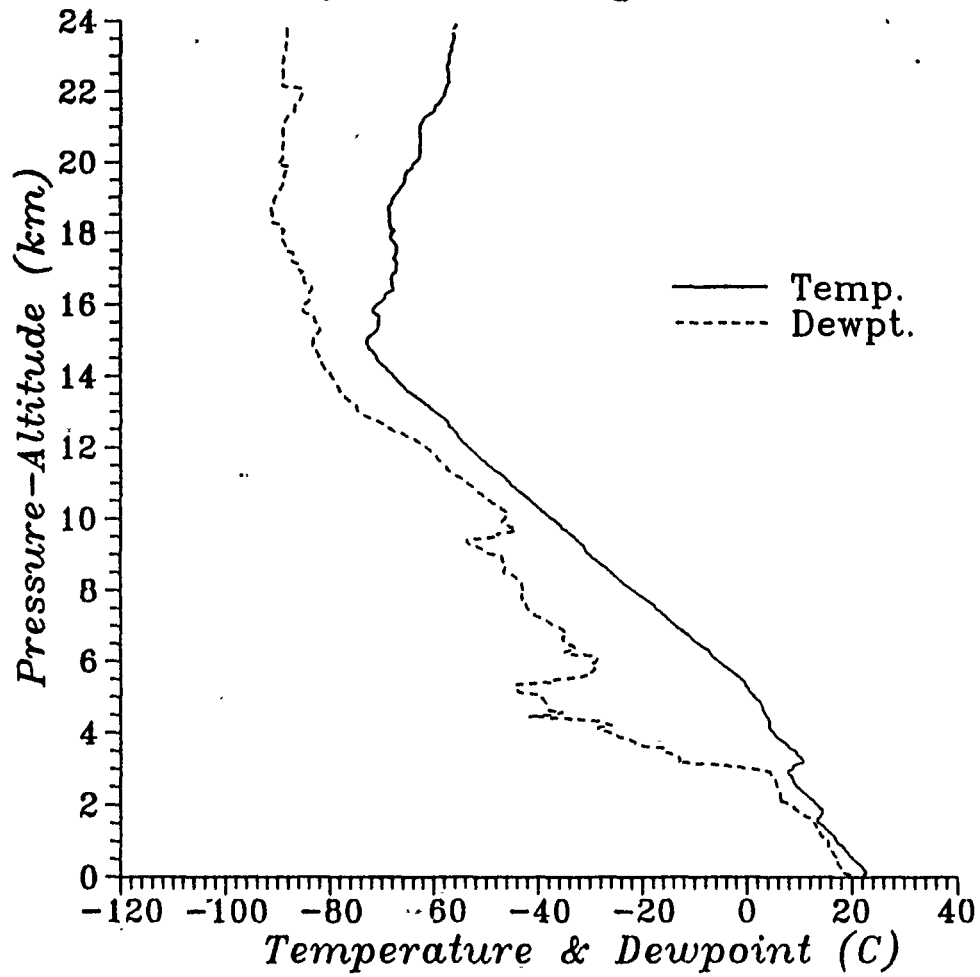


Fig. 65. Kihel, Maui Rawinsonde Data: 1537 UTC 7 July 1988

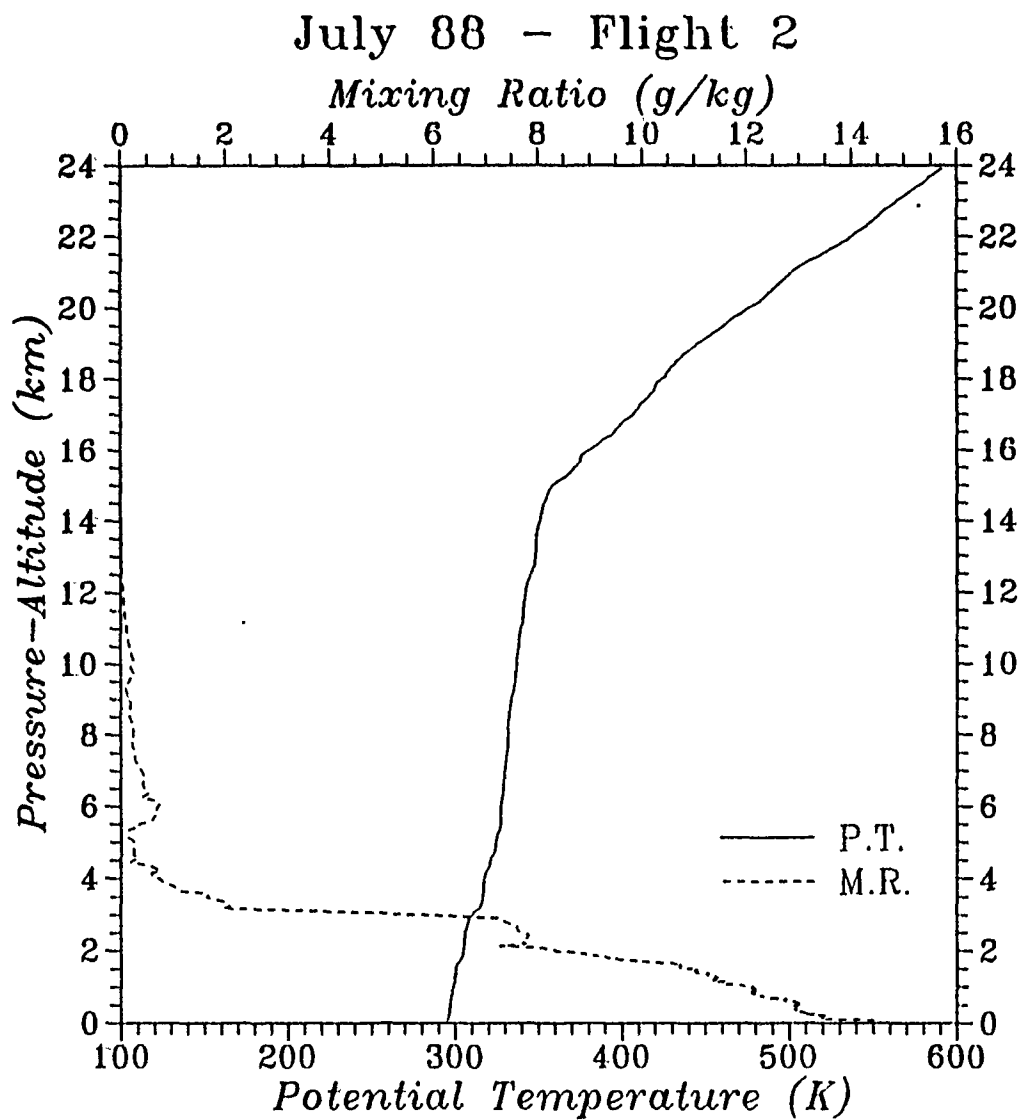


Fig. 66. Kīhei, Maui Rawinsonde Data: 1537 UTC 7 July 1988

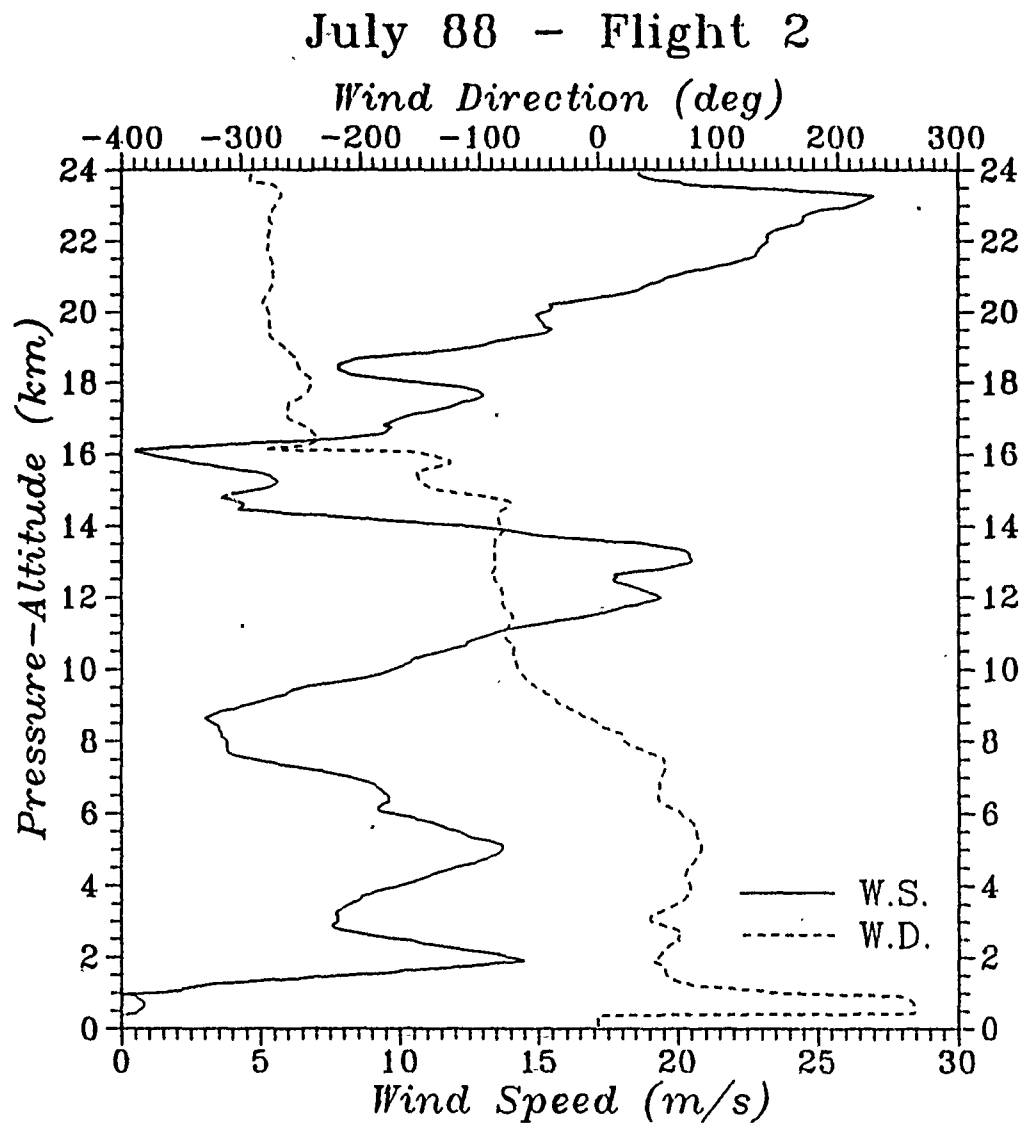


Fig. 67. Kihei, Maui Rawinsonde Data: 1537 UTC 7 July 1988

July 88 - Flight 3

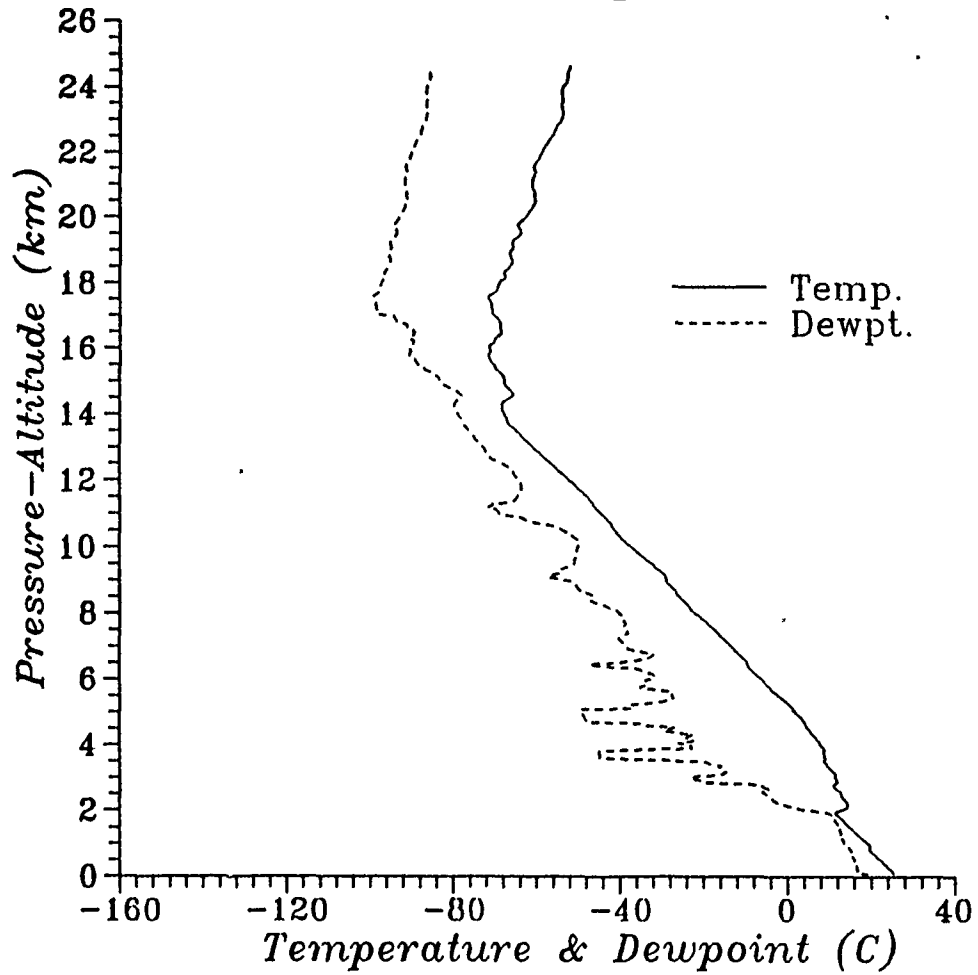


Fig. 68. Kihei, Maui Rawinsonde Data: 0536 UTC 8 July 1988

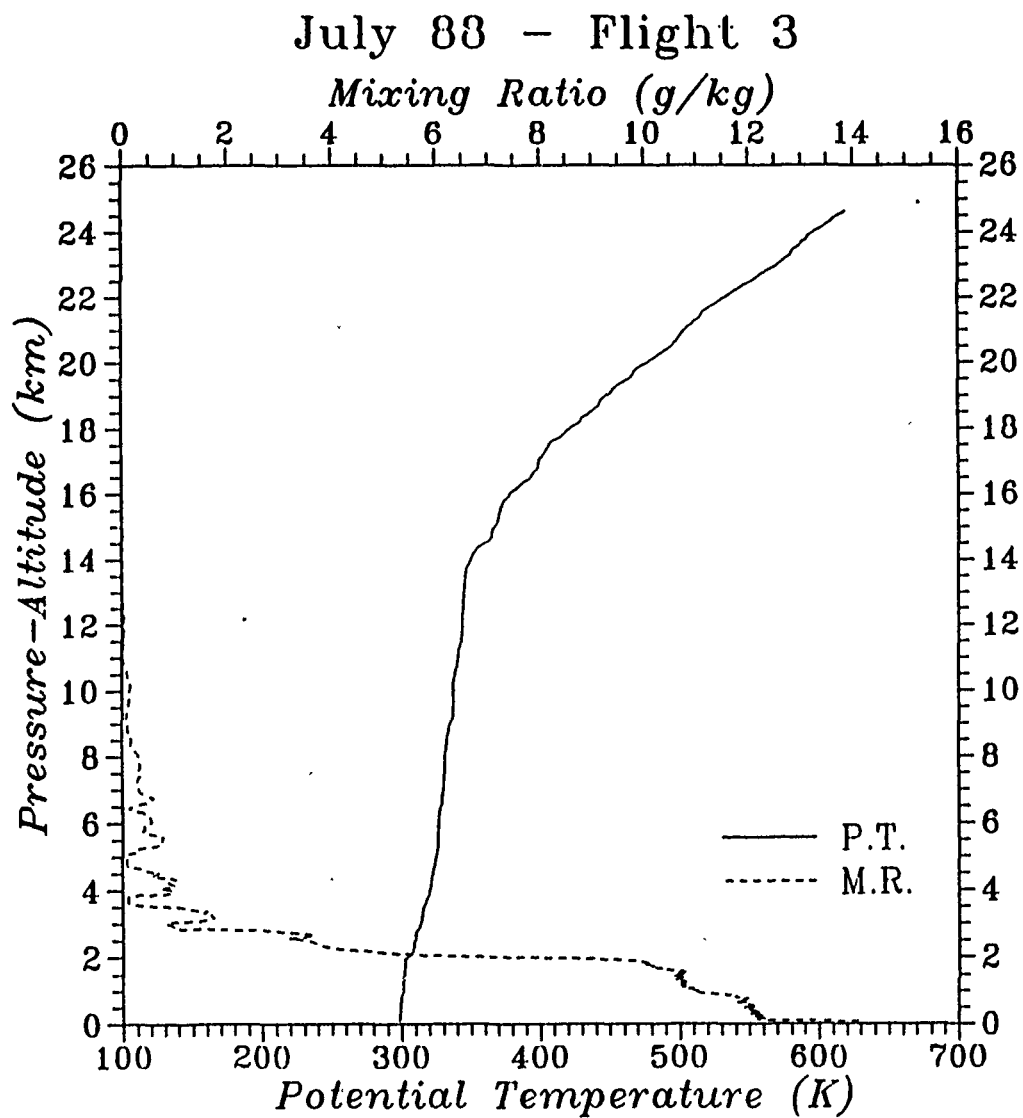


Fig. 69. Kihei, Maui Rawinsonde Data: 0536 UTC 8 July 1988

July 88 - Flight 3

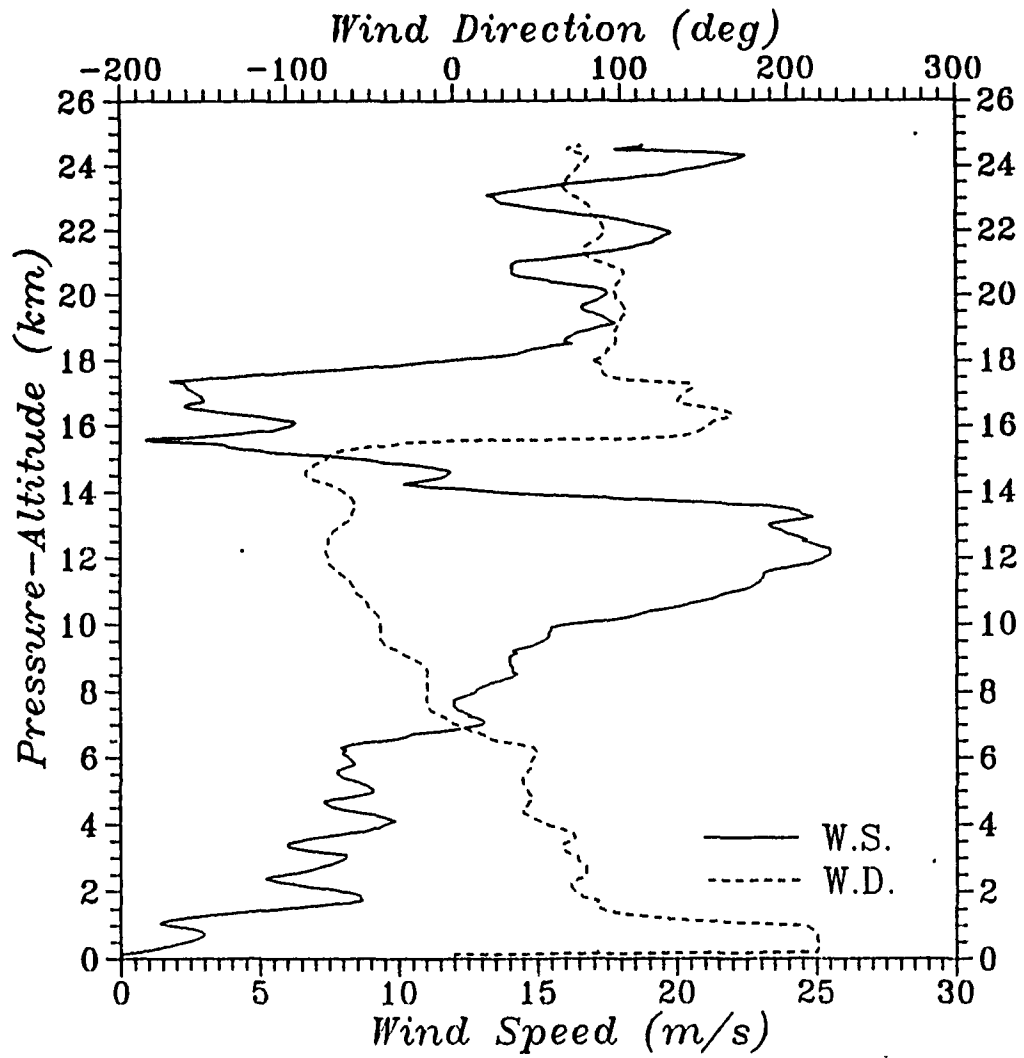


Fig. 70. Kihel, Maui Rawinsonde Data: 0536 UTC 8 July 1988

July 88 - Flight 4

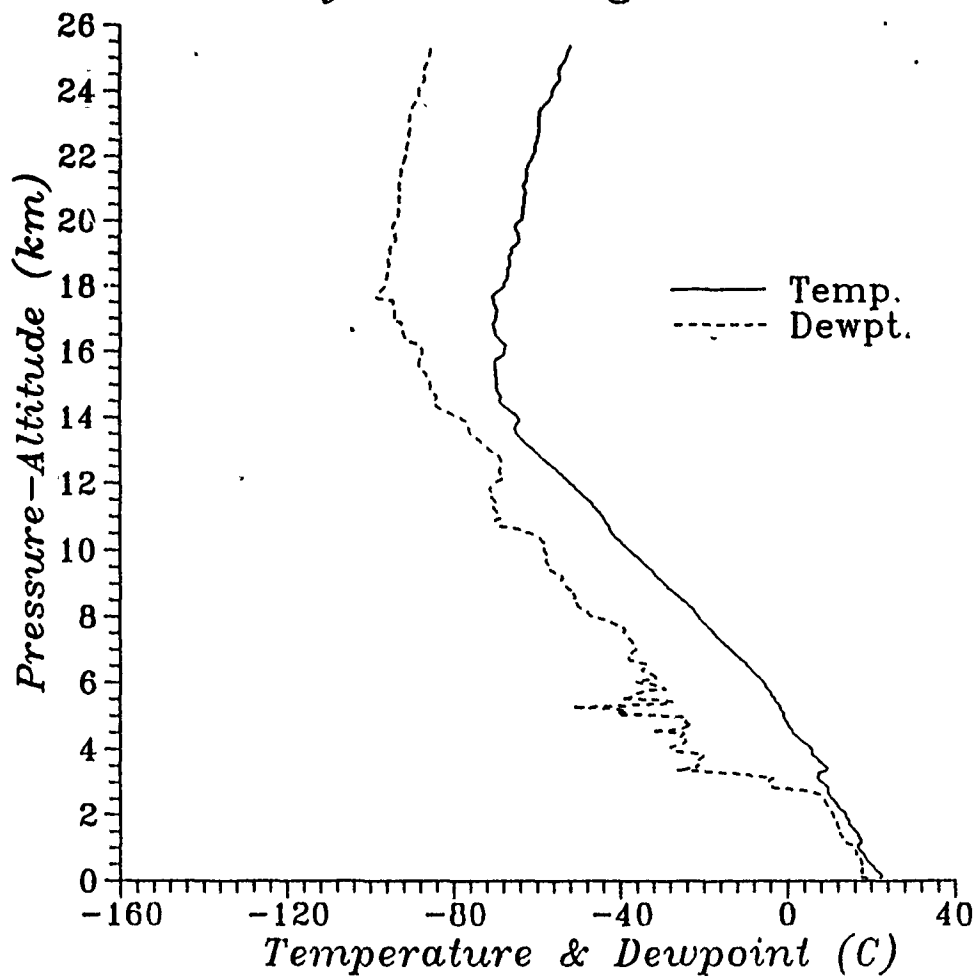


Fig. 71. Kihei, Maui Rawinsonde Data: 1612 UTC 8 July 1988

July 88 - Flight 4

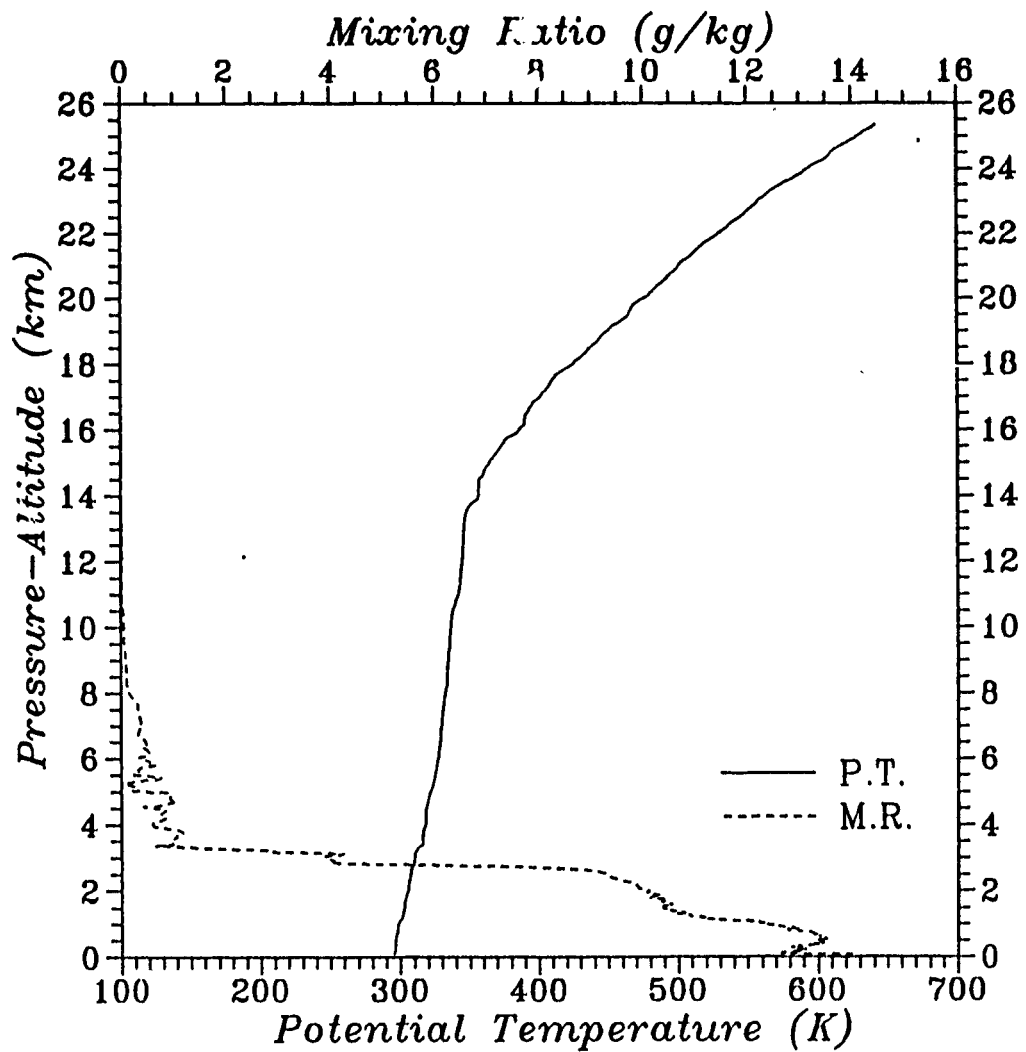


Fig. 72. Kihel, Maui Rawinsonde Data: 1612 UTC 8 July 1988

July 88 - Flight 4

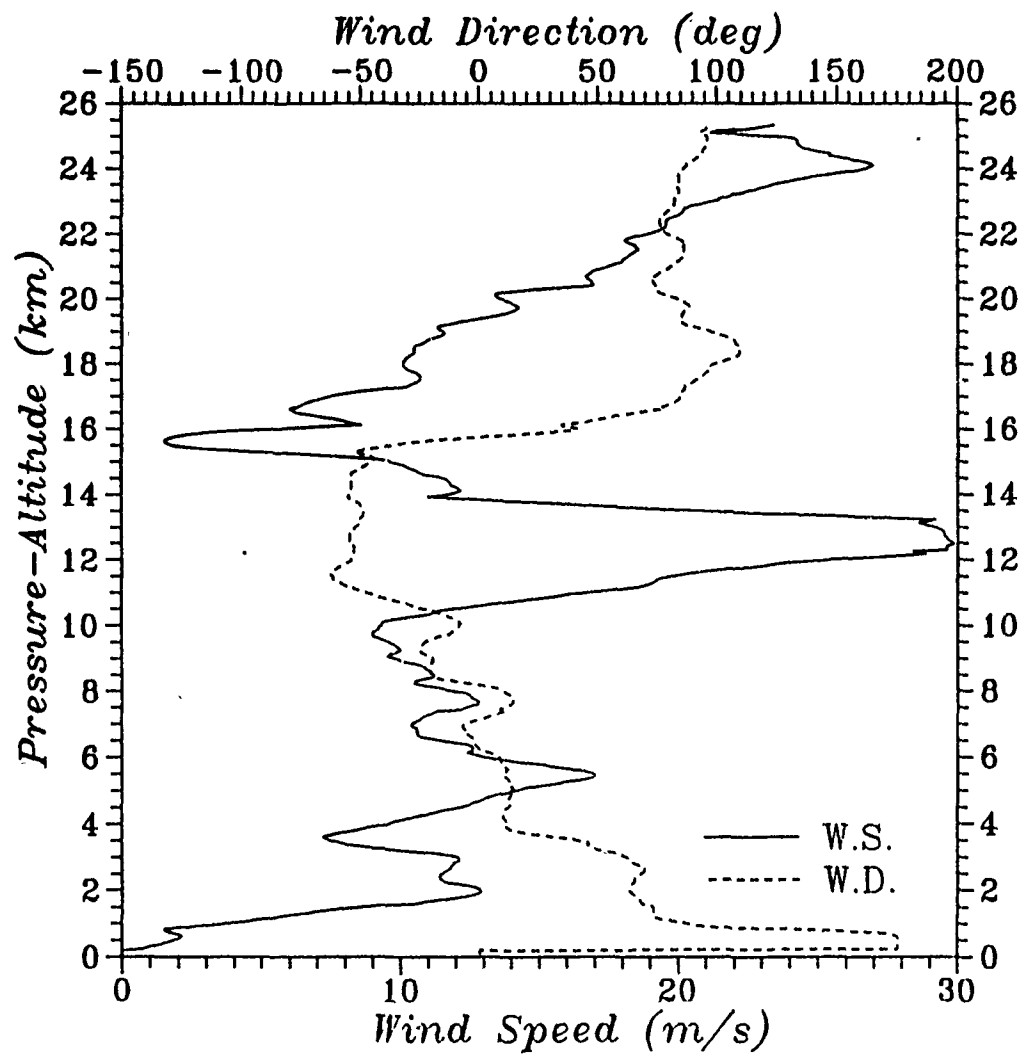


Fig. 73. Kilauea, Maui Rawinsonde Data: 1612 UTC 8 July 1988

July 88 - Flight 5

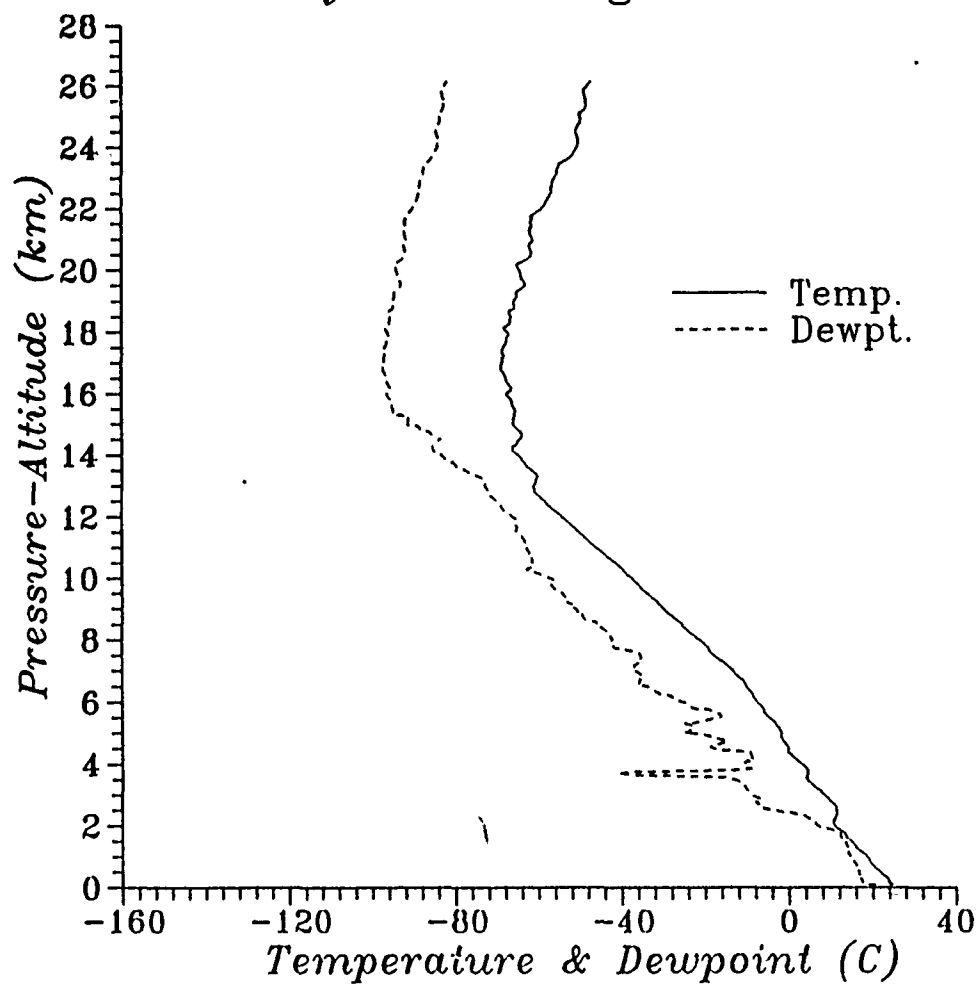


Fig. 74. Kihel, Maui Rawinsonde Data: 0605 UTC 9 July 1988

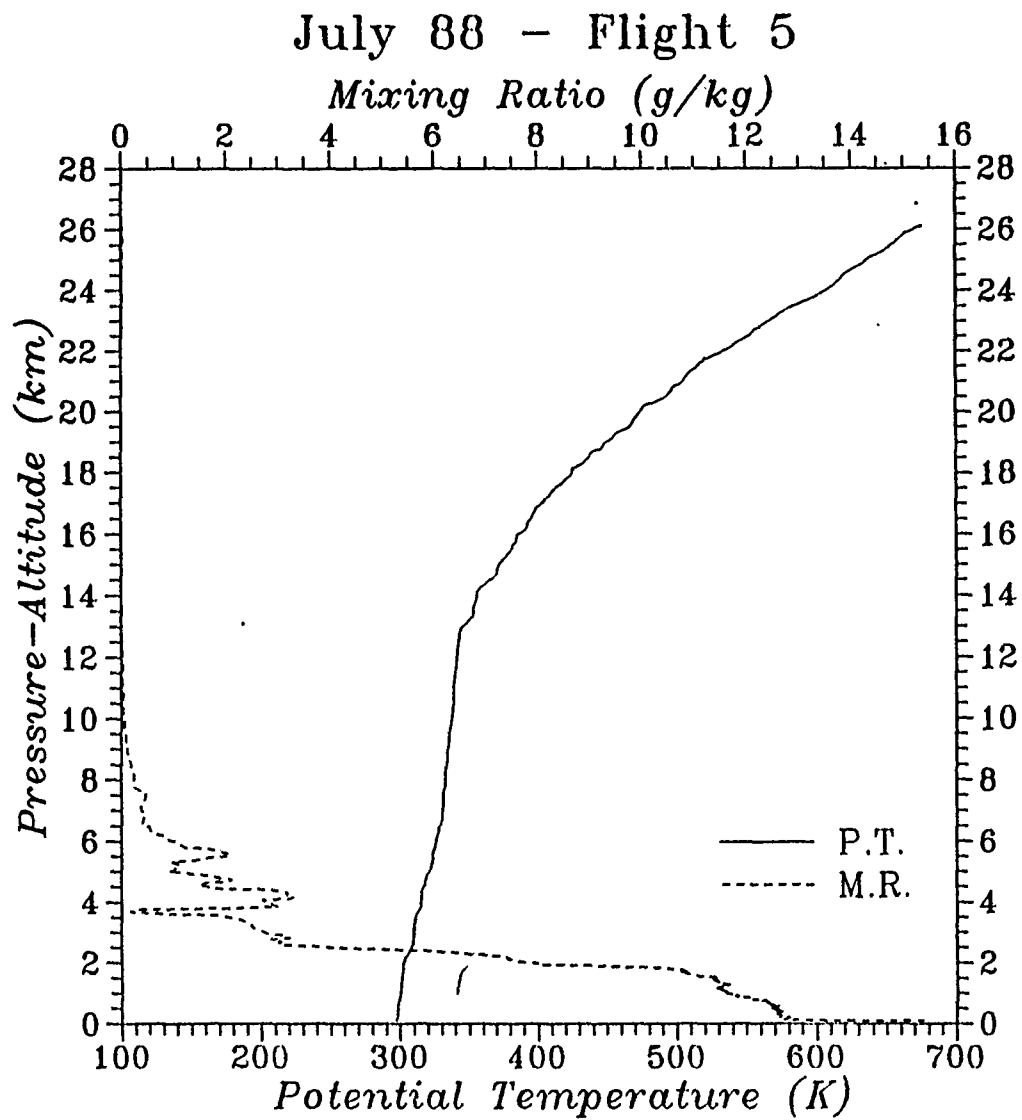


Fig. 75. Kihei, Maui Rawinsonde Data: 0605 UTC 9 July 1988

July 88 - Flight 5

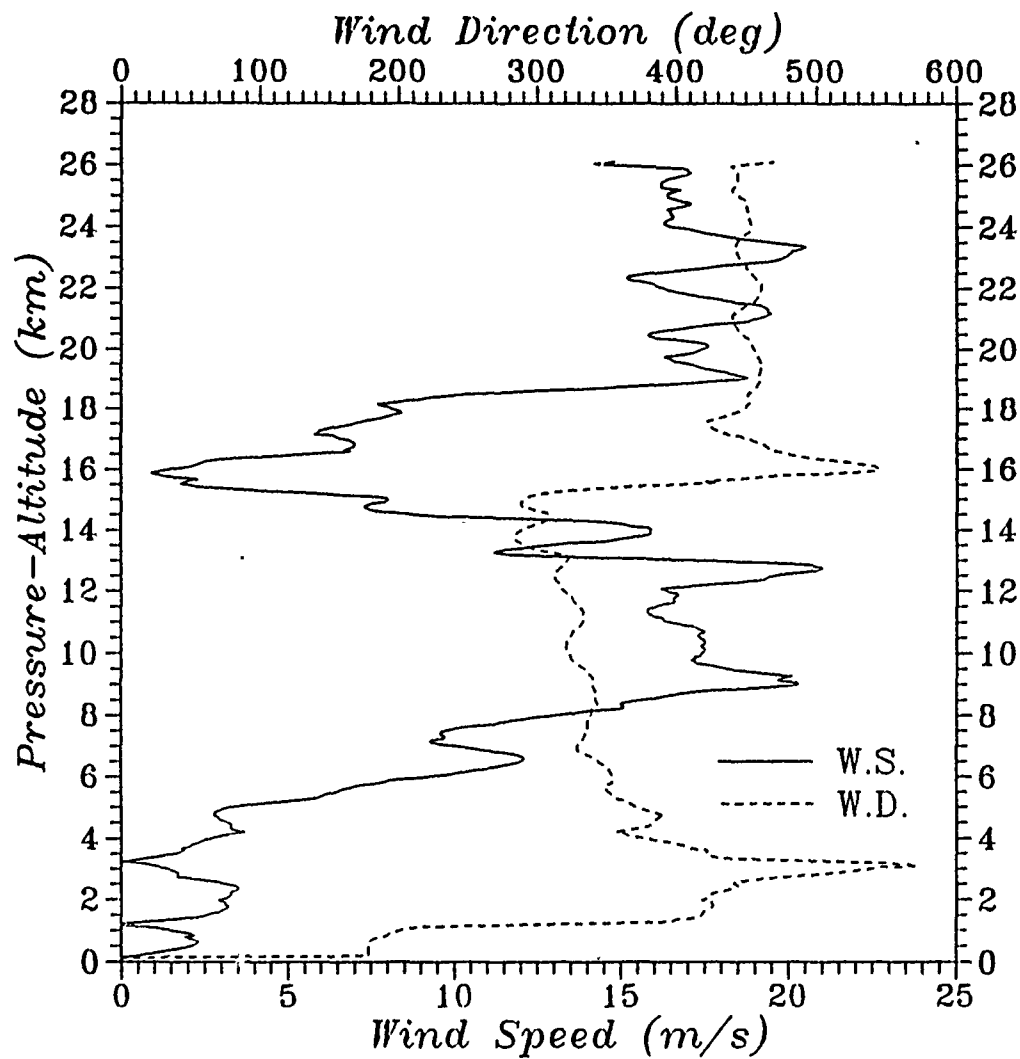


Fig. 76. Kihei, Maui Rawinsonde Data: 0605 UTC 9 July 1988

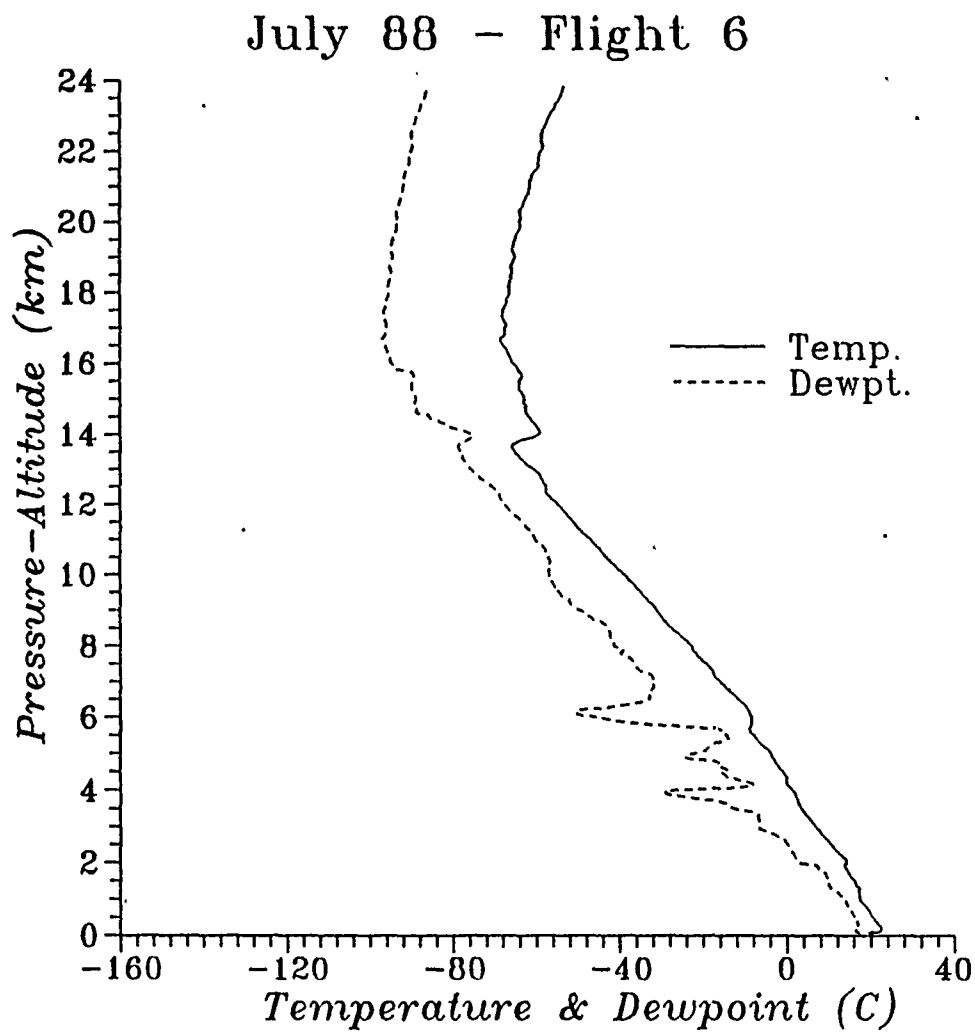


Fig. 77. Kilauea, Maui Rawinsonde Data: 1527 UTC 9 July 1988

July 88 - Flight 6

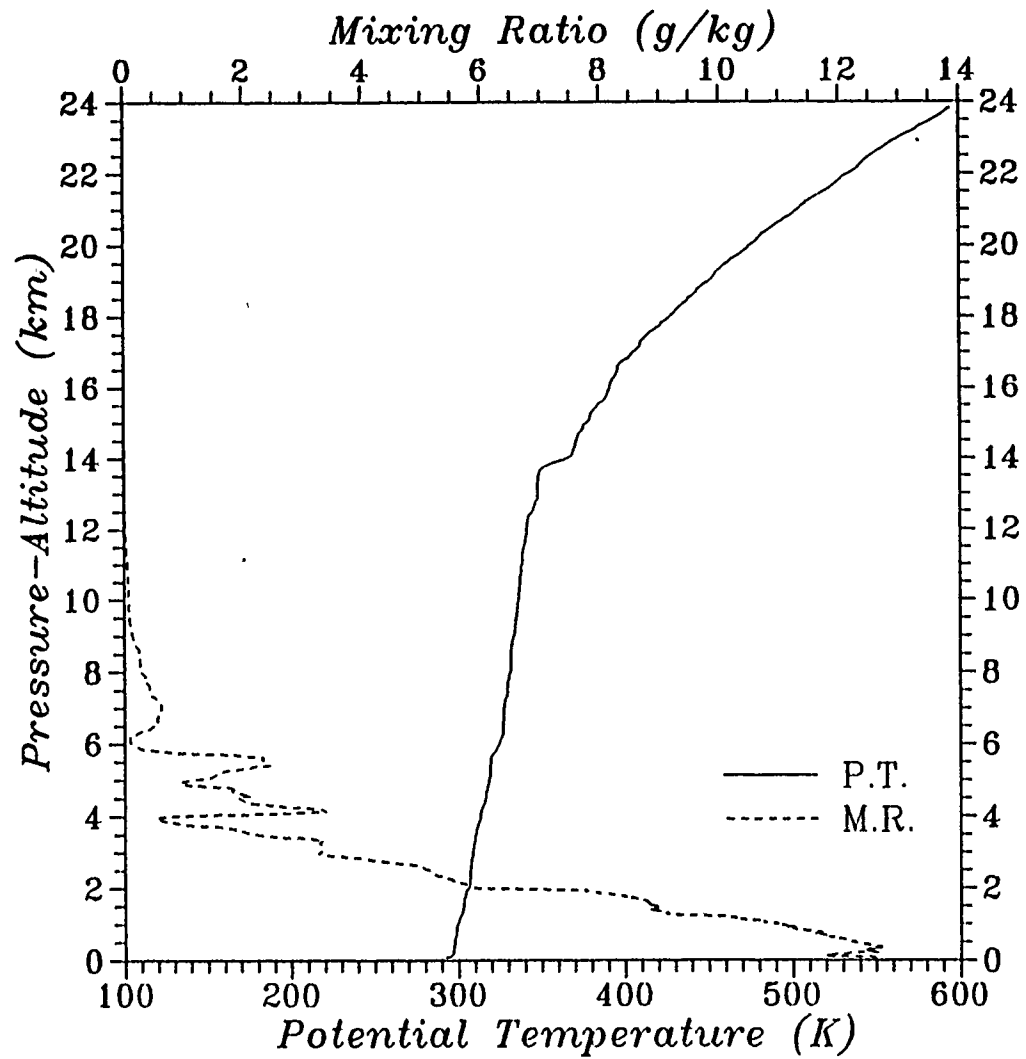


Fig. 78. Kihei, Maui Rawinsonde Data: 1527 UTC 9 July 1988

July 88 - Flight 6

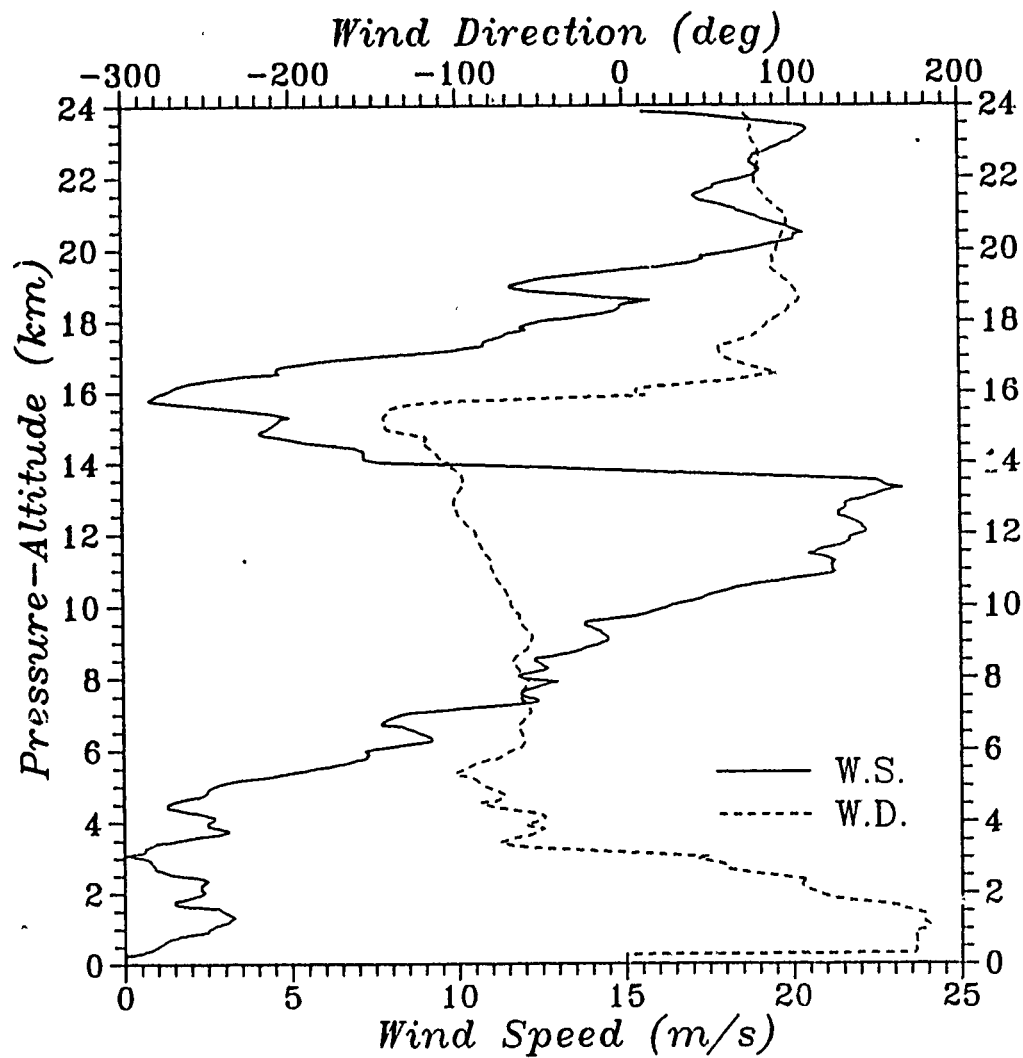


Fig. 79. Kilauea, Maui Rawinsonde Data: 1527 UTC 9 July 1988

July 88 - Flight 7

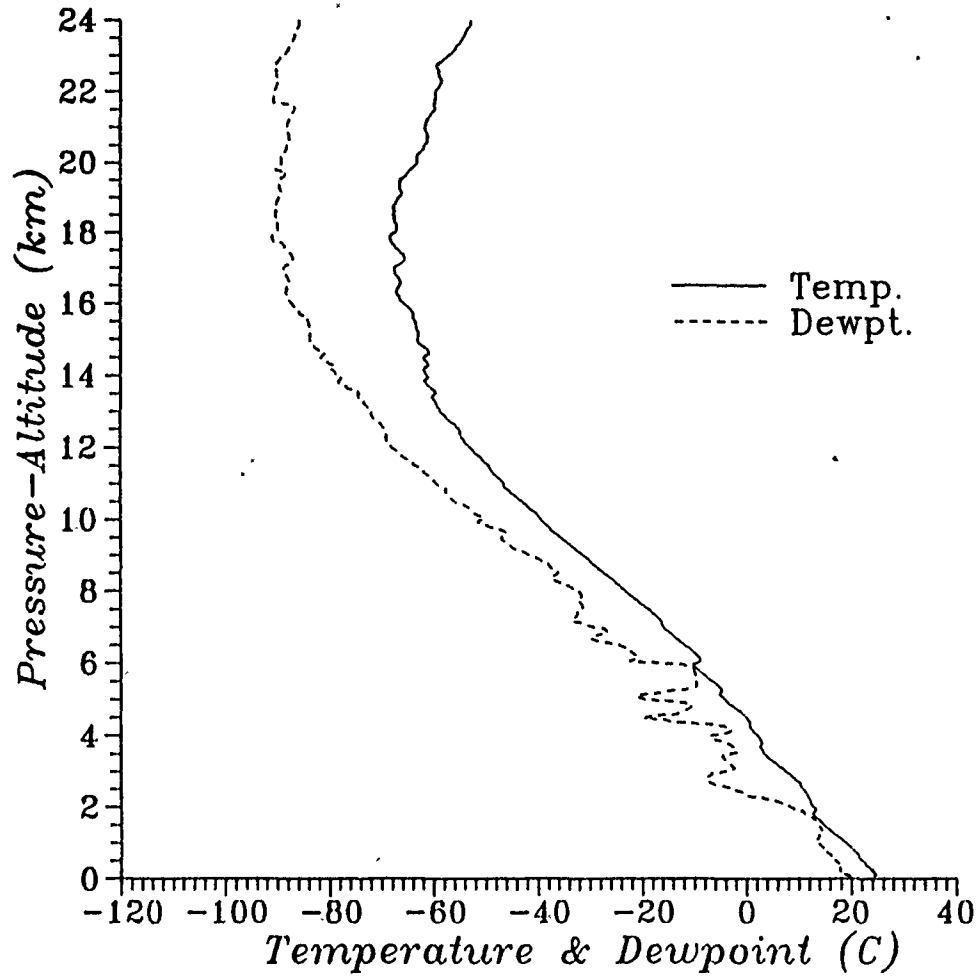


Fig. 80. Kilauea, Maui Rawinsonde Data: 0556 UTC 10 July 1988

July 88 - Flight 7

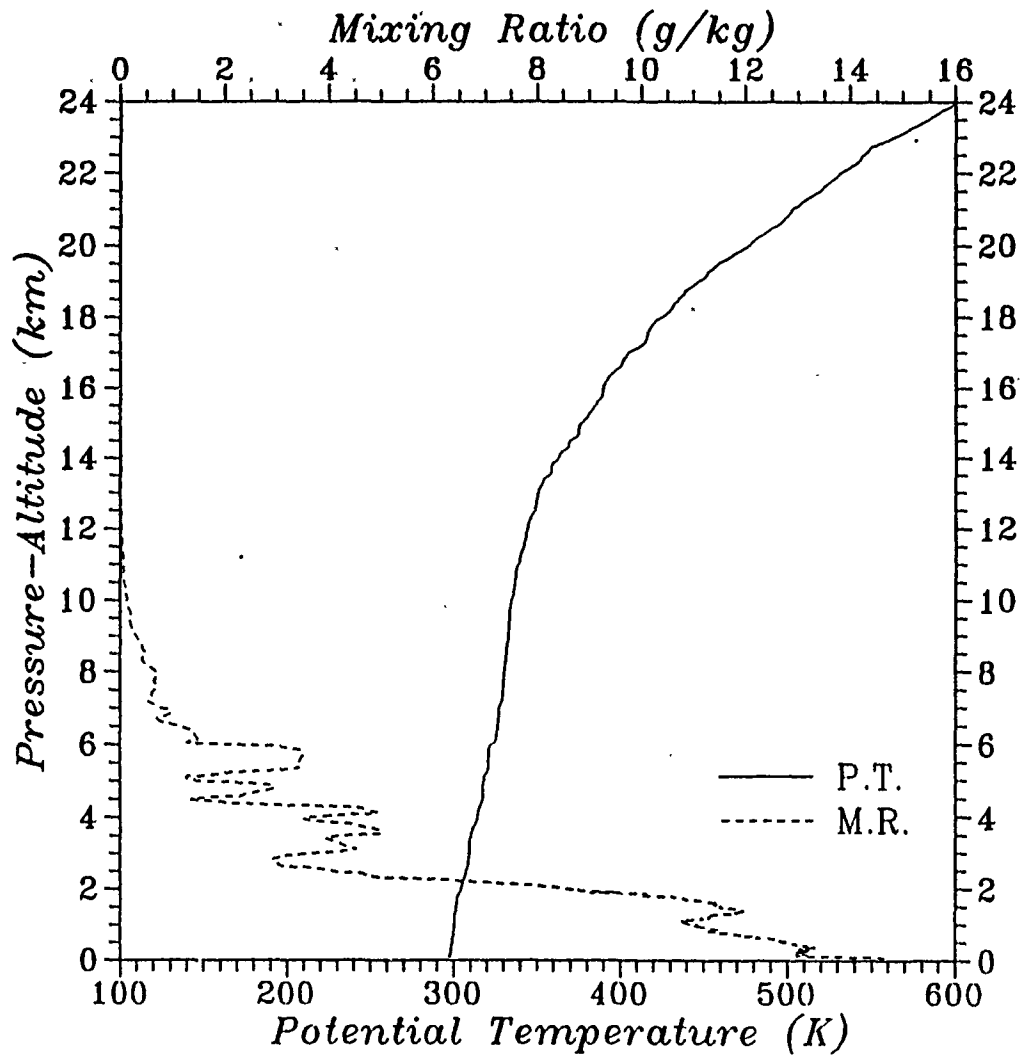


Fig. 81. Kihei, Maui Rawinsonde Data: 0556 UTC 10 July 1988

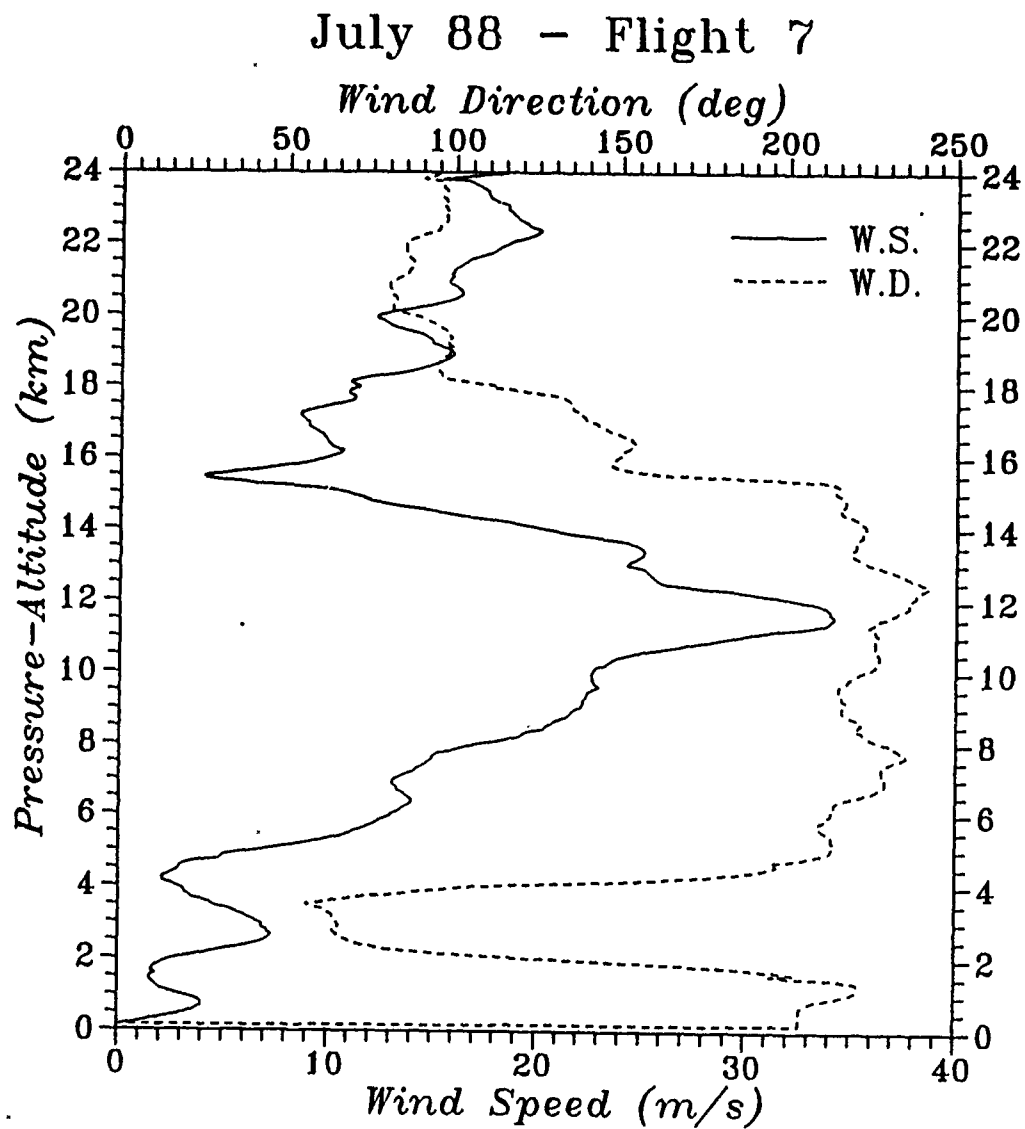


Fig. 82. Kīhei, Maui Rawinsonde Data: 0556 UTC 10 July 1988

July 88 - Flight 8

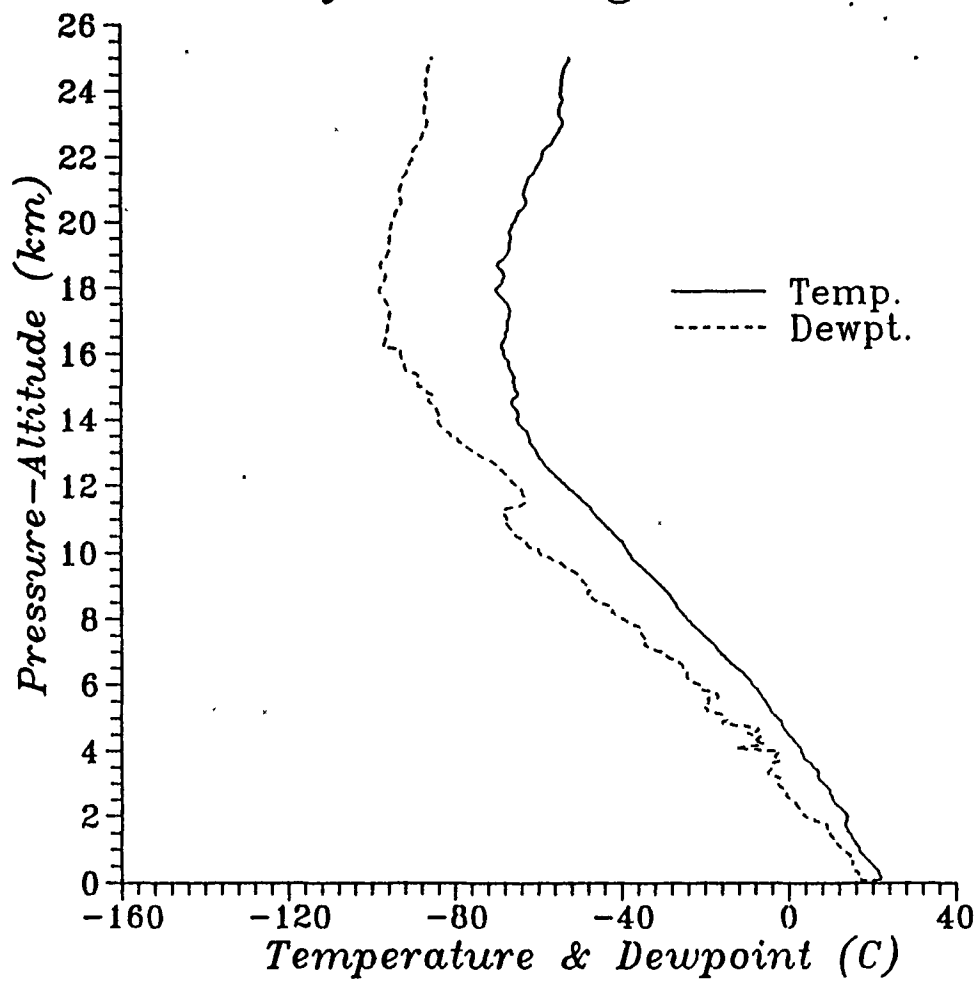


Fig. 83. Kihei, Maui Rawinsonde Data: 1532 UTC 10 July 1988

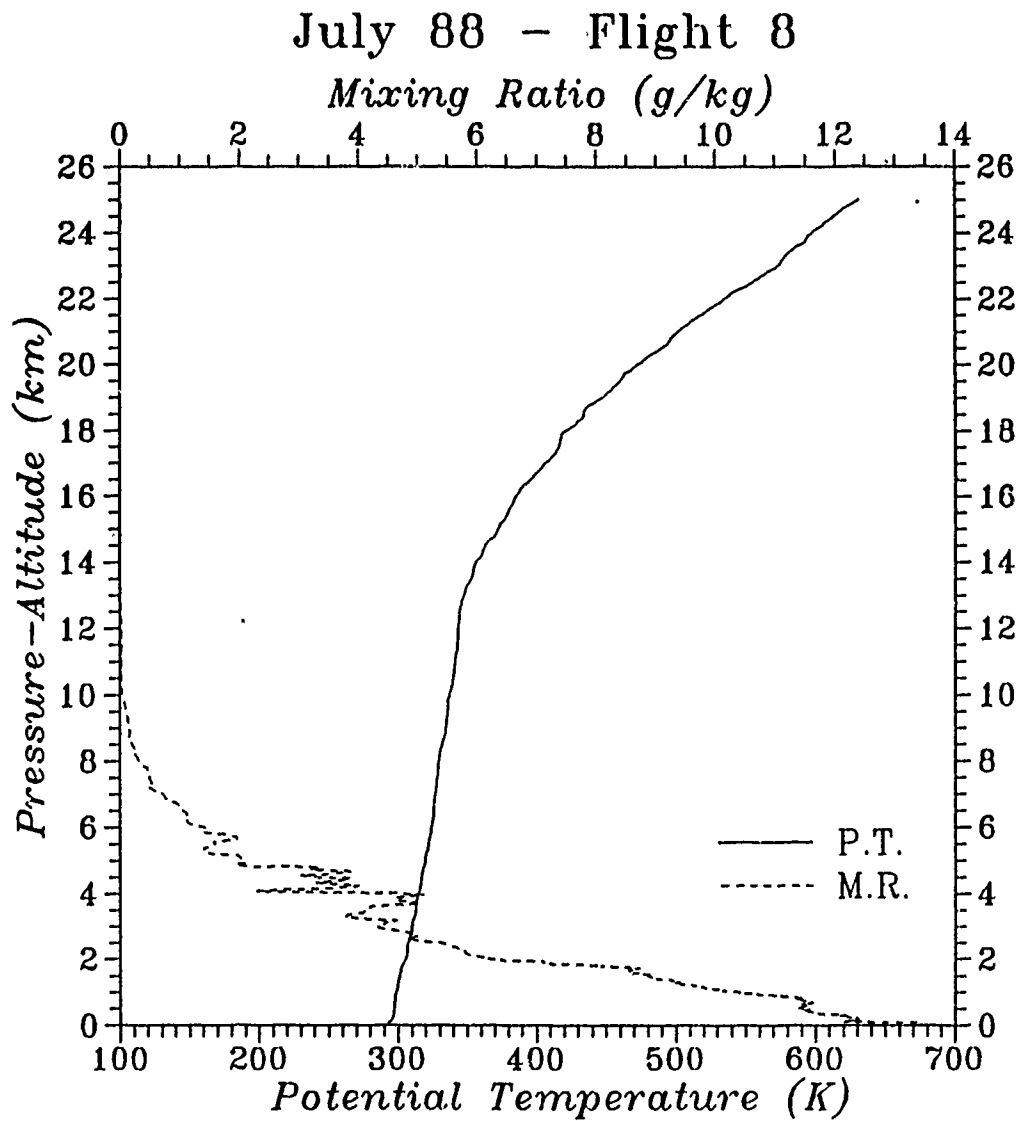


Fig. 84. Kihei, Maui Rawinsonde Data: 1532 UTC 10 July 1988

July 88 - Flight 8

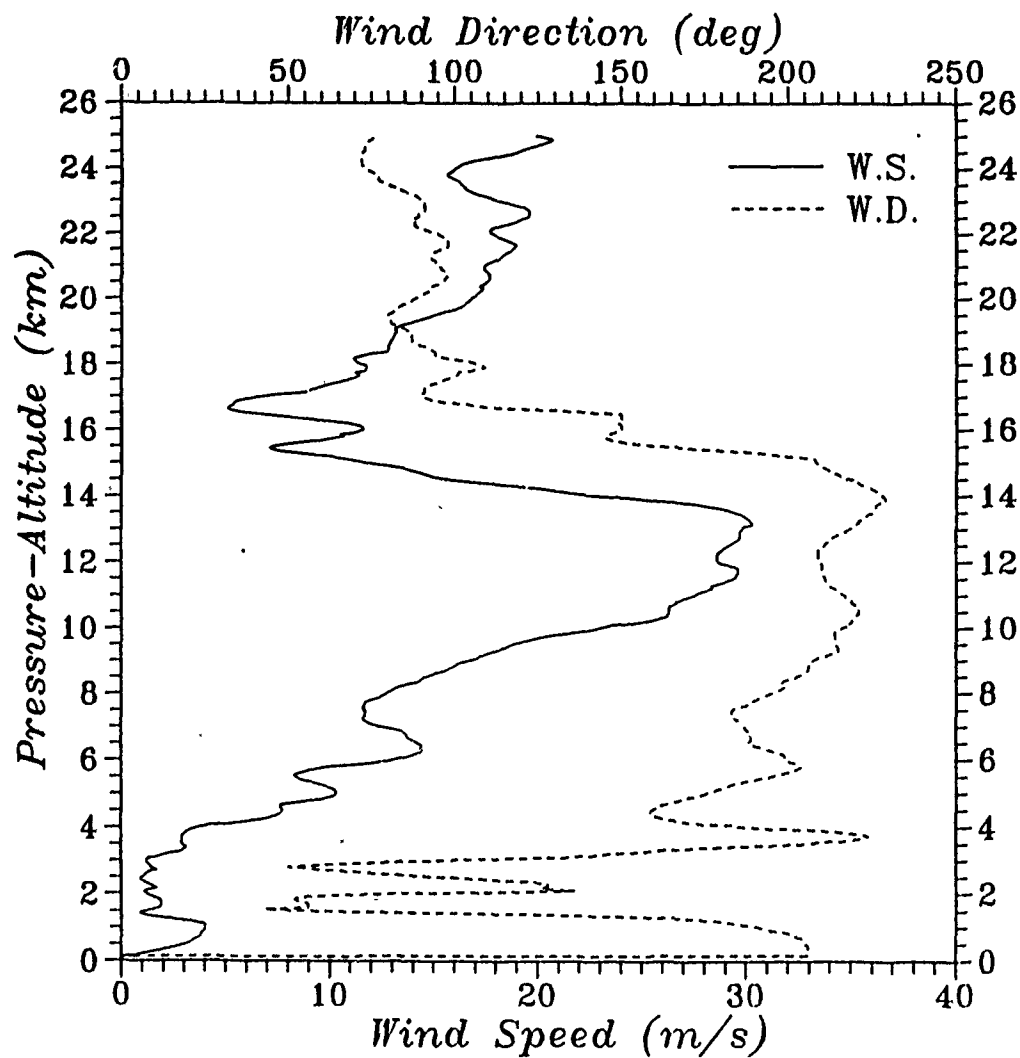


Fig. 85. Kihei, Maui Rawinsonde Data: 1532 UTC 10 July 1988

July 88 - Flight 9

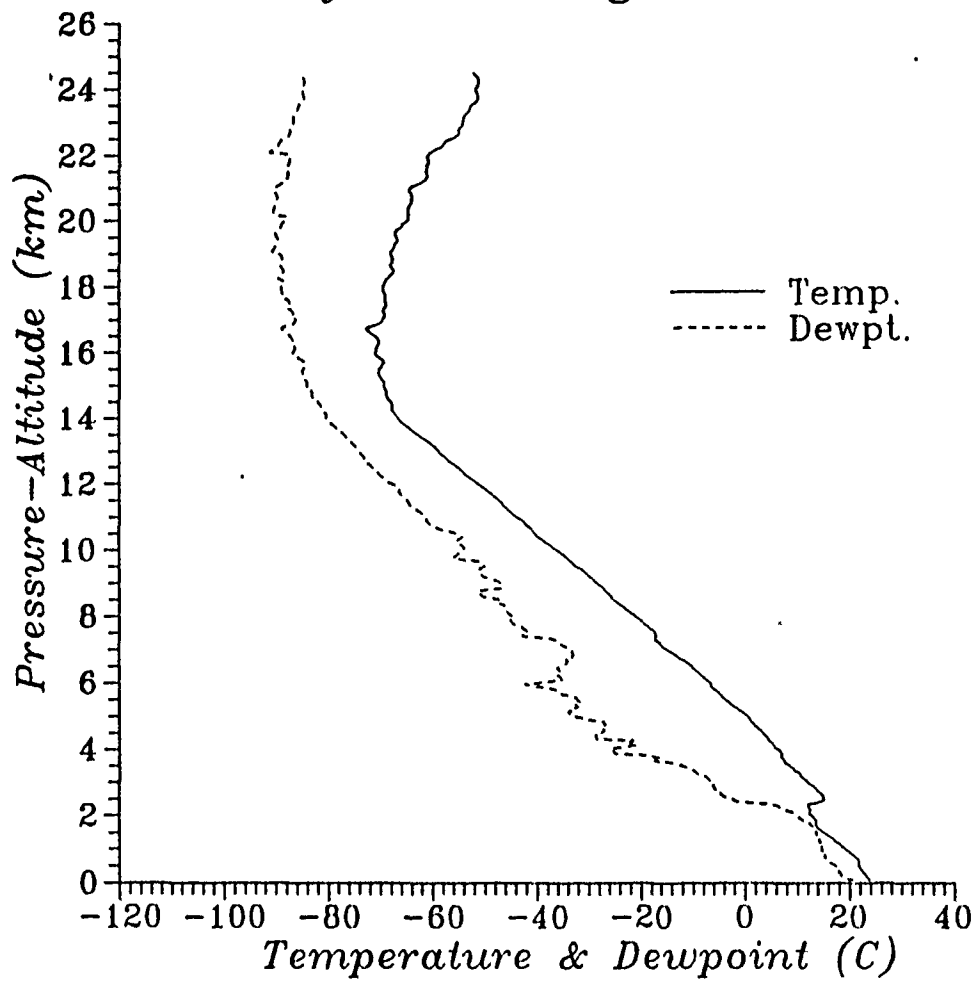


Fig. 86. Kihei, Maui Rawinsonde Data: 0550 UTC 11 July 1988

July 88 - Flight 9

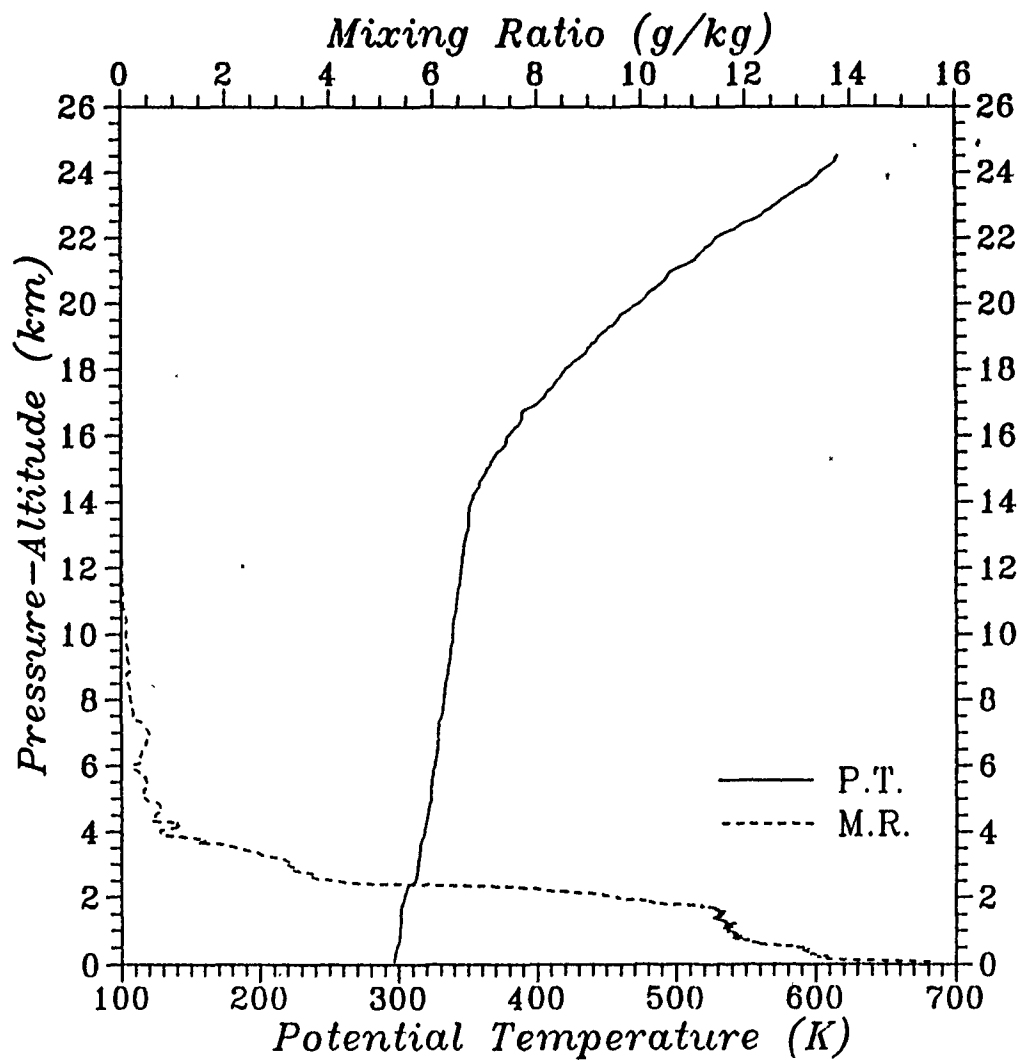


Fig. 87. Kīhei, Maui Rawinsonde Data: 0550 UTC 11 July 1988

July 88 - Flight 9

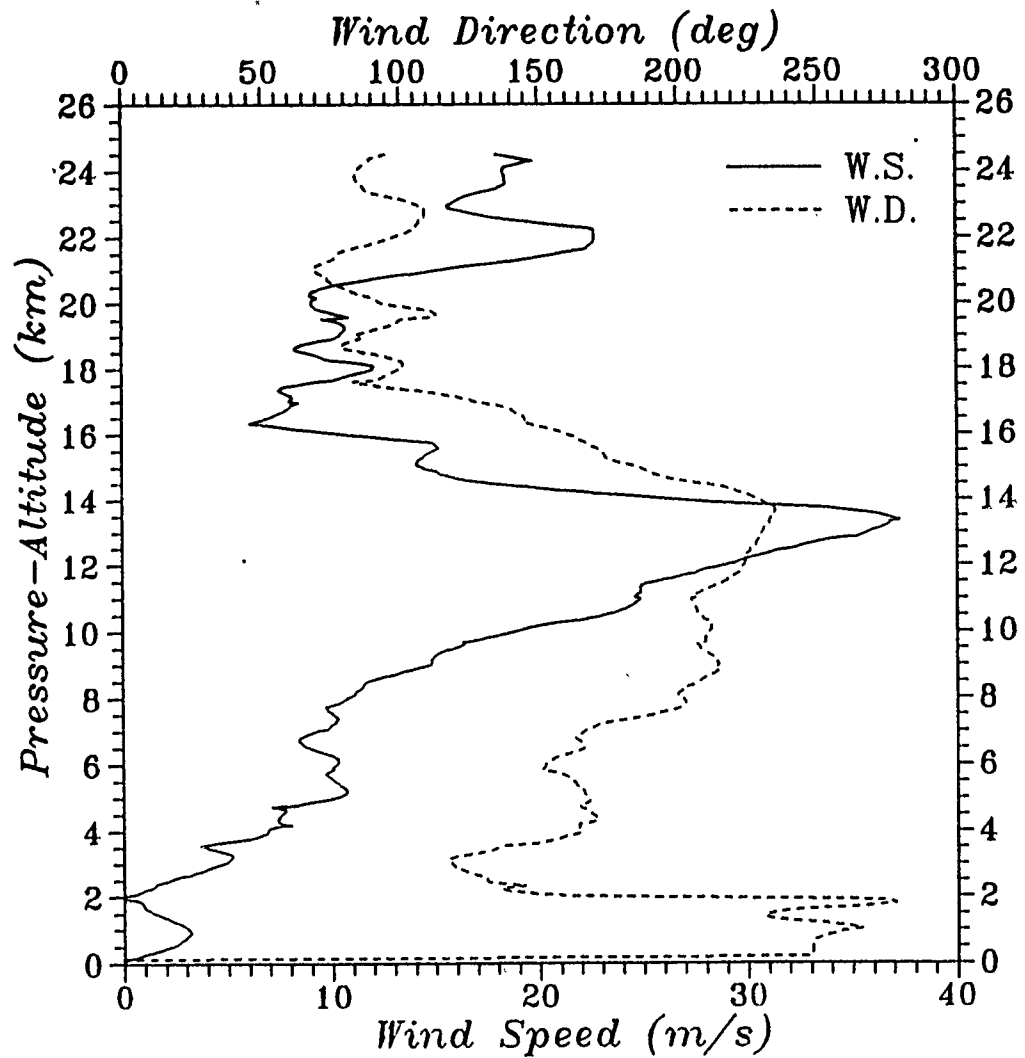


Fig. 88. Kilauea, Maui Rawinsonde Data: 0550 UTC 11 July 1988

July 88 - Flight 10

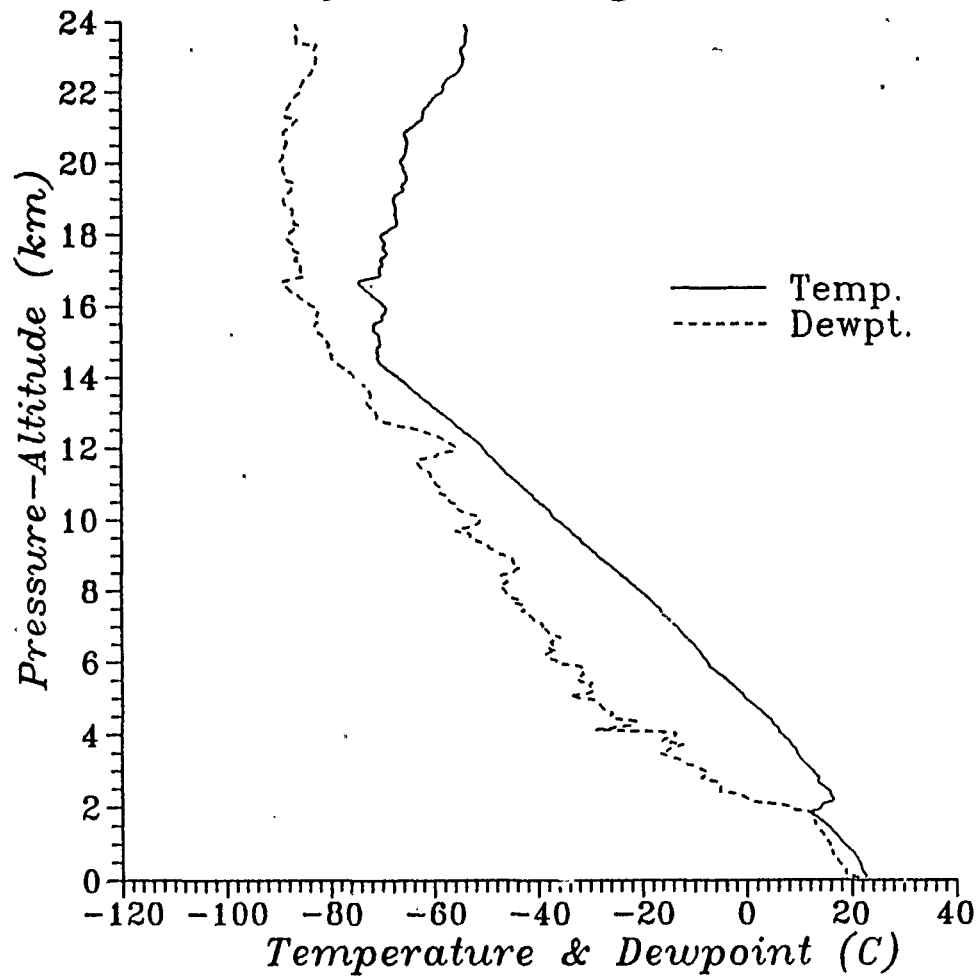


Fig. 89. Kihei, Maui Rawinsonde Data: 0926 UTC 11 July 1988

July 88 - Flight 10

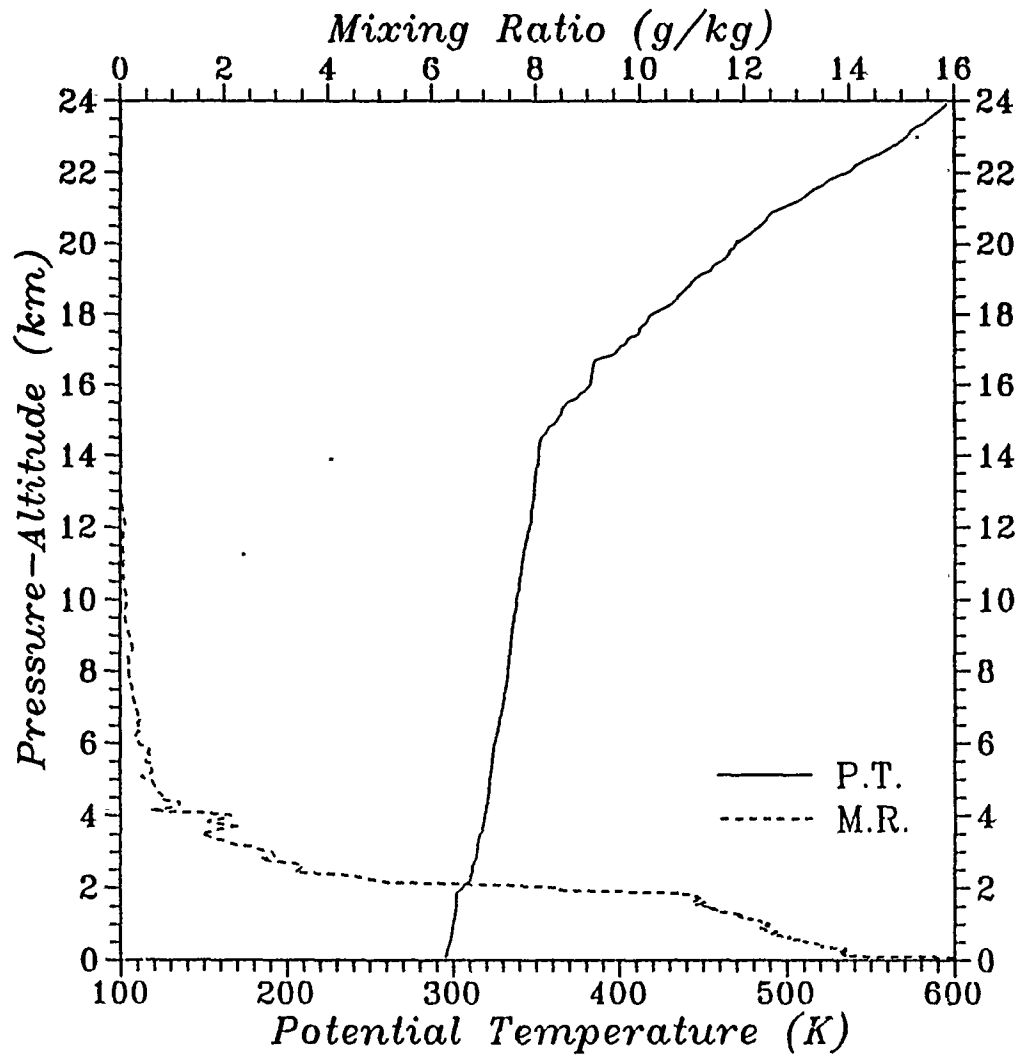


Fig. 90. Kihei, Maui Rawinsonde Data: 0926 UTC 11 July 1988

July 88 - Flight 10

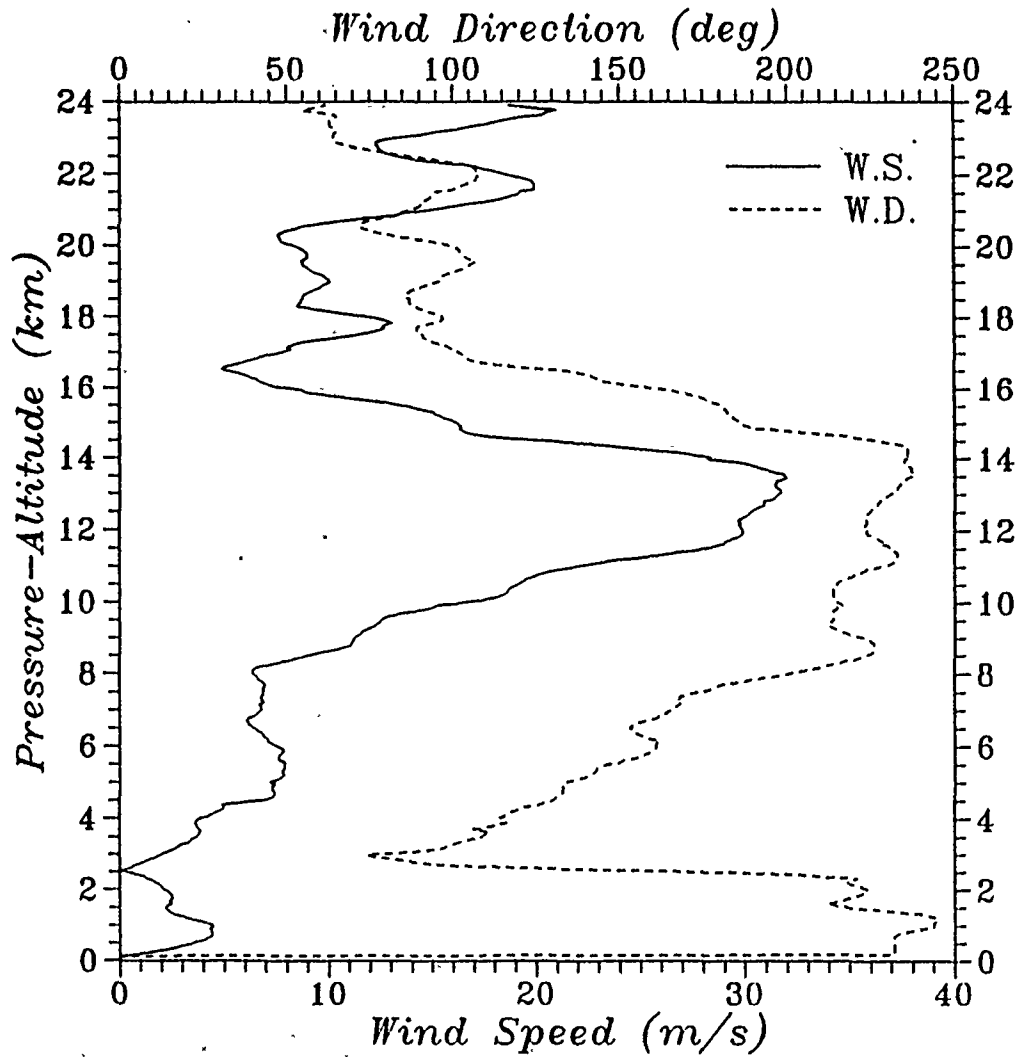


Fig. 91. Kihei, Maui Rawinsonde Data: 0926 UTC 11 July 1988

LIST OF REFERENCES

- Bevington, P.R., 1969: *Data Reduction and Error Analysis for the Physical Sciences*, McGraw-Hill, Inc., New York, 336 pp.
- Blumenstock, D.I. and S. Price, 1967: *Climates of the States-Hawaii*, U.S. Department of Commerce. Climatology of the US No. 60-51, 140 pp.
- Bol'shakova, G.I. and Sh.P. Darchiya, 1966: Fluctuations of Shimmer Angle. *Optical Instability of the Earth's Atmosphere*, Israel Program for Scientific Translations Ltd., Jerusalem, 174 pp.
- Bose, N.K., 1985: *Digital Filters; Theory and Applications*, Elsevier Science Publishing Co., New York, 496 pp.
- Clifford, S.F., 1978: The Classical Theory of Wave Propagation in a Turbulent Medium. *Topics in Applied Physics. Laser Beam Propagation in the Atmosphere*, v. 25, Springer-Verlag, Germany, 325 pp.
- Creal, J.B. et al., 1987: *Hawaii Tourbook*, American Automobile Association, 120 pp.
- Fried, D.L., 1966: Optical Resolution through a Randomly Inhomogeneous Medium for Very Long and Very Short Exposures. *J. Opt. Soc. Am.*, v. 56, 1372-1379.
- Fried, D.L., 1982: Anisoplanatism in Adaptive Optics. *J. Opt. Soc. Am.*, v. 72, 56.
- Gossard, E.E., 1985: Finestructure of Elevated Stable Layers Observed by Sounder and In Situ Tower Sensors. *J. Atmos. Sci.*, v. 42, 2156-2164.
- Hecht, E. and Zajac, A., 1974: *Optics*, Addison-Wesley Publishing Co., Mass., 565 pp.
- Hunten, D.M., 1964: *Introduction to Electronics*, Holt, Rinehart and Winston, New York, 369 pp.
- Huschke, R.E., 1970: *Glossary of Meteorology*, American Meteorological Society, Boston, Mass, 638 pp.
- Kolmogorov, A., 1961: *Turbulence, Classic Papers on Statistical Theory*, ed. by S.K. Friedlander and L. Topper, Interscience, New York, 151.
- Kuchеров, N.I., 1966a: *Optical Instability of the Earth's Atmosphere*, Israel Program for Scientific Translations Ltd., Jerusalem, 174 pp.
- Kuchеров, N.I., 1966b: The effect of Synoptic Fronts on Seeing. *Optical Instability of the Earth's Atmosphere*, Israel Program for Scientific Translations Ltd., Jerusalem, 174 pp.

- Lutomirski, R.F. and H.T. Yura, 1971: Wave Structure Function and Mutual Coherence Function of an Optical Wave in a Turbulent Atmosphere. *J. Opt. Soc. Am.*, v. 61, 482-487.
- Nelson, D.H., 1988: *Atmospheric Turbulence Effects in the Relay Mirror Experiment*, Master's Thesis, Naval Postgraduate School, Monterey, CA, 89 pp.
- Olmstead, M.R., 1988: *Development of a Differential Temperature Probe for the Measurement of Atmospheric Turbulence at All Levels*, Master's Thesis, Naval Postgraduate School, Monterey, CA, 92 pp.
- Stevens, K.B., 1985: *Remote Measurement of the Atmospheric Isoplanatic Angle and Determination of Refractive Turbulence Profiles by Direct Inversion of the Scintillation Amplitude Covariance Function with Tikhonov Regularization*, Ph.D. Dissertation, Naval Postgraduate School, Monterey, CA, 170 pp.
- Tatarski, V.I., 1961: *Wave Propagation in a Turbulent Medium*, Dover Publications, Inc., New York, 285 pp.
- Tatarski, V.I., 1971: *The Effects of the Turbulent Atmosphere on Wave Propagation*, National Technical Information Service, Va, 471 pp.
- Vaisala, 1986a: *DigiCORA*, Wodurn, Mass, Ref. A0416.
- Vaisala, Upper Air Systems Division, 1986b: *RS 80 Radiosondes*, Wodurn, Mass, Ref. A0435.
- Wallace, J.M. and P.V. Hobbs, 1977: *Atmospheric Science An Introductory Survey*, Academic Press, Inc., New York, 467 pp.
- Walters, D.L., 1981: Atmospheric Modulation Transfer Function for Desert and Mountain Locations: r_0 Measurements. *J. Opt. Soc. Am.*, v. 71, 403.
- Walters, D.L., 1985: Saturation and the Zenith Angle Dependence of Atmospheric Isoplanatic Angle Measurements. *Adaptive Optics*, v. 551, 38.
- Walters, D.L., 1989: Private Communication.
- Walters, D.L., Favier, D.L. and Hines, J.R., 1979: Vertical Path Atmospheric MTF Measurements. *J. Opt. Soc. Am.*, v. 69, 829.
- Walters, D.L. and Kunkel, K.E. 1981: Atmospheric Modulation Transfer Function for Desert and Mountain Locations: The Atmospheric Effects on r_0 . *J. Opt. Soc. Am.*, v. 71, 397-398.
- Zinchenko, L.K., 1966: An Estimation of Atmospheric Turbulence Affecting Seeing. *Optical Instability of the Earth's Atmosphere*, Israel Program for Scientific Translations Ltd., Jerusalem, 174 pp.

INITIAL DISTRIBUTION LIST

	No. Copies
1. Defense Technical Information Center Cameron Station Alexandria, VA 22304-6145	2
2. Library, Code 0142 Naval Postgraduate School Monterey, CA 93943-5002	2
3. Professor Donald L. Walters, Code 61We Naval Postgraduate School Monterey, California 93943-5000	10
4. Gail Tirrell Vaucher, Code 61 Department of Physics Naval Postgraduate School Monterey, California 93943-5000	3
5. Air Force Weapons Laboratory (AFWL/ARCS) Attn: Mr. Paul Kervin Kirtland A.F.B., New Mexico 87117-6008	5
6. Chairman (Code 68Mr) Department of Oceanography Naval Postgraduate School Monterey, California 93943-5000	1
7. Chairman (Code 63Rd) Department of Meteorology Naval Postgraduate School Monterey, California 93943-5000	1
7. Chairman (Code 61Wh) Department of Physics Naval Postgraduate School Monterey, California 93943-5000	1
8. Director Naval Oceanography Division Naval Observatory 34th and Massachusetts Avenue NW Washington, DC 20390	1
9. Commander Naval Oceanography Command Stennis Space CTR, MS 39529-5000	1

- | | | |
|-----|---|---|
| 10. | Commanding Officer
Naval Oceanographic Office
Stennis Space CTR, MS 39522-5001 | 1 |
| 11. | Commanding Officer
Fleet Numerical Oceanography Center
Monterey, CA 93943-5005 | 1 |
| 12. | Commanding Officer
Naval Ocean Research and Development Activity
Stennis Space CTR, MS 39529-5004 | 1 |
| 13. | Commanding Officer
Naval Environmental Prediction Research Facility
Monterey, CA 93943-5006 | 1 |
| 14. | Chairman, Oceanography Department
U.S. Naval Academy
Annapolis, MD 21402 | 1 |
| 15. | Chief of Naval Research
800 N. Quincy Street
Arlington, VA 22217 | 1 |
| 16. | Office of Naval Research (Code 420)
Naval Ocean Research and Development Activity
800 N. Quincy Street
Arlington, VA 22217 | 1 |
| 17. | Program Manager (CIRF)
Air Force Institute of Technology
Wright-Patterson Air Force Base, OH 45433 | 1 |
| 18. | Commander
Air Weather Service
Scott Air Force Base, IL 62225 | 1 |
| 19. | Commanding Officer
Air Force Global Weather Central
Offutt Air Force Base, NE 68113 | 1 |
| 20. | Commander (AIR-370)
Naval Air Systems Command
Washington, DC 20360 | 1 |
| 21. | Library Acquisitions
National Center for Atmospheric Research
P.O. Box 3000
Boulder, CO 80307 | 1 |

22. Research Administrative Dept.
Code 012
Naval Postgraduate School
Monterey, California 93943-5000

1